UNIVERSITY OF CALIFORNIA SAN DIEGO

Tuning Nanoparticle Synthesis to Enable Anionic and Cationic Redox in Cathode Materials

A dissertation submitted in partial satisfaction of the
requirements for the degree
Doctor of Philosophy

in

Nanoengineering

by

Hyeseung Chung

Committee in charge:

Professor Ying Shirley Meng, Chair
Professor David P. Fenning
Professor Olivia A. Graeve
Professor Ping Liu
Professor Yu Qiao

2020

The dissertation of Hyeseung Chung is approved, and it is acceptable in quality and form for publication on microfilm and electronically:

_____

_____

_____

_____

_____

Chair

University of California San Diego

2020

TABLE OF CONTENTS

LIST OF FIGURES

LIST OF TABLES

ACKNOWLEDGEMENTS

All the work presented here would not be possible without the support of many. First, I would like to thank my PhD advisor Professor Ying Shirley Meng for her generous guidance, mentorship, and financial support. It was honor to work with her in the last five years. I would like also to express my deep gratitude to my committee members: Professor Ping Liu, Professor Olivia A. Graeve, Professor Yu Qiao, and Professor David P. Fenning.

During my PhD, I received infinite support from my friends and family. I would like to especially thank my parents, In Seop Chung and Myung Sook Lee, who are the greatest mentors in my life. Thank you for always believing in me.

I would like to acknowledge all my brilliant minded collaborators. I am grateful that I was able to work with Dr. Jean-Marie Doux and Dr. Minghao Zhang, whom I could always count on for insightful discussions even in the middle of their busy schedules. I would like to also acknowledge the most hardworking undergraduate students that I ever met – Jessie Lin, Ricky Huang, and Carlos Mejia. They all taught me more than I taught them. I am extremely grateful to all my collaborators in EFRC consortium, but especially, Dr. Antonin Grenier and Dr. Zachary Lebens-Higgins. I learned a lot from their expertise. I would like to acknowledge Dr. Ich Tran and Dr. Toshihiro Aoki from University of California Irvine and Dr. Peter Ercius and Mr. Chengyu Song from Lawrence Berkley National Lab, who were always helpful and proactive when I wanted to discuss about the challenges I faced in my research. I would like to also acknowledge Vadim Malis who helped a lot of graphics presented here. Lastly, I would like to acknowledge all my group mates in Laboratory for Energy Storage and Conversion. Each of them helped and inspired me in many ways.

Chapter 3, in full, is a reprint of material, as it appears in: H. Chung; A. Grenier; R. Huang; X. Wang; Z. Lebens-Higgins; J. Doux; S. Sallis; C. Song; P. Ercius; K.W. Chapman; L.F.J. Piper; H. Cho; M. Zhang; Y.S. Meng, “Comprehensive study of a versatile

polyol synthesis approach for cathode materials for Li-ion batteries," *Nano Research*, 12, 2238-2249 (2019). The author was the primary investigator and author of this paper. All the experiment parts were performed by the author except sXAS, sXRD, and sol-gel LNMO electrochemical testing.

Chapter 4, in full, is currently being prepared for submission for publication as: H. Chung; A. Grenier; C. Mejia; R. Huang; K.W, Chapman; S.J. Kim; Y.S. Meng, "Insights into Twin Boundary Defect and Mitigation of Anisotropy Change in Classical Layered Oxide Material for Li-ion batteries," The author was the primary investigator and author of this paper. All the experiment parts were performed by the author except operando XRD analysis.

Chapter 5, in full, is currently under review as: H. Chung; Z. Lebens-Higgins; B. Sayahpour; C. Meija; A. Grenier; G.E. Kamm; Y. Li; R. Huang; L.F.J. Piper; K.W. Chapman; J. Doux; Y.S. Meng, "Experimental Considerations to Study Li-Excess Disordered Rock Salt Cathode Materials." The author was the primary investigator and author of this paper. All the experiment parts were performed by the author except electrochemical testing, XPS, and EIS.

VITA

2012	B. S. in Chemical Engineering, Cornell University
2017	M. S. in Nanoengineering, University of California San Diego
2020	Ph. D. in Nanoengineering, University of California San Diego

PUBLICATIONS

H. Chung, A. Grenier, R. Huang, X. Wang, Z. Lebens-Higgins, J. Doux, S. Sallis, C. Song, P. Ercius, K.W. Chapman, L.F.J. Piper, H. Cho, M. Zhang, and Y.S. Meng, "Comprehensive study of a versatile polyol synthesis approach for cathode materials for Li-ion batteries," *Nano Research*, 12, 2238-2249 (2019).

H. Chung, Z. Lebens-Higgins, B. Sayahpour, C. Meija, A. Grenier, G.E. Kamm, Y. Li, R. Huang, L.F.J. Piper, K.W. Chapman, J. Doux and Y.S. Meng, "Experimental Considerations to Study Li-Excess Disordered Rock Salt Cathode Materials," (under review).

H. Chung, A. Grenier, C. Mejia, R. Huang, K.W. Chapman, S.J. Kim, and Y.S. Meng "Insights into Twin Boundary Defect and Mitigation of Anisotropy Change in Classical Layered Oxide Material for Li-ion batteries," (in preparation).

Z. Lebens-Higgins, **H. Chung**, M.J. Zuba, J. Rana, Y. Li, N.V. Faenza, N. Pereira, B.D. McCloskey, F. Rodolakis, W. Yang, M.S. Whittingham, G.G. Amatucci, Y.S. Meng, T. Lee and L.F.J. Piper, "How Bulk Sensitive is Hard X-ray Photoelectron Spectroscopy: Accounting for the Cathode-Electrolyte Interface when Addressing Oxygen Redox," *The Journal of Physical Chemistry Letters*, 11, 2106-2112 (2020).

H. Hirsh, M. Olguin, **H. Chung**, Y. Li, S. Bai, D. Feng, D. Wang, M. Zhang and Y.S. Meng, "Meso-Structure Controlled Synthesis of Sodium Iron-Manganese Oxides Cathode for Low-Cost Na-Ion Batteries," *Journal of The Electrochemical Society*, 166, A2528 (2019).

J.K. Seo, J.W. Shin, **H. Chung**, P.Y. Meng, X. Wang, and Y.S. Meng, "Intercalation and Conversion Reactions of Nanosized β-MnO_2 Cathode in the Secondary Zn-MnO_2 Alkaline Battery," *The Journal of Physical Chemistry C*, 122, 11177 (2018).

M. Wang, Y. Shi, D.J. Noelle, A.V. Le, H. Yoon, **H. Chung**, M. Zhang, Y.S. Meng and Y. Qiao, "Internal short circuit mitigation of high-voltage lithium-ion batteries with functional current collectors," *RSC Advances*, 7, 45662 (2017).

C.S. Rustomji, Y. Yang, T.K. Kim, J. Mac, Y.J. Kim, E. Caldwell, **H. Chung**, Y.S. Meng, "Liquefied Gas Electrolytes for Electrochemical Energy Storage Devices," *Science*, 356, 1351 (2017).

H. Ren, Y.H. Lee, E.A. Wu, **H. Chung**, Y.S. Meng, E. Fullerton, M. Nguyen, "Nano-Ceramic Cathodes via Co-sputtering of Gd-Ce Alloy and Lanthanum Strontium Cobaltite for Low-Temperature Thin-Film Solid Oxide Fuel Cells," (under review).

Z. Lebens-Higgins, **H. Chung**, I. Temprano, M. Zuba, J. Rana, C. Mejia, M.A. Jones, C. Grey, Y. Du, W. Yang, Y.S. Meng, and L.F.J. Piper "Electrochemical Utilization of Iron IV in the $Li_{1.3}Fe_{0.4}Nb_{0.3}O_2$ disordered rocksalt cathode," (in preparation).

ABSTRACT OF THE DISSERTATION

Tuning Nanoparticle Synthesis to Enable Anionic and Cationic Redox in Cathode Materials

by

Hyeseung Chung

Doctor of Philosophy in Nanoengineering

University of California San Diego, 2020

Professor Ying Shirley Meng, Chair

With an ever-growing number of applications, from portable electronics to electric vehicles, that rely on Li-ion battery technologies, advancements in this field are now shaping the convenience, efficiency, and sustainability of modern society. Further performance improvements are still highly anticipated, pushing the scientific community to develop a novel strategy to design a battery material with enhanced properties. An in-depth understanding of the synthesis process is critical to achieve this goal, since it can provide insights towards controlling the material's chemical and physical properties, such as crystal structure, morphology, and defects. In this study, a polyol method has been developed as a

versatile technique for the synthesis of high-performance, dispersive cathode nanoparticles. Although the polyol method is a promising synthetic process that offers many advantages such as low cost, ease of use, and proven scalability for industrial applications, the scope of previous studies has been mainly limited to simple metals and metal oxides. As a novel method to synthesize battery materials, a detailed reaction mechanism study was conducted using a combination of in situ and ex situ characterization. Nanoscale dynamics that occur during the synthesis process were reported with a focus on the material's structural and chemical transformation. The detailed knowledge of the reaction mechanism helped provide an insight towards finding the optimum synthesis conditions for a variety of cathode materials - including layered $LiNi_{0.4}Mn_{0.4}Co_{0.2}O_2$, spinel $LiNi_{0.5}Mn_{1.5}O_4$, and olivine $LiCoPO_4$. Using scanning transmission electron microscopy, polyol-synthesized $LiNi_{0.4}Mn_{0.4}Co_{0.2}O_2$ was further revealed to be enriched with highly coherent twin boundary defects. The positive role of twin boundary defects was thus proposed, as mitigated anisotropy and volume expansion were observed in the polyol sample during the charge and discharge process. Lastly, in order to increase the capacity, the scope of the studied material was expanded beyond the conventional transitional metal redox and towards high capacity anionic redox materials, referred to as cation-disordered rock salt cathode materials. The strategies to develop the synthesis method that can control the morphology of this material have been proposed, along with the precautions that need to be taken when studying this type of cathode nanoparticles.

Chapter 1

Motivation and Outline

Li-ion batteries have revolutionized our way of life since their introduction to the commercial market three decades ago. They are the key players for enabling portable electronic devices, such as cell phones, laptops, and power tools, with "wireless" revolution granting us a freedom in mobility that we now take for granted. We simply charge our devices at the time and location of our convenience and still fully utilize them without constantly looking for a place to be provided with energy source. Furthermore, the environmental consequences from mankind's centuries of burning fossil fuels and emitting greenhouse gas are becoming more and more tangible in people's lives. Li-ion batteries can enable electric vehicles (EVs) to replace gasoline powered transportation, or make renewable energy sources, such as solar or wind, more competitive for grid-scale applications by enhancing the quality of the energy harvested, alleviating some of the environmental strain generated by fossil fuels. As a result, the demand for Li-ion batteries has been rising rapidly within industry and government alike, pushing the scientific community to develop higher energy density, longer lasting, cheaper, and safer batteries.

Li-ion batteries have certain fundamental advantages over other chemistries. First, lithium is light and has one of the smallest ionic radii for a single charged ion. This provides

advantages in gravimetric and volumetric capacity and power density over other possible elements. Secondly, lithium has the lowest reduction potential of any element, allowing lithium-based batteries to have the highest cell potential. However, conventional Li-ion batteries, which are mainly based on a lithium intercalation mechanism and transition metal redox chemistry, cannot offer the high charge capacity over thousands of cycles that the current market wishes for. Moreover, with the increase in market demand, the price for the elements used mainly in Li-ion battery cathode materials, such as Li, Co, or Ni, has gone up, pushing the search for alternative materials.

Over the years, diverse electrode materials have been proposed, synthesized, and intensely investigated by both academia and industry to overcome these challenges. While early works focused more on solid state physics, the advent of nanotechnology at the end of the 20th century has enabled more recent studies to focus on the morphological aspects of the materials.[1] Morphological aspects of the battery impact the electrochemical performance not only by influencing the active material properties themselves but also by determining the nature of the interface formed with other battery components, such as the electrolyte. The influence of surface coatings, as well as the size and shape of the material, on the electrochemical performance of Li-ion battery, such as achievable capacity, cyclability, and rate performance, are now widely acknowledged in the field. Naturally, nano-sized battery materials, with their unique property of high surface area to volume ratio, has garnered significant attention in battery material research. Throughout my PhD, my research has been focused on developing a versatile method that can control the battery cathode material properties in the nanoscale. Nano-sized materials are ideal for interface studies, given their higher surface areas enable more interface to be formed. It can also potentially enable some of the kinetically challenged battery materials by reducing Li diffusion distance during the charge-discharge process. Thirdly, it is desirable for applications, such as all-solid-state-batteries, as it can provide more intimate solid-to-solid contact. However, it

is extremely challenging to produce competitive-performance cathode materials with these morphologies because higher surface areas suffer from increased electrolyte side reactions, low tap densities, and complexities in synthesis procedures.

My PhD thesis consists of 6 chapters. **Chapter 1** starts with this motivation and outline. **Chapter 2** provides the general introduction of Li-ion battery with emphasis on the different types of cathode materials studied here. It also includes the characterization methods that was repeatedly used during my study. **Chapter 3** focuses on developing a versatile polyol synthesis method that can produce a variety of cathode nanoparticles with enhanced electrochemical performance. The study is followed by detailed reaction mechanism study to provide insight what is happening during each synthesis step. Then, **Chapter 5** investigates the possible origin of the enhanced electrochemical performance observed for polyol synthesized $LiNi_{0.4}Mn_{0.4}Co_{0.2}O_2$ and suggests how twin boundary defects can help mitigate anisotropy during cycling. **Chapter 4** expands the scope of cathode materials from transition metal redox to high capacity anionic redox chemistry and studies cation-disordered rock salt cathode material. The material is systematically evaluated for their potential as the next generation cathode material. **Chapter 6** summarizes the overall work and presents the direction for the future research.

Chapter 2

Background

2.1 Overview of Li-ion Battery

Lithium-ion battery (LIB) is an advanced battery technology that uses Li-ion as the key component of its electrochemistry. It is mainly constituted of four components – cathode, anode, separator, and electrolyte - as illustrated in Figure 2.1.[2] During the charge, Li-ions are extracted from the cathode host, solvate into and move through the electrolyte, and intercalate into the anode host. At the same time, electrons move from cathode to anode through the outside current collectors forming an electric circuit. Since the chemical potential of Li is much higher in the anode than in the cathode, the electric energy can be stored in the form of chemical energy in the process. This process occurs in reverse during the discharge. Li-ions move from anode to cathode and also drive electrons to move from the anode to cathode, generating an electron current. The cathode and anode regions are separated by the separator, which is a microporous membrane that selectively allows the electrolyte and Li-ion to penetrate but prevents the flow of electrons inside the battery. Both electrolyte and separator can be viewed as the inert components in the battery - all the Faradaic processes for energy storage occur only within the cathode

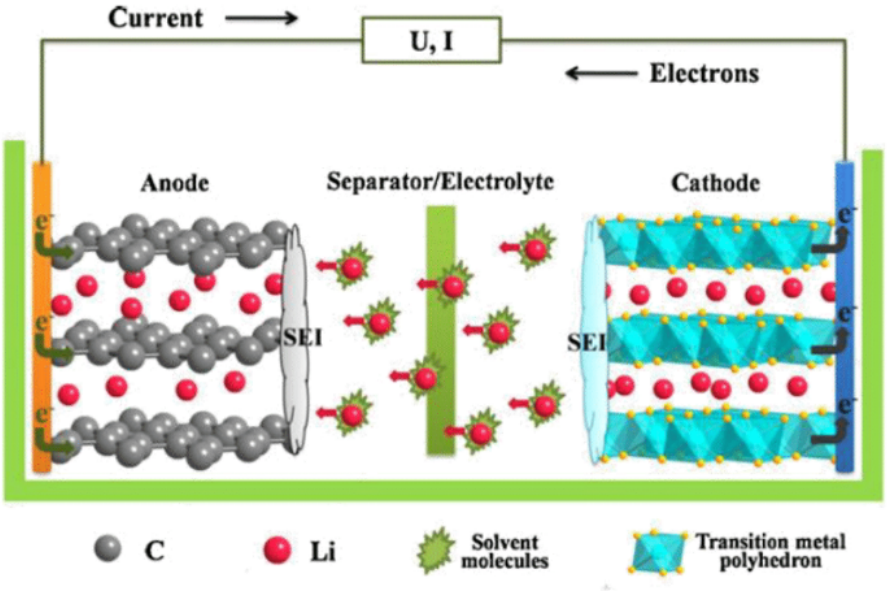

Figure 2.1: Schematic of Li-ion Battery.[2]

and anode electrodes. However, the stability with these inert components and the surface of the electrodes heavily influence the performance of the battery. In addition to being ionically conducting and electrically insulating, an ideal electrolyte should have a wide electrochemical window, so that electrolyte degradation does not occur within the range of the working potentials of both the cathode and the anode.[3] Most of the electrolytes used in commercial LIBs are non-aqueous solutions, where lithium hexafluorophosphate ($LiPF_6$) salt is dissolved in organic carbonates, such as ethylene carbonate (EC) with dimethyl carbonate (DMC), propylene carbonate (PC), diethyl carbonate (DEC), and/or ethyl methyl carbonate (EMC).[4]

Unfortunately, all the components in even the most state-of-the-art batteries go through degradation over time, resulting in performance losses that involve a progressive decrease in capacity and an increase in internal resistance. As illustrated in Figure 2.2, LIB degradation mechanisms are extremely complicated.[5] Previous studies have proposed several mechanisms, supported by a wide range of characterization techniques.[6,7] For

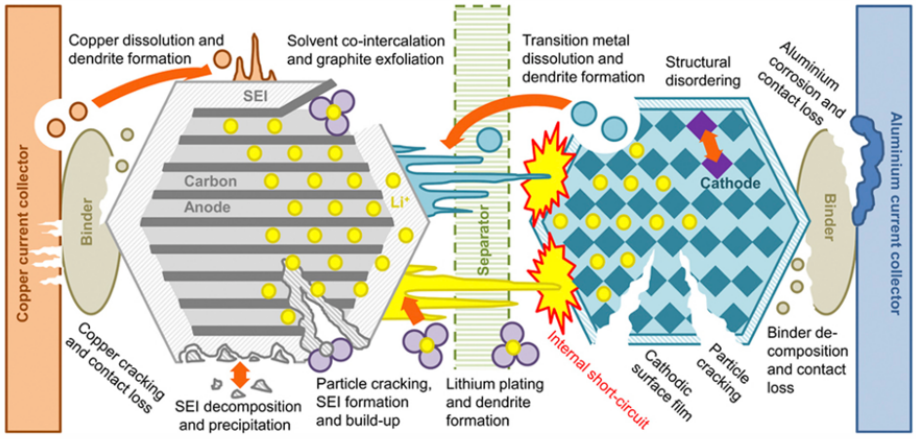

Figure 2.2: Schematics of Proposed Degradation Mechanisms in Li-ion Batteries.[5]

instance, on the cathode side, repeated charge-discharge processes lead to structural disordering, formation of resistant cathode-electrolyte-interphase (CEI), particle cracking, and transitional metal dissolution. The anode side experiences Li-dendrite formation, graphite exfoliation and decomposition, and precipitation of solid-electrolyte-interface (SEI).[5] Despite these studies, we are still far from understanding all the degradation mechanisms of Li-ion batteries and even farther away from coming up with a magic solution that can resolve all these issues. Insights gained from suitable characterization, however, can help us get closer to that goal and help develop a successful design strategy of advanced Li-ion battery materials.

2.2 Cathode Materials in Li-ion Battery

After Whittingham coined the concept of "rocking chair" in the 1970s to describe the intercalation mechanism of Li-ion cells,[8,9] diverse cathode materials have been proposed and investigated. Despite the advancements made, cathodes are still primary bottlenecks of energy density enhancement and cost reduction,[10] thus, my PhD study has been focused on trying to resolve some of these issues. The following cathode materials are some of the

most promising candidates studied, categorized by their crystal structures.

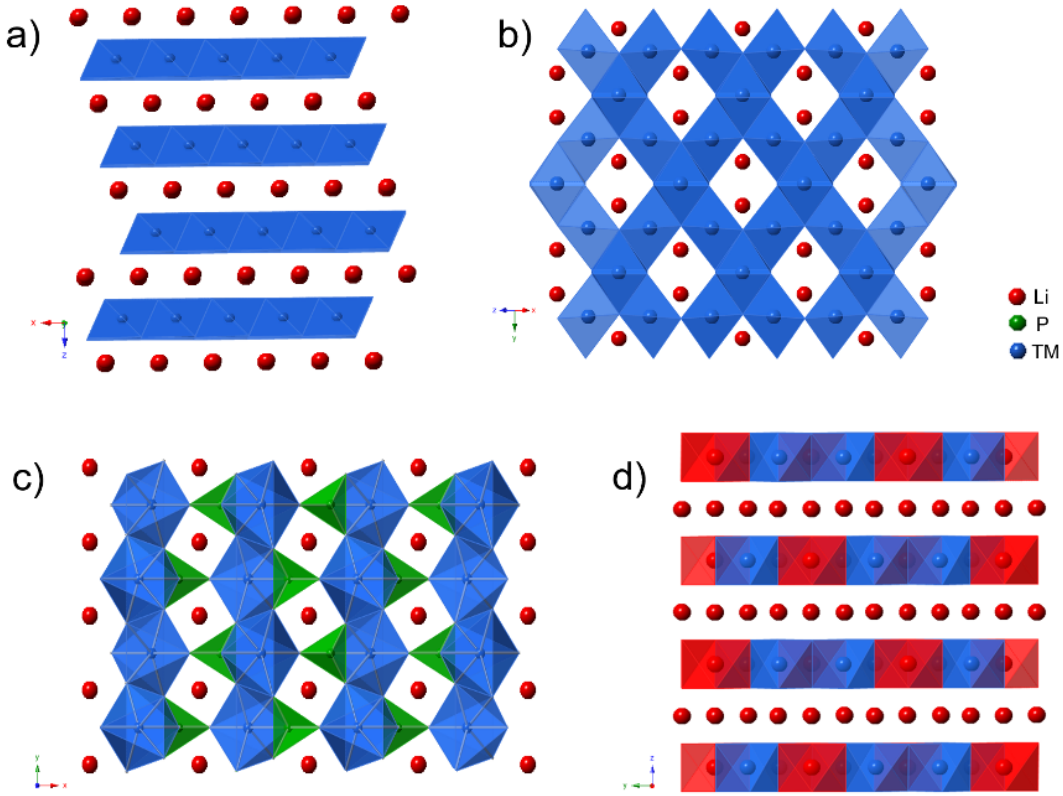

Figure 2.3: Crystal structures of a) layered oxide, b) spinel oxide, c) olivine phosphate, and d) Li_2TMO_3 (Li-rich layered oxide). Blue represents transition metal ions, red represents lithium ions, and green represents phosphorus ions. Oxygen anions were omitted in the illustration for simplicity.

2.2.1 Layered oxides

With the general formula $LiTMO_2$, the crystal structure of layered oxides consists of a close packed oxygen framework with Li-ion and transition metal (TM) cations filling the alternating layers of the interstitial sites.[2,7] As shown in Figure 2.3a, the TM layer consists of edge-sharing TMO_6 octahedra, providing two dimensional pathways for Li-ion to intercalate during the charge and discharge processes.

Since 1990s, layered oxide cathode materials have been widely adopted in the

portable device applications, such as cell phones and laptops.[11] Without a doubt, $LiCoO_2$ (LCO) is the first cathode material to achieve commercial success with its key advantages as follows. First of all, LCO intrinsically forms a good cation ordering, because Li^+ and Co^{3+} have a large enough charge and size difference. This allows the formation of direct Co-Co interaction across the shared octahedral edges in the *TM* plane, which also results in a good electronic conductivity. Good structural stability, along with high electronic and Li-ion conductivity, supports high rate performance without suffering much irreversibility.[10] However, in conjunction with the growing market demand for LIBs, the concerns for Co is growing at the same time due to its toxicity and high cost. This has motivated the scientific community to look for an alternate chemistry. Among them, $LiNi_xMn_yCo_{1-x-y}O_2$ (NMC) has received great attention because it offers a unique blend of advantages – 1) lower cost with less Co dependence, 2) enhanced safety and cycle life with Mn, and 3) high energy capacity with Ni redox (Ni^{2+}/Ni^{4+}). However, as with all layered oxides, the gap between the theoretical and practical capacity exists, because only half of theoretical capacity ($\sim 280\,\mathrm{mA\,g^{-1}}$) are used in practice to compromise the reversibility of the charge-discharge process.

Increasing the operating voltages by further delithiation may achieve initial high capacity but is accompanied material degradation, including microcrack formation and structural transformations at the surface.[12] To solve the long-term stability issues and bridge the gap between theoretical and practical capacity, the degradation mechanism of layered oxides in high voltage operation are addressed more in detail in the following chapters.

2.2.2 Spinel oxides

With the general formula Li_2TMO_4, the crystal structure of spinel oxides is shown in Figure 2.3b. Similar to the layered materials discussed earlier, *TM* cations in spinel

occupy an octahedral site, but 1/4 of them are located in the Li layer. This leaves 1/4 of the *TM* layer vacant. As a result, Li-ions, occupying the tetrahedral sites of the Li layer, share faces with this empty octahedral site, resulting in a three-dimensional diffusion pathway during charge-discharge.[2,13] Due to the difficulty of stabilizing highly oxidized $TM^{3+/4+}$ oxidation state during the synthesis, transition metal that can form spinel oxide materials are usually limited to only a few elements, such as Ti, V, and Mn. Among others, a derivative of $LiMn_2O_4$, $LiMn_{1.5}O_0.5O_4$, has gained much enthusiasm in the field because it shows superior capacity and operating voltage than its parent structure. By substituting 25% Ni for Mn, this composition avoids the Jahn-Teller distortion associated with Mn^{3+} and keep its valence to 4+. Also, the redox potential of $Ni^{2+/3+}$ and $Ni^{3+/4+}$ couples ensure that this material undergoes the majority of its electrochemical reactions at high voltage ($\sim 4.7\,V$ vs. Li). Along with these advantages, high power capability and good rate capability are attractive features of this material, but it should be acknowledged that phase pure LMNO, without impurities, such as NiO and/or $Li_yNi_{1-y}O$, is still difficult to synthesize due to oxygen loss at high temperature.[14] Poor cycle life, especially at elevated temperatures ($\sim 50\,°C$), can come from the disproportion reaction of Mn and is another important challenge to overcome before it can be more widely adopted in the market. Finally, high voltage characteristic is desirable for high energy and power capability, but it accompanies undesirable side reactions between the electrolyte and the cathode material. Electrolyte compatible with LNMO should be developed, as cathode operating voltage is beyond the stability window of typical commercial electrolyte ($\sim 4.5\,V$).[13]

2.2.3 Olivine polyanion oxides

Among several olivine polyanion oxides developed, phosphate-based, $Li\,TMPO_4$, is the most studied and widely used, so it was used as an example for the structure illustrated in Figure 2.3c. As shown, this structure consists of a distorted hexagonal close

packed oxygen array with TM located in half of the octahedral sites and P located in one-eighth of the tetrahedral sites. Corner-shared TMO_6 octahedra and edge-shared LiO_6 octahedra run parallel to the b-axis and are stitched together by the PO_4 tetrahedra. Combination of experimental and computational studies show that Li diffusion occurs only on one dimension (along the b axis) in the olivine framework because it is most energetically favorable. Because oxygen atoms are strongly bonded by both *TM* and P atoms, the material has been considered more stable at high temperature than layered LCO. Unfortunately, strong covalent oxygen bonds also lead to low ionic and electronic conductivity.

Among others, $LiFePO_4$ has already been adopted widely in power tool and electric vehicle applications with good power capability and low manufacturing cost. Low energy density and low operating voltage, however, have shifted interest towards other isostructural materials as well, such as $LiMnPO_4$ (LMP), $LiCoPO_4$ (LCP), and $LiNiPO_4$ (LNP). These compounds provide significant advantages over LFP in gravimetric energy densities, mainly stemming from high operating voltages. To illustrate, the operating voltages for LCP, LMP, and LNP are 4.1, 4.7, and 5.1 V, respectively, much higher than LFP with 3.34 V vs Li/Li^+.[15,16] As a result, some of these materials will be explored in the following chapter.

2.2.4 Anionic redox materials

Compared to previously mentioned cathodes, anionic redox cathode materials set themselves apart in a way that it relies not only on traditional *TM* redox chemistry but also on anion, such as oxygen, redox to achieve high capacity. Moreover, some of the most representative anionic redox materials, such as Li-rich layered oxide or cation-disordered rock salt, use more environmentally benign elements, such as Mn and Fe, with less dependence on Co. As a result, these materials have been receiving great attention in the scientific community as the next generation cathode material.

Li-excess Layered Material

Lithium-excess layered oxides (LLO) is a type of layered oxide, but it goes beyond 1 Li with the traditional TMO_2 formula. It creates a compound somewhere between a rhombohedral $LiTMO_2$ and monoclinic Li_2MnO_3 as shown in Figure 2.3a, d. Therefore, the general formula for LLO is expressed as $Li_{1+x}TM_{1-x}O_2$ or $xLi_2MnO_3-(1-x)LiTMO_2$.[17] Interestingly, when excess Li is incorporated into the TM layer, oxygen becomes less covalent in character and more easily oxidized by donating electrons.[18,19] As a result, additional capacity coming from anionic redox becomes accessible in addition to the capacity coming from conventional transition metal redox. Some of the highest-capacity materials provide capacities of ~ 280 to $310\,mA\,h\,g^{-1}$ with a high working potential of $\sim 3.7\,V$ (vs Li/Li^+), well beyond the capacity that conventional traditional metal oxides can provide. However, extra capacity obtained due to oxygen redox also essentially destabilizes oxygen within the structure and causes irreversible oxygen loss, limiting the reversibility of the material. Doping, surface treatment, or defect engineering are some of the strategies to mitigate the performance degradation that occurs with cycles.[20–22]

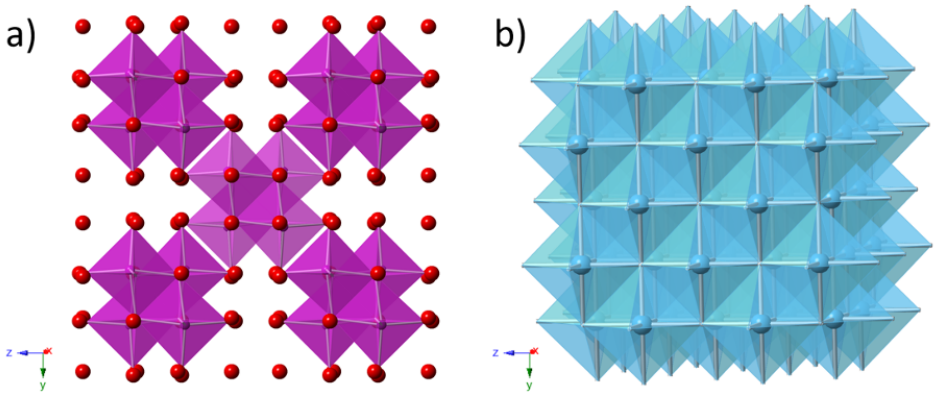

Figure 2.4: Crystal structures of a) Ordered and b) Disordered phase of Li_3NbO_4.

Li-excess Cation Disordered Material

If the *TM* layer is even more enriched with Li than Li-excess layered material, it can no longer maintain an ordered phase, forming the material we refer to as "cation disordered rock salt" phase. For decades of battery material research, cation disorder, where the Li and *TM* mix on each other's position, has been considered detrimental to Li-ion transport, limiting the reversible capacity. However, the discovery of the lithium excess disordered rock salt structure as a high capacity cathode material changed many people's perspectives and created a new paradigm in battery material design. This material, which does not even have a distinct Li-pathway, promises high capacity with a number of studies reporting $\sim 300\,\mathrm{mA\,h\,g^{-1}}$ at elevated temperature (60 °C).[23]

Li_3NbO_4 is one of the most commonly used host structures for the cation disordered rock salt structure. As illustrated in Figure 2.4, Li_3NbO_4 can exist in two types: "disordered" and "ordered". In the illustration, oxygen anions are omitted for simplicity, Ordered phase consists of four edge-shared NbO_6 octahedra (represented in purple) with Li-ion (represented in red) accommodated in a body-centered cubic lattice. In disordered phase, Nb and Li are randomly distributed within the structure. Disordered Li_3NbO_4 is both synthetically challenging and electrochemically inactive due to its insulating character without electrons in a conduction band (Nb^{5+} has $4d^0$ configuration). However, when Li/Nb are substituted to *TM* with similar ionic radii, such as Fe^{3+}, V^{3+} and Mn^{3+}, the ordering of Nb in the cubic close packed oxygen array is disrupted, favoring the formation of cation-disordering. Therefore, depending on the degree of substitution, the general formula is also written as $x\mathrm{Li_3NbO_4} - (1-x)\mathrm{Li}\,TM\mathrm{O_2}$. Unfortunately, the material also suffers from poor cyclability and rate performance.[24] Efforts to overcome such issues will be addressed in Chapter 5.

2.3 Material Characterization Method

2.3.1 X-ray Diffraction and Pair Distribution Function

The crystal structures of the battery materials are closely related to the performance of the battery, such as power and energy density, cyclability, and rate capability. Thus, as a powerful non-destructive technique to characterize crystalline material, X-ray diffraction (XRD) and pair distribution function (PDF) are indispensable techniques for battery material identification and characterization, including all the studies presented here.

In XRD, a beam of X-rays illuminates a sample, which leads to the energy being absorbed by electrons and then released in the form of secondary emissions, a mechanism also known as elastic scattering. For crystalline materials with long range periodicity in the atomic arrangement, scattering occurs as regular arrays of waves. Diffraction can be observed when the scattered radiation waves undergo constructive interference in accordance with Bragg's law:

$$n\lambda = 2d\sin\theta \tag{2.1}$$

where n is the number of wavelengths in the path difference between diffracted X-rays and adjacent crystal planes, λ represents the wavelength of the incident X-ray, d represents interplanar spacing, and θ is the scattering angle between the incident X-ray and the lattice planes. The schematic is presented as in Figure 2.5.[25]

The target material used to generate incident X-rays determine the specific wavelength, λ, during the measurement. In laboratory XRD, Cu and Mo are the most frequently used targets, each with the wavelength of Cu K_α ($\lambda \approx 1.54\,\text{Å}$) or Mo K_α ($\lambda \approx 0.71\,\text{Å}$) (Figure 2.6). Cu offers advantages such as high intensity, good resolution, and high thermal conductivity (easier to design cooling system). X-ray produced by Mo, with a shorter wavelength than copper, will scatter more weakly and contract the diffraction towards low

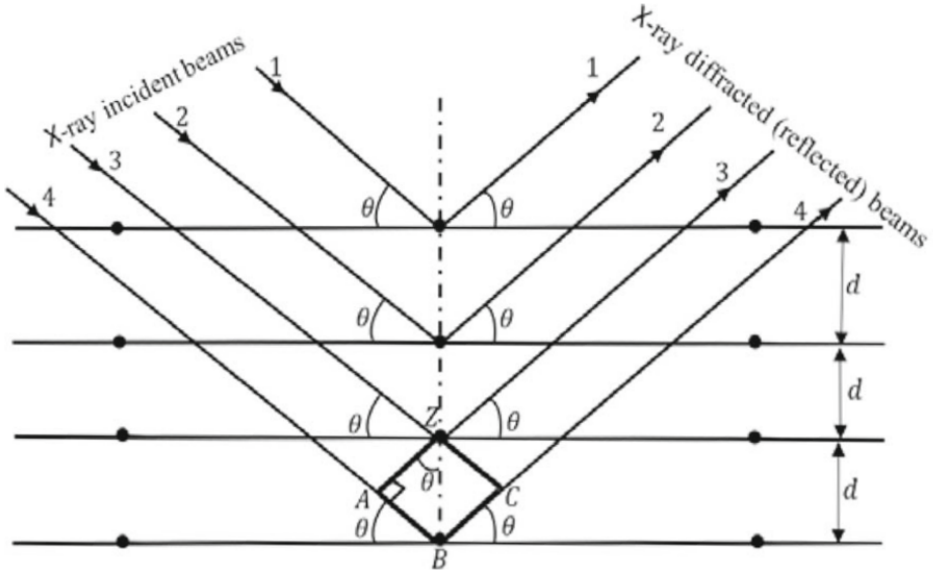

Figure 2.5: Schematic of X-ray diffraction pattern.[25]

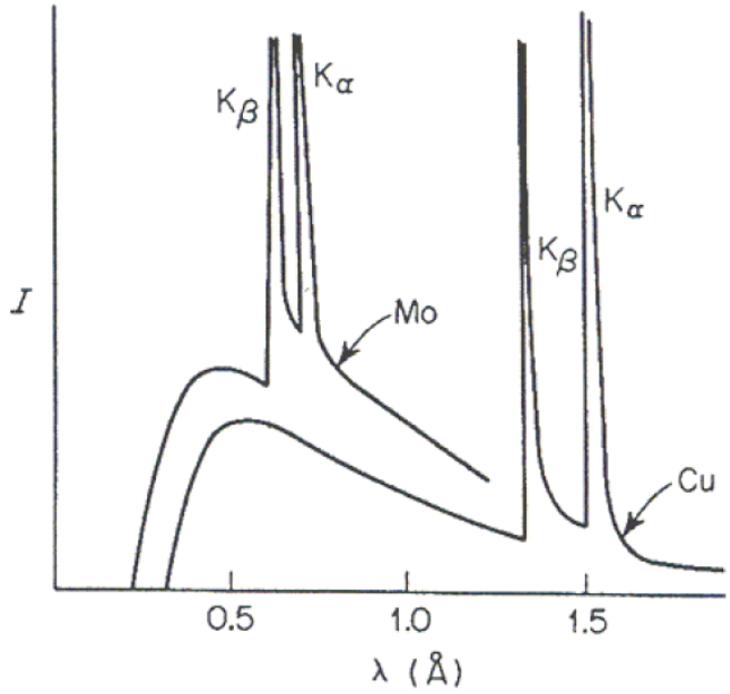

Figure 2.6: Continuous X-ray spectra with characteristic peaks from Mo and Cu anodes.[26]

Bragg angles, resulting in loss of d spacing and accuracy resolution. However, Mo-source has an advantage over Cu-source in many battery materials due to the background contribution coming from fluorescence. When the incident X-ray excites electrons in the sample, it also emits the characteristic X-ray radiation of the respective elements in the sample, known as fluorescence. Unfortunately, common elements used for battery materials, such as Fe, Co, or Mn, have a radiation close to that of Cu, resulting in high background in the XRD pattern. Although Mo-radiation does not prevent these elements from inducing fluorescence, the energy difference between their radiation and Mo K_α radiation is large enough that the two can be distinguished by properly set detector. Thus, Mo is eliminating the detected fluorescence signal, while in the case of Cu, the energy difference is too small to be separated by most detectors.

In order to overcome the shortcomings of the lab-based XRD, synchrotron XRD (sXRD) are often used to complement the study. Although it may not be as accessible to users as lab-based XRD, sXRD offers advantages, most notably its brilliance, which is described by both the brightness and the angular speed of the beam. A typical synchrotron source X-ray has more than a billion times higher brilliance than a lab source. High intensity of the beam allows us to have good quality data even with small samples and fast data acquisition times. While wavelength is tunable, typically small wavelengths are used in the measurement, which permits the study of tiny features with high accuracy, such as nanoscale materials and bond structures in the molecule.

Furthermore, since synchrotron X-rays have both high energy and high flux of X-ray photons, it is often coupled with pair distribution function (PDF) measurement. PDF analysis provides rich information that concerns the distribution of distances between pairs of particles contained within a given volume of the sample. Thus, while the diffraction-based technique is established based on translational symmetry, which relies on long-range order, PDF can provide more insights into the local structure of materials where the structural

coherence extends only over a few nanometers. Nano- or amorphous materials used in my study also benefitted from PDF analysis. The pair distribution function $g(r)$ is defined as:

$$g(r) = \frac{1}{4\pi\rho_0 r^2 N} \sum_i \sum_{j \neq i} \delta\left(r - r_{ij}\right) \tag{2.2}$$

in which r is the average number density of atoms, N is the number of atoms, and r_{ij} is the distance between atom i and atom j. $\delta(r - r_{ij})$ is the Dirac delta function which equals a single unit only when $r = r_{ij}$. In practice, PDF patterns in most studies are usually presented in the reduced atomic pair distribution function $G(r)$, defined as:

$$G(r) = 4\pi r \rho_0 [g(r) - 1] \tag{2.3}$$

This is because $G(r)$ can be directly calculated from the measured total scattering function through Fourier transformation with measured coherent scattering intensity.[27] Figure 2.7 presents the typical PDF pattern with the illustration of structural information it can provide.

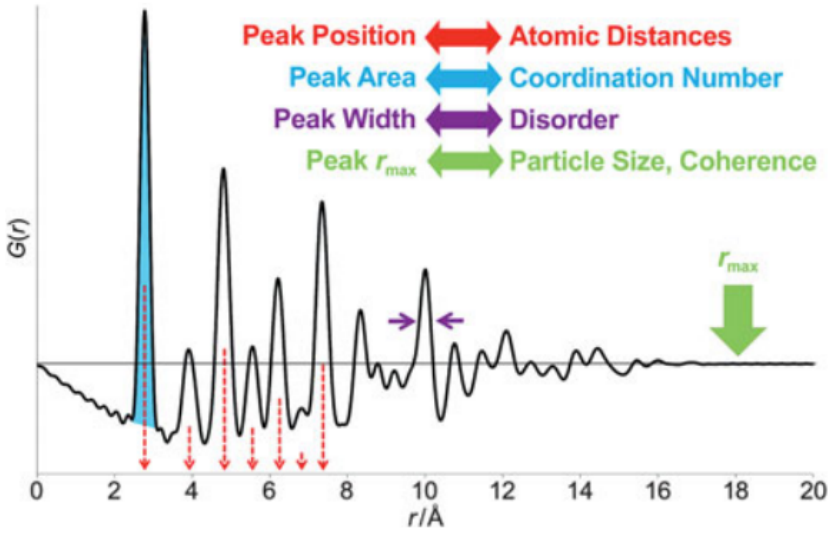

Figure 2.7: Schematics of PDF analysis.[28]

2.3.2 X-ray Photoelectron Spectroscopy

X-ray photoelectron spectroscopy (XPS), also known as electron spectroscopy for chemical analysis (ESCA), is a surface-sensitive characterization technique that is widely used in material science research. It provides the chemical information, such as elemental composition, empirical formula, and the chemical and electronic state of each element within the sample. In my study, XPS was extensively used to characterize the surface layer on cathode material developed due to contact with electrolyte or ambient-air storage. Typically, this type of surface layer is extremely thin ($< 5\,\mathrm{nm}$) and may be below the detection limit of other characterization techniques that gives the average information about the bulk material.

As shown in Figure 2.8, XPS instruments usually consist of a monoenergetic X-ray source, sample stage, electron energy analyzer, and electron detector system, which are all encapsulated in an ultra-high vacuum chamber ($\sim 10^{-10}\,\mathrm{mbar}$) with magnetic shielding. In this set up, a beam of X-ray irradiates a solid surface of a sample, which emits a photoelectron with the absorbed energy. The ejected electrons are filtered in hemispherical energy analyzers which will disperse these electrons based on their kinetic energy before the intensity is recorded in the detector. Due to the conservation of energy, the kinetic energy of the ejected electron (KE) can be correlated to the binding energy of the electron relative to the chemical potential (BE) as:

$$KE = hv - BE - \Phi_{\mathrm{spectrometer}} \tag{2.4}$$

where hv represents the energy of the X-ray photons being used and $\Phi_{\mathrm{spectrometer}}$ represents the work function of the spectrometer. Typical XPS spectra plot the number of electrons detected with respect to binding energy, because the kinetic energy is dependent on the source of X-ray photon energy used in the measurement. While there are several X-ray

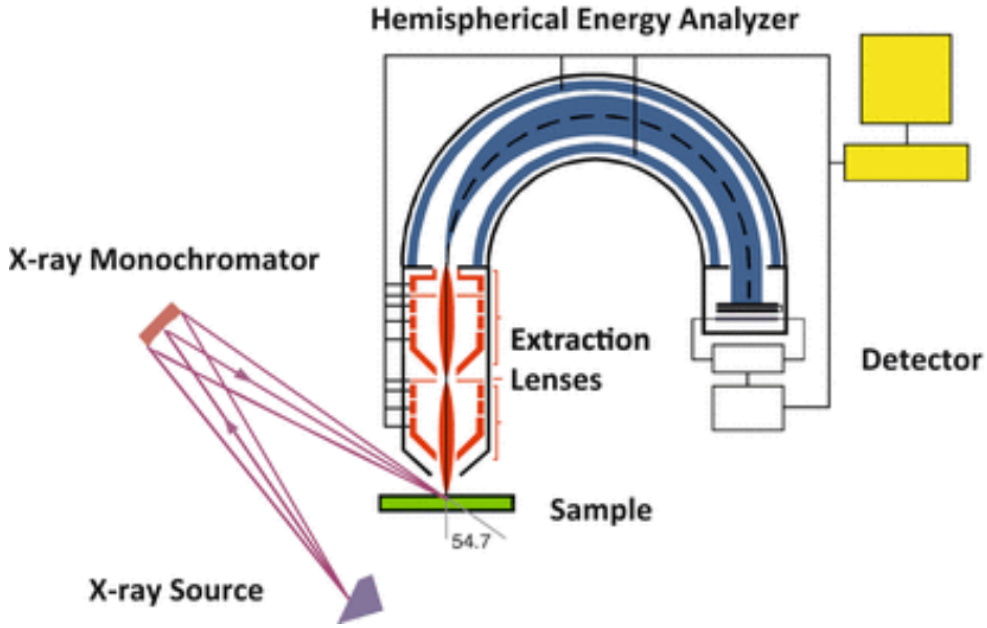

Figure 2.8: Schematic of a typical X-ray photoelectron spectrometer.[29]

sources that can be used in XPS, Al K_α X-rays are one of the most commonly used. It is centered on 1486.7 eV and has its intrinsic full width at half maximum (FWHM) of 0.43 eV. With monochromators, the energy width can be decrease down to 0.16 eV, with practical resolution achieving around ~ 0.3 eV in typical XPS instrument.

As mentioned earlier, XPS is only surface-sensitive, because electrons with kinetic energy typically studied by XPS are in the range of $0 - 1400$ eV and can only travel finite distances through a condensed phase before they scatter inelastically. Such attenuation of signal is governed by the Beer-Lambert Law:

$$I = I_0 \exp\left(-d/\lambda \cos\theta\right) \tag{2.5}$$

where I is the attenuated electron signal, I_0 is the non-attenuated surface electron signal, d is the depth of electron it is generated from, λ is the inelastic mean-free path, and θ is the angle that electrons are emitted with respect to the surface normal. Under this principle, 95% of the signal intensity ($I/I_0 = 0.05$) comes from the depth of $d = 3\lambda\cos\theta$.

Even assuming the maximum for $\cos\theta$ with $\theta = 0°$, most of the detected signal still comes from 3λ. Since the photoelectrons of interest in XPS have relatively low kinetic energy, XPS gives the sample information no more than $\sim 5\,\text{nm}$ below the surface.

2.3.3 Transmission Electron Microscopy and Electron Energy Loss Spectroscopy

Transmission Electron Microscopy (TEM) is a powerful characterization tool that utilizes high energy electrons to extract morphological, compositional, and crystallographic information of a sample. Unlike optical microscopes, in which the resolution is limited to $\sim 200nm$ by the Raleigh criterion, electron microscopes use electrons with much shorter wavelengths than photons. Based on the de Broglie relationship that calculates the wavelength based on the momentum ($\lambda = h/p$), the wavelength achievable for electron microscopes follows the equation:

$$\lambda = \frac{h}{\sqrt{2meV}} \tag{2.6}$$

where h is Planck's constant, m is the mass of a particle, v is the velocity, e is the charge of an electron, V is the accelerating voltage. Once all the constants are replaced, the wavelength limitation for electron microscope becomes $12.25 \cdot 10^{-10}/\sqrt{V}$. Thus, TEM operating at 200 and 300 keV have the wavelengths of about 2.74 pm and 2.24 pm, respectively. With this key capability of high-resolution imaging, TEM was extensively used in my study to observe nanoscale dynamics that occur during the material charge-discharge or synthesis process.

A schematic of a typical TEM is illustrated in Figure 2.9. First, the illumination system generates an electron beam with an electron gun accelerated by a high voltage electric field. The beam is then gathered by condenser lenses and focused onto the sample area of interest. Depending on the TEM mode of the user's choice, parallel or

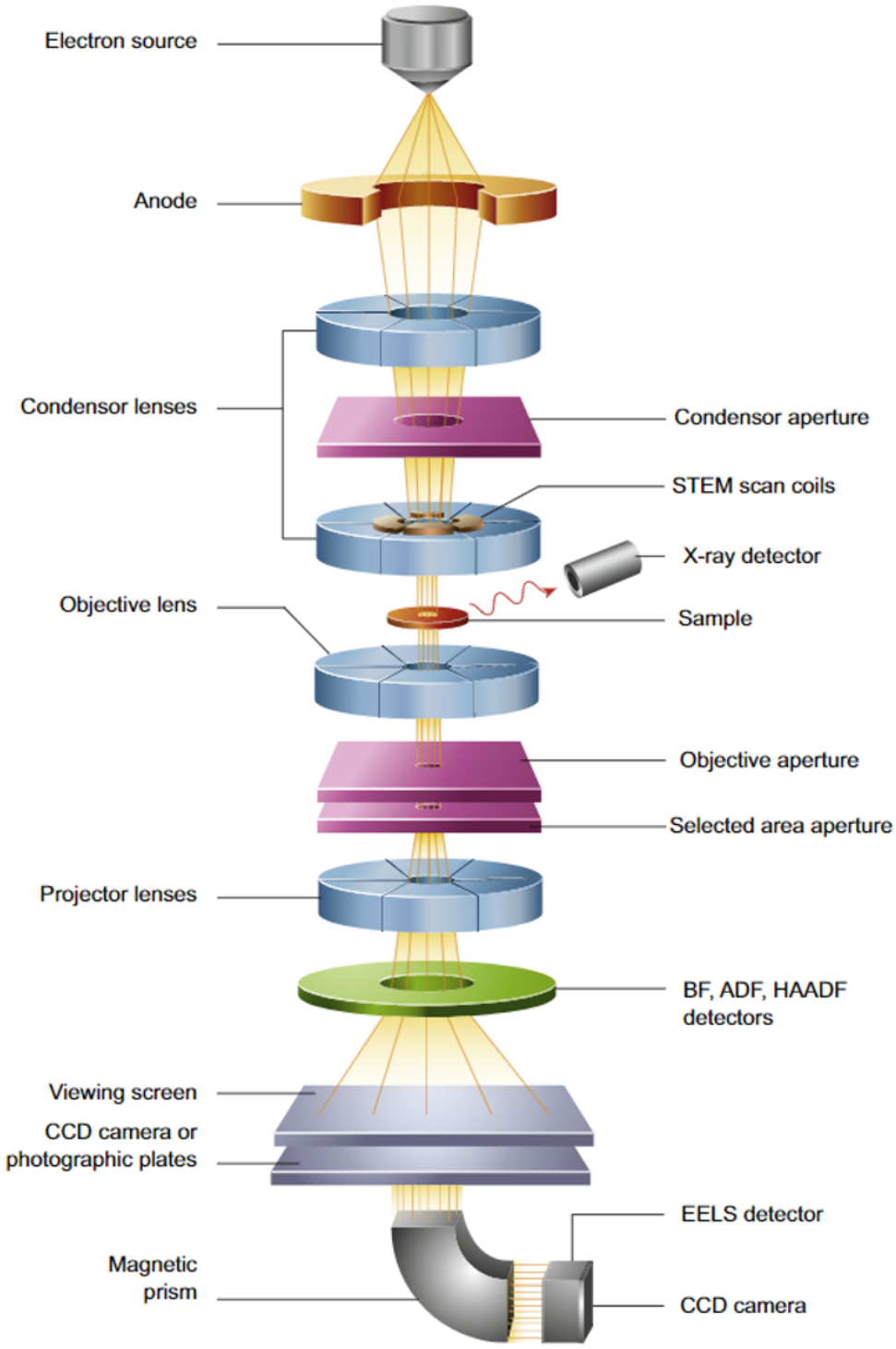

Figure 2.9: Schematics of TEM column.[30]

convergent beam can interact with the sample. Parallel beams are generated in the case of conventional transmission electron microscopy, denoted as (C)TEM, while convergent beams are generated in scanning transmission electron microscopy (STEM). Two modes are usually used interchangeably in material science depending on the sample properties and type of sample information trying to be acquired. Afterwards, the beam will go through an objective lens, which is the key determinant for the microscope resolution. Finally, there is an imaging system which magnifies the image and converts the electron image into a digital image that we observe from the screen. TEM can be equipped with an x-ray detector for energy dispersive spectrometer (EDS), which is usually located near the objective pole-piece, and an electron energy loss spectrometer (EELS), typically located at the bottom of the microscope.[28]

As mentioned earlier, the imaging can be done in both TEM and STEM mode. High-resolution TEM generates phase contrast images, which is based on the difference in the phase of the electron waves scattered through a thin specimen. On the other hand, STEM generates Z-contrast images based on the elastic scattering of electrons. STEM image can be directly interpreted as it gives the information based on the atomic number. Using high angle annular dark-filed (HAADF) detectors, well set up and aligned STEM can offer atomic resolution images, as shown in my study. Furthermore, STEM is often used in conjunction with EELS. EELS is based on the inelastic scattering (electron lose energy) that occurs when the electron beam goes through the sample. The number of electrons at each energy loss provide valuable information about the sample, such as chemical bonding and valence states.

Chapter 3

Comprehensive study of a versatile polyol synthesis approach for cathode materials for Li-ion batteries

This work reports a comprehensive study of a novel polyol method that can successfully synthesize layered $LiNi_{0.4}Mn_{0.4}Co_{0.2}O_2$, spinel $LiNi_{0.5}Mn_{1.5}O_4$, and olivine $LiCoPO_4$ cathode materials. When properly designed, polyol method offers many advantages such as low cost, ease of use, and proven scalability for industrial applications. Most importantly, the unique properties of polyol solvent allow for greater morphology control as shown by all the resulting materials exhibiting monodispersed nanoparticles morphology. This morphology contributes to improved lithium ion transport due to short diffusion lengths. Polyol-synthesized $LiNi_{0.4}Mn_{0.4}Co_{0.2}O_2$ delivers a reversible capacity of 101 and $82\,mA\,h\,g^{-1}$ using high current rate of 5C and 10C, respectively. It also displays surprisingly high surface structure stability after charge-discharge processes. Each step of the reaction was investigated to understand the underlying polyol synthesis mechanism. A combination of *in situ* and *ex situ* studies reveal the structural and chemical transformation of Ni-Co

alloy nanocrystals overwrapped by a Mn- and Li-embedded organic matrix to a series of intermediate phases, and then eventually to the desired layered oxide phase with a homogeneous distribution of Ni, Co, and Mn. We envisage that this type of analysis will promote the development of optimized synthesis protocols by establishing links between experimental factors and important structural and chemical properties of the desired product. The insights can open a new direction of research to synthesize high-performance intercalation compounds by allowing unprecedented control of intermediate phases using experimental parameters.

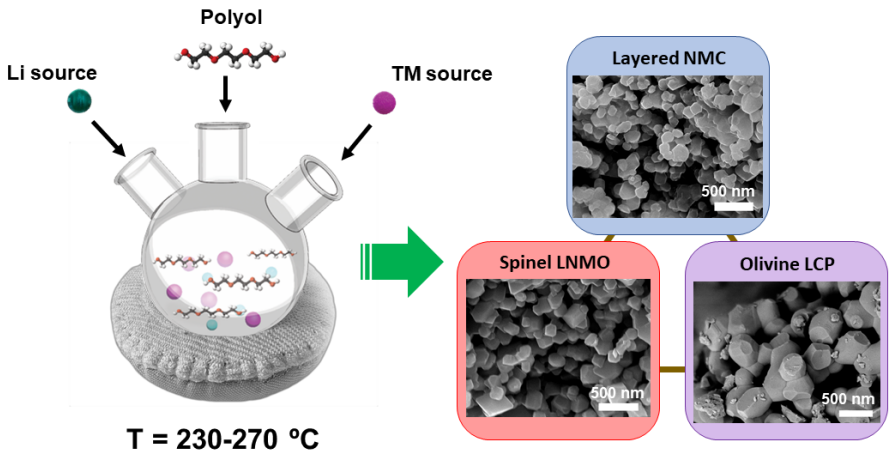

Figure 3.1: Polyol Synthesis for Three Types of Cathode Materials

3.1 Introduction

One of the most pressing challenges that modern society faces is to provide energy sources for a variety of applications, ranging from small portable devices to electric vehicles (EVs) and large grid-scale systems to store energy from intermittent solar or wind-driven devices.[31] Recently, enough technological advancement has been made that

Li-ion batteries (LIBs) are now considered the most promising solution for this problem. There is, however, no single universal battery material that can meet the demands of all these applications. Just as there are various devices that can benefit from Li-ion battery technology, each respective application has a different set of prioritized features for energy storage, such as high power for power tools, high energy for portable devices, or competitive cost for grid-scale energy storage.[32–34] Particularly, cathode materials have received considerable attention because they are considered as the primary determinant for meeting these demands. As a result, diverse cathode materials have been proposed and intensely investigated by both academia and industry.[35] Categorized by their unique crystal structures, the current state-of-the-art cathode materials include layered oxide compounds ($LiCoO_2$, $LiNi_xMn_yCo_{1-x-y}O_2$, $LiNi_{0.85}Co_{0.10}Al_{0.05}O_2$), spinel compounds ($LiMn_2O_4$, $LiNi_{0.5}Mn_{1.5}O_4$), and olivine compounds ($LiFePO_4$, $LiCoPO_4$).

The evaluation of these cathode materials cannot be conducted without the exploration of diverse synthetic methods. To date, the synthesis process to make the cathode oxide material has been developed with the goal of producing a product of a specific phase, with a desired particle size and shape, and without local compositional and crystallographic inhomogeneities.[36] Many developed methods proved to have advantages but were simultaneously accompanied by some major drawbacks. In the traditional solid-state method, the mixing of multiple metal sources is done by manual grinding or ball milling. This method is simple and easy in preparation but results in a microcrystalline product with long lithium ion diffusion pathways as well as inhomogeneous morphology and metal distribution. Such features have an adverse effect on the electrochemical reaction kinetics. The co-precipitation method compensates for some of these shortcomings, but it also requires a careful control of pH when using carbonate[37,38] or an inert atmosphere to minimize the undesired impurities when using hydroxide.[39] Previous studies show that the hydrothermal method is an effective way to synthesize cathode materials with high crystallinity, but its complex set up and high

cost makes it impractical to be applied in large-scale synthesis.[40,41] The sol-gel method also poses challenges due to the high pH sensitivity of the gel formation. An inappropriate control of the pH may result in the formation of a precipitate instead of a gel, producing undesirable inhomogeneity of the product.[42] Lastly, most of the conventional synthetic methods fall short on versatility, making systematic evaluation of cathode materials extremely challenging. Different synthetic factors must be taken into consideration each time a cathode material is made by a different method.

Herein, we developed a novel polyol-mediated synthesis process that is versatile enough to prepare three cathode materials with layered, spinel, and olivine crystal structures. Developed by Fievet and co-workers in the 1980s, polyol synthesis has been widely used in recent decades, but its scope has been mostly limited to the synthesis of simple metals and metal oxides.[43,44] In this method, the polyol medium acts as a chelating agent, a solvent, and a reducing agent, guaranteeing a stable dispersion of nanoparticles with controlled size distribution.[45] In this work, our group has extended this synthesis method to develop more complex metal oxides used as cathode materials in batteries. Polyol synthesis yields completely dispersed cathode nanoparticles with a narrow particle size distribution and competitive electrochemical performance. With the growing interest for solid state lithium batteries, cathode materials with dispersive morphology are strongly desirable as they can provide more intimate solid-solid contact. Using a combination of powder X-ray diffraction (XRD), high-angle annular dark-field scanning transmission electron microscopy (HAADF-STEM), and energy dispersive spectroscopy (EDS), we confirmed high crystallinity and uniform elemental distribution for all three polyol-synthesized cathode materials. Finally, HAADF-STEM images and electron energy loss spectroscopy (EELS) for cycled NMC material were collected to confirm its structural stability after charge-discharge cycling processes. Based on the results of these three polyol-synthesized cathode materials, we believe that the polyol method can provide a valuable platform for evaluating high-

performance, nano-dispersed cathode materials for LIBs. Furthermore, using a combination of *in situ* and *ex situ* characterizations, we have constructed a comprehensive picture of how the reaction progresses during each step of the synthesis. In the case of layered NMC, polyol-mediated solution yields a core/shell structure with Ni-Co alloy nanocrystals surrounded by Mn- and Li-embedded organic matrix. Using *in situ* XRD, the progression of intermediate phases during the post heat treatment were analyzed with respect to the temperature. The detailed knowledge of the reaction mechanism will help to efficiently provide feedback to researchers, such as controlling reaction temperature or heating rate, to eventually find the most optimized synthetic conditions for polyol process.

3.2 Experimental

3.2.1 Synthesis

Synthesis for cathode nanoparticles is a two-step process which involves: 1) preparation of the precursors via polyol solution reaction and 2) heat-treatment to complete the phase transformation and eliminate impurities.

$LiNi_{0.4}Mn_{0.4}Co_{0.2}O_2$ nanoparticles: Transition metal acetates - $Ni(CH_3COO)_2 \cdot 4H_2O$ (0.012 mol), $Mn(CH_3COO)_2 \cdot 4H_2O$ (0.012 mol), and $Co(CH_3COO)_2 \cdot 4H_2O$ (0.006 mol) - and $LiOH{\cdot}H_2O$ (0.0345 mol) were mixed in 80 ml of triethylene glycol along with citric acid (0.045 mol). The mixture was heated at 230 °C with constant stirring for 3 hours in a round bottom flask connected to a reflux. The resulting solution was washed with ethanol several times with a centrifuge and subsequently dried at 80 °C overnight. As-obtained precursors were decomposed at 450 °C for 12 hours and then annealed as a pellet for 5 hours at 850 °C in air.

$LiNi_{0.5}Mn_{1.5}O_4$ nanoparticles: $LiNi_{0.5}Mn_{1.5}O_4$ was synthesized with stoichiometric ratio of $Ni(CH_3COO)_2 \cdot 4H_2O$ (0.0075 mol), $Mn(CH_3COO)_2 \cdot 4H_2O$ (0.0225 mol), and

$LiOH{\cdot}H_2O$ (0.015 mol) in 100 ml of tetraethylene glycol and citric acid (0.030 mol). The mixture was heated at 230 °C with constant stirring for 3 hours. The precipitate was washed with ethanol and subsequently dried at 80 °C for overnight. As-obtained precursors were decomposed at 450 °C for 12 hours and then annealed as a pellet for 1 hour at 800 °C in air.

$LiCoPO_4$ nanoparticles: LiH_2PO_4 (0.015 mol) and $Co(CH_3COO)_2 \cdot 4H_2O$ (0.015 mol) were added as stoichiometric ratio in 100 ml of tetraethylene glycol along with 0.030 moles of polyvinylpyrrolidone (MW = 58000). The mixture was heated at 270 °C with constant stirring for 3 hours. The precipitate was washed with ethanol and subsequently dried at 80 °C overnight. As-obtained precursors were decomposed at 450 °C for 12 hours and then annealed as a pellet for 5 hours at 700 °C in air.

3.2.2 *Ex situ* Powder X-ray Diffraction

Powder X-ray diffractions (XRD) of NMC and LNMO samples were collected on a laboratory X-ray diffractometer, Bruker D8, using a Cu K_α radiation. The data was collected by continuous scanning of a detector covering an angular range from 10.0 °C to 80.0 °C with a scan rate of $0.02\,^\circ\,s^{-1}$ with Cu K_α radiation ($\lambda = 1.540\,59$ Å). In the case of LCP, the data was collected on a Bruker APEX II Ultra diffractometer equipped with Mo K_α radiation ($\lambda = 0.710\,73$ Å) at the UCSD X-ray Crystallography Facility. Diffraction images were merged/integrated in DIFFRAC.EVA (Bruker, 2018) to produce 2d-plots.

All Rietveld refinements were conducted with a pseudo-Voigt profile using FullProf software.

3.2.3 Inductive coupled plasma atomic emission spectroscopy (ICP-AES)

The amount of Li and transition metal ions (Ni, Co, Mn) was analyzed by inductive coupled plasma atomic emission spectroscopy (ICP-AES, Perkin Elmer Plasma 3700). The ICP-AES equipped with two monochromators covering the spectral range of $167 - 785\,\mathrm{nm}$ with a grated ruling of 3600 lines/mm. The system can analyze range of less than 1 part per billion.

3.2.4 Scanning electron microscopy (SEM)

The particle sizes and morphologies were checked using ultrahigh resonance scanning electron microscope (FEI Apreo SEM) at an acceleration voltage of $5\,\mathrm{kV}$. The sample has been coated by sputtering with iridium prior to the measurement.

3.2.5 Brunauer-Emmett-Teller (BET)

N_2 gas physisorption analysis was performed with a Quantachrome Autosorb – iQ/MPXR surface area and porosity analyzer. Each sample was loaded into a quartz sample tube, inserted into the machine, and was degassed under vacuum at $80\,^{\circ}\mathrm{C}$ for 8 hours prior to the measurement.

3.2.6 Electrochemistry

For the composite electrode fabrication, the slurry consisting of 80 wt.% active materials, 10 wt.% acetylene carbon black, and 10 wt.% poly(vinylidene fluoride) (PVDF) in N-methyl pyrrolidone (NMP) was coated on an aluminum foil current collector and then dried overnight in a vacuum oven at $80\,^{\circ}\mathrm{C}$. As-prepared electrodes were punched, pressed uniaxially, dried again at $80\,^{\circ}\mathrm{C}$ for 6 hours and then stored in an argon-filled glovebox

(H_2O level of <1 ppm) (MBraun, Germany) before cell assembly. For the electrochemical characterizations, lithium metal was used for the negative (counter) electrode with Celgard separator. The electrolyte was a 1-M solution of lithium hexafluorophosphate ($LiPF_6$) in a 3:7 volume mixture of ethylene carbonate (EC) and dimethyl carbonate (DMC). The cell used for the electrochemical tests was assembled in a glove box (MBraun, Germany) filled with purified argon gas. The as-prepared cell was charged and discharged in the voltage ranges of $2.5-4.3\,\mathrm{V}$ and $2.5-4.7\,\mathrm{V}$ for NMC, $3.5-4.85\,\mathrm{V}$ for LNMO, and $2.8-4.95\,\mathrm{V}$ for LCP. Theoretical capacity was assumed to be $200\,\mathrm{mA\,h\,g^{-1}}$ for NMC, $146.7\,\mathrm{mA\,h\,g^{-1}}$ for LNMO, and $167\,\mathrm{mA\,h\,g^{-1}}$ for LCP. An Arbin battery cycler was employed to carry out all the galvanostatic cycling tests.

3.2.7 Transmission Electron Microscopy

High-resolution STEM images and EELS of pristine NMC, LNMO, and LCP and cycled NMC were carried out using the double aberration-corrected scanning TEM (TEAM 0.5) operated at an acceleration voltage of 300 kV installed at the Molecular Foundry at Lawrence Berkeley National Laboratory. All annular dark-field STEM micrographs were recorded in TEAM 0.5 with a convergence angle of 30 mrad and a probe size of $<1\,\text{Å}$ after fine-tuning of the probe corrector at 300 kV. EDS/EELS elemental mappings and as-synthesized NMC precipitate characterizations were performed on a double aberration-corrected scanning TEM (JEOL JEM-ARM300CF) at 300 kV installed at the UC Irvine Materials Research Institute (IMRI). To minimize possible electron beam irradiation effects, all the EELS and EDS spectra presented in this work were acquired from areas without pre-beam irradiation.

3.2.8 Synchrotron XRD and pair distribution function (PDF) analysis

X-ray scattering data were recorded using high-energy X-rays ($\lambda = 0.2113\,\text{Å}$) provided by beamline 11-ID-B at the Advanced Photon Source at Argonne National Laboratory. Powders were loaded in amorphous SiO_2 tubes and placed in the flow-cell/furnace for heating under controlled atmosphere.[46] Air (1 cc/min) was flown through the tube as temperature was increased up to 850 °C in 10 °C steps. To more closely resemble high-temperature treatment condition, another set of experiment was conducted with the pre-heated sample. This sample was heated at 450 °C for 12 hours and cooled down back to room temperature. Air (4 cc/min) was flown as the temperature was increased up to 900 °C in 50 °C steps. For both sets of data, 2D images were recorded in transmission geometry using an amorphous-Si detector, and integrated into 1D patterns using GSAS-II,[47] using CeO_2 or LaB_6 standards as calibrant. At each temperature step, data was recorded at two sample-to-detector distances to provide Q ranges suitable for XRD and atomic pair distribution function (PDF) analyses. PDFs ($Q_{max} = 24\,\text{Å}^{-1}$) were calculated using PDFgetX3, and modeled using PDFgui.[48,49]

Le Bail refinements

Lattice parameters of the fcc ($Fm\bar{3}m$) phase identified in the NMC442 precipitate and lattice parameters of the spinel intermediate ($I41/amd$) identified at 230 °C, were obtained from Le Bail refinements of the synchrotron XRD data using TOPAS Academic V6. Diffuse scattering intensity from amorphous SiO_2 tubes was fit using a series of pseudo Voigt functions and an 8-term Chebyshev-type function. The peak profile was fit using CS_L/CS_G macros defined in TOPAS.

PDF refinements

Parameters included lattice parameters, isotropic atomic displacement parameters, scale factor and spdiameter. The spdiameter parameter accounts for the decrease of the PDF amplitude with increasing r due to limited diameter of spherical scattering domains. The occupancies of Ni/Co were fixed to 1 and their relative occupancy was ignored considering their similar scattering factors. The Q_{damp} (correction for PDF dampening due to instrumental limitations) was obtained from a Ni reference. The weighted reliability factor R_w characterizes the agreement between the model and the data, with smaller value corresponding to better a fit.

Rietveld refinements

High-temperature heat treatment for 450 °C pre-heated sample was analyzed by the Rietveld method. The cell parameter refinements were carried out with a pseudo-Voigt profile using Fullprof software in the full pattern matching mode with WinPLOTR.[50,51] From 850 °C, SiO_2 tube crystallizes, so the refinement was performed after excluding region between $3.3 - 3.9°$. More details can be found in Table 3.7.

3.2.9 Soft XAS

Soft X-ray absorption spectroscopy (sXAS) experiments were performed in total electron yield (TEY), total fluorescence yield (TFY) and partial fluorescence yield (PFY) modes using the iRIXS endstation at beamline 8.0.1 at the Advanced Light Source (ALS) at Lawrence Berkeley National Laboratory (LBNL).[52] The X-ray absorption spectra were recorded in TEY mode using the sample drain current, TFY mode using a channeltron, and PFY mode using the high throughput spectrograph (htRIXS). These modes provide surface (TEY) and bulk (TFY/PFY) sensitivity. All spectra were normalized to the

current from a reference Au-coated mesh in the incident photon beam. For the Mn L_3-edge, photon energies were normalized to a TiO_2 reference. For the Co and Ni L_3-edges, photon energies were normalized to a Ni-metal reference. Previously reported Mn L_3-edge spectra for MnO, Mn_2O_3, and Li_2MnO_3 are used as Mn^{2+}, Mn^{3+}, and Mn^{4+} references, respectively.[53] Metallic Ni and Co films mounted on the iRIXS manipulator were used as Ni^0 and Co^0/Co^{2+}, respectively, with the Co film having a slightly reduced Co^{2+}-like surface. Pristine commercial $LiNi_{0.8}Co_{0.15}Al_{0.05}O_2$ (NCA) powder was used as a Ni^{3+} and Co^{3+} reference.

3.3 Results and Discussion

3.3.1 Material Characterization

The synthesis process of the polyol method is schematically shown in Figure 3.2a. The precipitate is obtained after the high-temperature polyol solution reaction. The as-obtained precipitates have three distinct colors - light brown (NMC precursor), greyish brown (LNMO precursor), and light purple (LCP precursor) – due to different compositions. Afterwards, all precipitates go through a two-step heat treatment process. The polyol medium acts as a low solubility solvent, chelating agent, and stabilizing agent at the same time during the reaction.[54] Such conditions are favorable to control the nucleation and growth of the synthesized particles. As a result, the SEM micrographs show that all three polyol-synthesized cathodes have highly dispersed nanoparticles with narrow size distribution (Figure 3.2b-d). Dispersive nanoparticles are ideal for any surface-interface study, since there is no micron-sized meso-structure morphology present in the sample. Such morphology confirms that polyol synthesis method has a potential to provide an excellent synthetic platform for various fundamental studies on cathode nanoparticles. Polyol-synthesized NMC and LNMO cathodes are highly homogeneous network of nanoparticles with 138 and

180 nm in diameter with 40.9 and 41.7 nm for standard deviations, respectively (Figure 3.3). Polyol-synthesized LCP has slightly larger particles which are around 477 nm in diameter with wider standard deviation of 68.6 nm, but it is still absent of any secondary meso-structure. Figure 3.4 clearly shows the difference in the morphology between commercial and polyol-synthesized NMC. Without a secondary meso-structure, polyol-synthesized NMC has five times more surface area ($2.83\,m^2\,g^{-1}$) than commercial NMC ($0.5\,m^2\,g^{-1}$) and possibly lower tap density. Similarly, BET measurements shows that polyol-synthesized LNMO and LCP have surface areas of 4.13 and $8.13\,m^2\,g^{-1}$. Indirect correlation of particle size and surface area can come from possible aggregation for polyol-synthesized NMC and

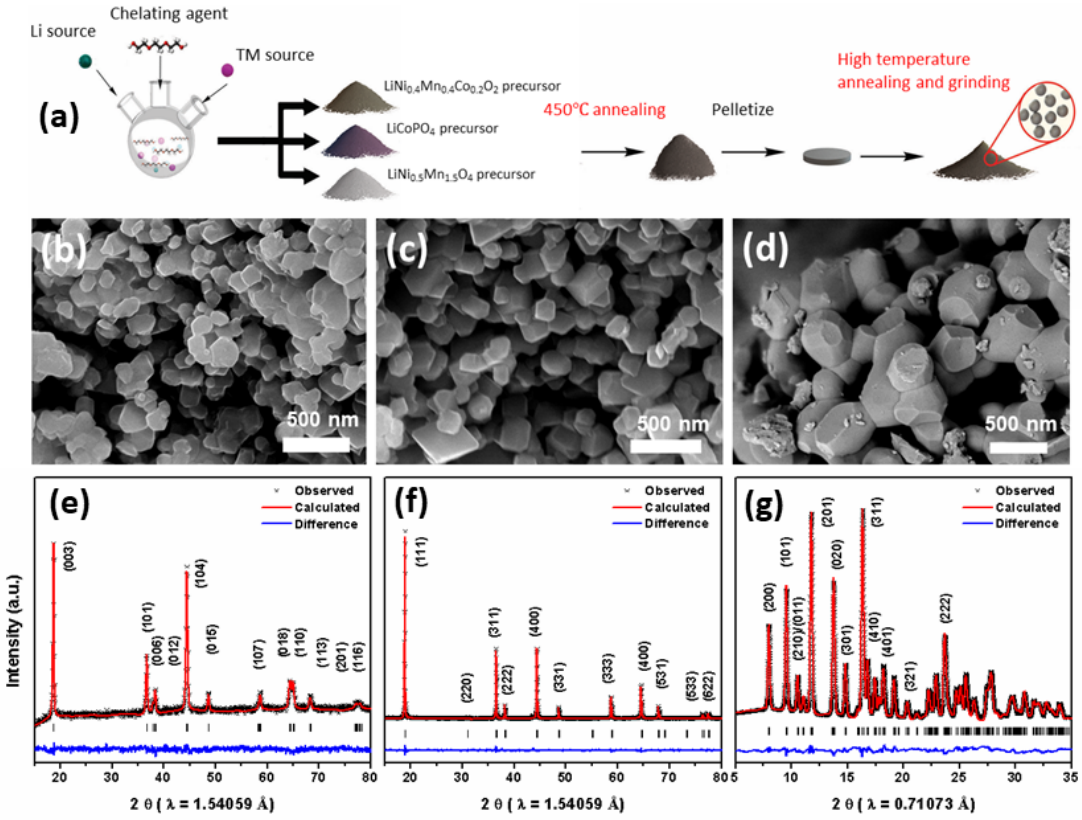

Figure 3.2: (a) Polyol synthesis reaction schematic, morphology, and the Rietveld refinement results of powder X-ray diffraction pattern collected for polyol-synthesized (b, e) layered NMC, (c, f) spinel LNMO, and (d, g) olivine LCP materials.

LNMO as commonly observed in nanoparticle synthesis.[55–57] Small particle size increases the contact area with the electrolyte for charge transfer and shortens Li-ion diffusion length, thus enhancing the rate capability as described in a later section.[58]

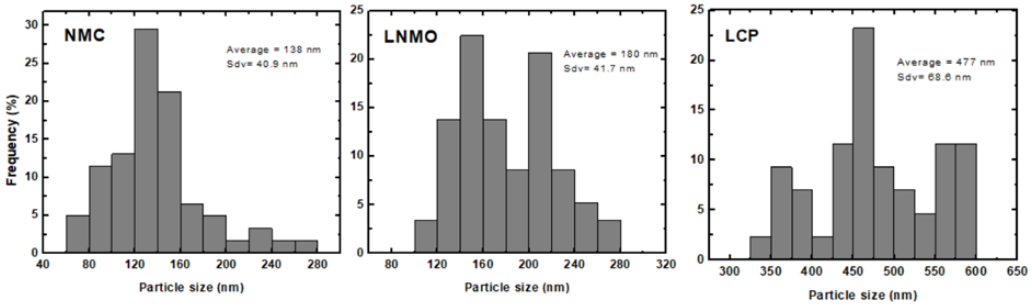

Figure 3.3: Polyol-synthesized cathodes particle size distribution (in diameter) obtained from SEM micrographs using the Image J software.

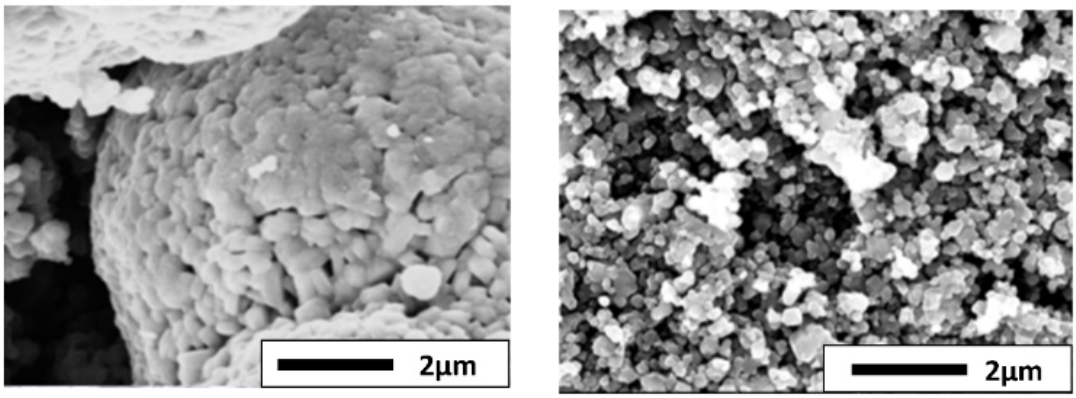

Figure 3.4: SEM micrographs of commercial NMC (left) and polyol-synthesized NMC (right).

The XRD analyses of the synthesized NMC, LNMO, and LCP are shown in Figure 3.2e-g. Rietveld refinements were performed for each sample to confirm their crystal structure. The corresponding crystallographic parameters are tabulated in Table 3.1. Results confirm pure phase of layered NMC, spinel LNMO, and olivine LCP obtained through the polyol method, as all peaks are indexed by the expected space groups with no indication of crystalline impurities. In the case of NMC, all diffraction peaks in the

pattern are indexed by a rhombohedral layered phase with the $R\bar{3}m$ space group. XRD pattern of polyol-synthesized LNMO exhibits peaks characteristic of the cubic spinel phase with the $Fd\bar{3}m$ space group. As a disordered LNMO spinel material, the Li sits in the tetrahedral sites with Ni and Mn randomly occupying in 16c octahedral sites. The minimal intensity of the (220) peak indicates low occupation of transition metals in tetrahedral sites.[59] This was consistent with our Rietveld refinement value, which only shows 1.7% of cation mixing. Nickel-rich rocksalt phase is a common concomitant impurity phase present in this material after high temperature heat-treatment,[60,61] but no sign of any impurity was detected in the XRD pattern of our synthesized material, confirming the excellent purity. The short annealing time (800 °C, 1 h) minimizes Li evaporation, therefore, limits the formation of $Li_xNi_{1-x}O$ impurity.[62,63] Lastly, XRD patterns of the synthesized LCP particles are shown in Figure 3.2g. All the diffraction peaks are indexed by the *Pnma* space group. The olivine structure is based on a distorted hexagonal close-packed oxygen array with P atoms occupying tetrahedral sites and Li and Co occupying the 4a and 4c octahedral sites, respectively.[64–66]

Aberration-corrected STEM was used to directly observe the local crystal structures of NMC, LNMO, and LCP at the atomic scale. As polyol-synthesized cathodes are completely dispersed nanoparticles, no special sample preparation for STEM was needed.[67] Figure 3.5 shows representative HAADF-STEM images of the polyol-synthesized cathodes in the pristine state. As shown in the image of NMC (represented by the blue frame) taken along the [100] zone axis, the position of transition metals in 3a sites are atomically resolved, which confirms a well-defined layered structure. Li (3b sites) and O (6c sites) are not visible due to their low atomic mass in Z-contrast HAADF-STEM images.[68] According to the Rietveld refinement, polyol-synthesized NMC features 6.47% of Li/Ni cation mixing. A small degree of cation mixing is also observed in the few atomic layers of the surface region in high resolution images, as previously observed in other studies.[69] Representative

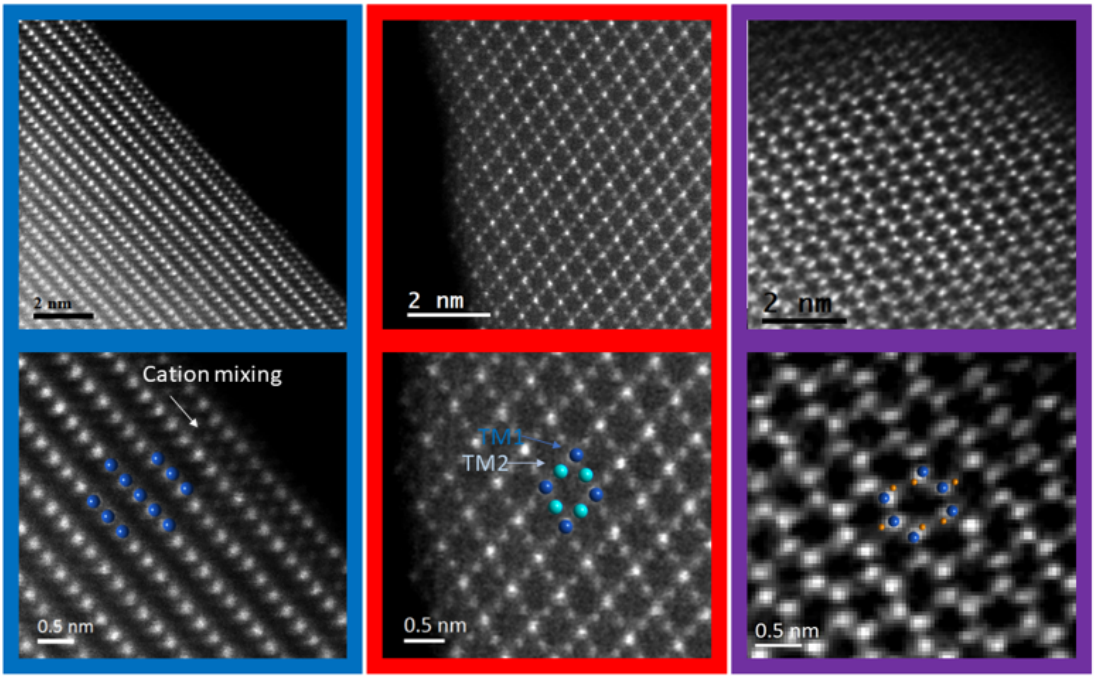

Figure 3.5: HAADF-STEM images of the polyol-synthesized layered NMC (blue frame), spinel LNMO (red frame), and olivine LCP (purple frame) materials. Dark and light blue color circles represent transition metal (Ni, Co, or Mn), while orange represents phosphorus ions.

HAADF-STEM images of the pristine LNMO were taken along the [110] zone axis (red frame). This direction allows the position of transition metal (TM) heavy atomic columns to be identified clearly as a diamond configuration. As shown, two different transition metal columns can be assigned as TM1 and TM2. Stronger contrast is observed in TM1 than in TM2 column position, because the stacking density of the TM1 is twice to that of TM2.[70,71] The well-defined spinel structure in the bulk material extends to the surface. Lastly, the purple color frame in Figure 3.5 shows synthesized LCP viewed along the [010] projection. The [010] direction has been chosen because it allows for the identification of the position of Co, P, O, and Li with separate aligned columns. Bright contrast produced by Co atoms can be clearly observed in a hexagon configuration under the HAADF STEM mode. Because P atomic columns are adjacent to the Co site, Co and P cannot be distinctively resolved.[72] The distribution of transition metal at the atomic level is extremely important

as it correlates closely with the materials' rate capability and cyclability.[41,73,74] Zheng *et al.* found that a careful choice of synthetic conditions applied for the precursor preparation can mitigate the transition metal segregation, thus enhancing the electrochemical performance of layered oxides.[41] Motivated by this study, we investigated the local chemical species in both the bulk and surface of the pristine cathode materials using energy dispersive X-ray spectroscopy in STEM. Polyol method is a one-pot synthesis method, which involves all the transition metal and lithium precursors reacting together at high temperature. As shown in Figure 3.6, all the elements in the polyol-synthesized NMC, LNMO, and LCP are uniformly distributed, with no apparent segregation. Additionally, the stoichiometry of the polyol-synthesized NMC, LNMO, and LCP were confirmed with ICP-AES, and is close to their nominal stoichiometry, with variances in the range of experimental error. These results are presented in Table 3.2.

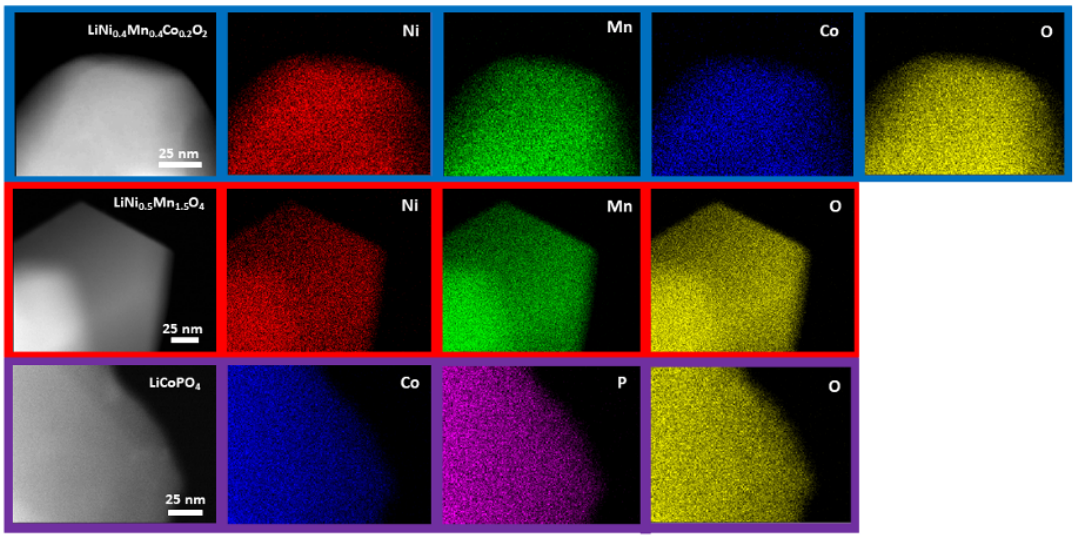

Figure 3.6: STEM/EDS mapping of a particle shows a uniform distribution of all constituents for layered NMC (blue), spinel LNMO (red), and olivine LCP (purple) materials.

3.3.2 Electrochemical Characterization

The three polyol-synthesized cathode materials were characterized by a series of electrochemical properties measured in Li half-cells. Figure 3.7 shows electrochemical properties and redox potentials for NMC, LNMO, and LCP. Layered NMC exhibits typical galvanostatic charge-discharge profile between 2.5 and 4.3 V with charge and discharge capacities of 158 $\mathrm{mA\,h\,g^{-1}}$ and 140 $\mathrm{mA\,h\,g^{-1}}$ respectively for C/10. The corresponding differential capacity versus voltage (dQ/dV) curves are plotted in Figure 3.7c. The broad peak between 3.7 V and 4.2 V on the 1$^{\mathrm{st}}$ charge is related to the oxidation of Ni ions (Ni^{2+}/Ni^{4+}) and Co ions (Co^{3+}/Co^{4+}), and the reduction peak found in similar potential indicates reversible Li insertion in the layered structure.[75] After 50 cycles, the material still maintains 87.1% of its initial capacity with 122 $\mathrm{mA\,h\,g^{-1}}$. In the case of spinel LNMO, the material was tested with C/10 between $3.5-4.85$ V. Both the voltage profile and dQ/dV plot clearly show the redox couple of Mn^{3+}/Mn^{4+} (4.0 V) and Ni^{2+}/Ni^{4+} ($4.6-4.8$ V). The peak splitting in $4.6-4.8$ V region is due to two oxidation steps: Ni^{2+}/Ni^{3+} and then Ni^{3+}/Ni^{4+}.[76,77] Spinel LNMO delivers the charge and discharge capacity of 137 $\mathrm{mA\,h\,g^{-1}}$ and 125 $\mathrm{mA\,h\,g^{-1}}$. Even after 50 cycles, the material retained 94.4% of its capacity, showing an excellent cycling stability. Only negligible voltage decay is observed for the 1$^{\mathrm{st}}$ and 50$^{\mathrm{th}}$ cycles as well. Cycling retention for LNMO by polyol far exceeds the same material made by more conventional sol-gel method, which also yields dispersive morphology (Figure 3.8). Lastly, olivine LCP has been tested between $2.8-4.95$ V for C/10. As shown, LCP redox couples correspond to the redox of two two-phase regions, specifically $LiCoPO_4/Li_{0.66}CoPO_4$ (4.8 V) and $Li_{0.66}CoPO_4/CoPO_4$ (4.9 V) versus Li/Li+ during the charge and two corresponding reduction peaks at 4.78 and 4.71 V. In agreement with previously published results, these two steps during charge-discharge are more pronounced at the 50$^{\mathrm{th}}$ cycle than during the 1$^{\mathrm{st}}$ cycle.[78,79] Both oxidation peaks in the initial cycle are shifted to more positive potential when compared with further cycles, which indicates the

slow kinetics of the initial delithiation of $LiCoPO_4$. As shown, LCP has first charge and discharge capacity $137\,mA\,h\,g^{-1}$ and $108\,mA\,h\,g^{-1}$, and high charge and discharge energy density of $646\,W\,h\,kg^{-1}$ and $504\,W\,h\,kg^{-1}$ due to high redox potential. LCP, unfortunately, suffers from poor cycle life, mainly attributed to the parasitic degradation reactions at the interface of the electrode and the electrolyte (Table 3.3). The working potential of LCP far exceeds the stability limit of standard carbonate-based electrolytes ($\sim 4.5\,V$).[66] The decomposition products of the electrolyte form resistive films on the particle surfaces, which hinder lithium intercalation reaction thereafter.

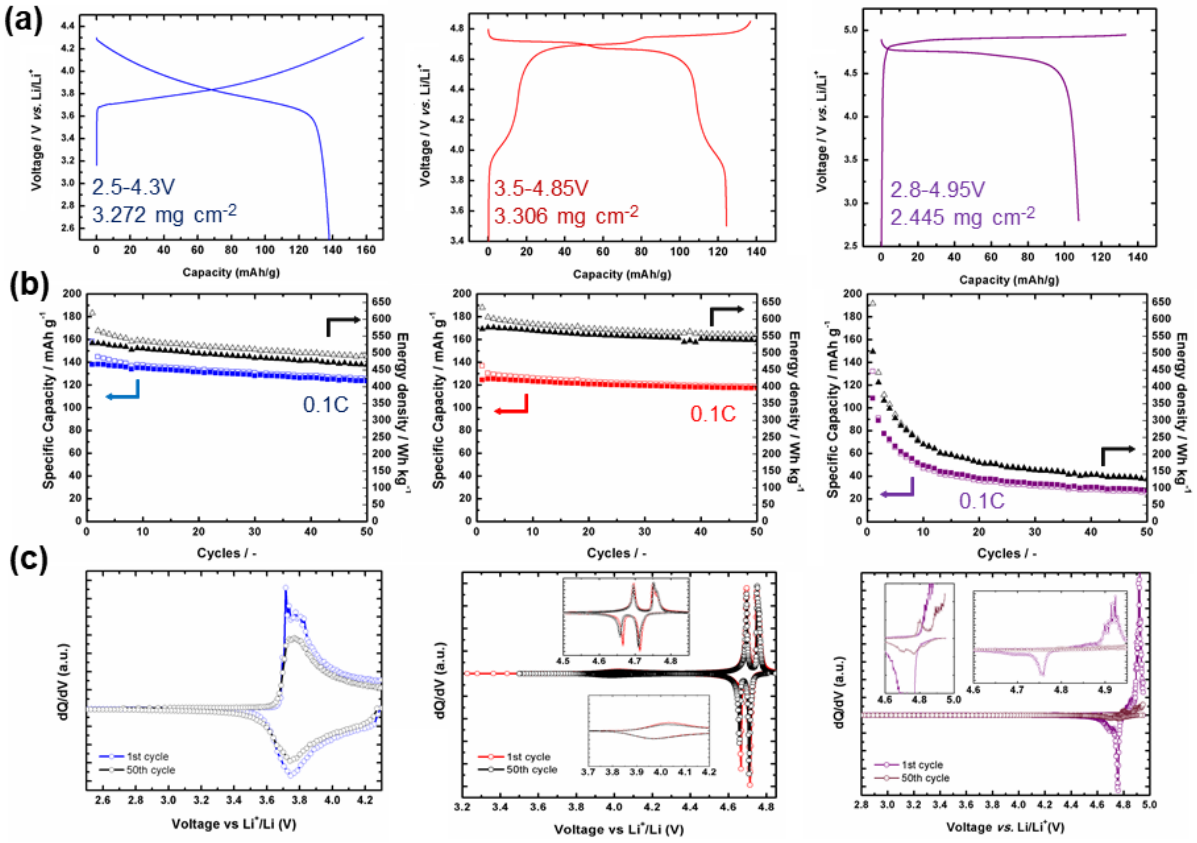

Figure 3.7: (a) First charge and discharge voltage profile, (b) cycling performance, and (c) dQ/dV in the voltage range of $2.5-4.3\,V$ for NMC (blue), $3.5-4.8\,V$ for LNMO (red), and $2.8-4.95\,V$ for LCP (purple).

Similar to spinel LNMO and olivine LCP, layered NMC can also be evaluated with

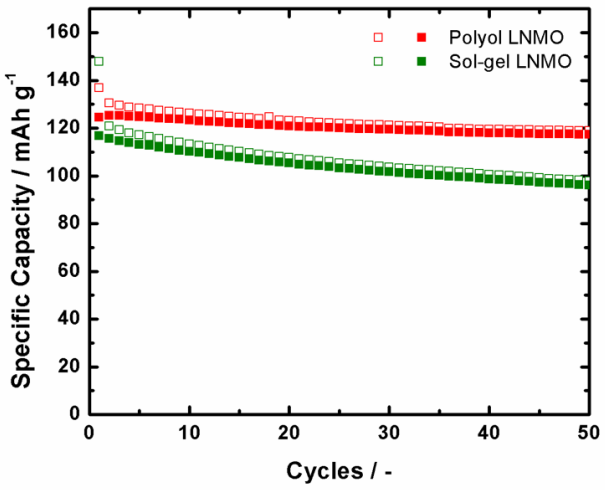

Figure 3.8: Comparison of cycling performance for polyol and sol-gel synthesized LNMO at room temperature.

a high voltage cutoff of 4.7 V. By increasing the operating voltage, polyol-synthesized NMC can reach up to 251 and 207 $\mathrm{mA\,h\,g^{-1}}$ of the first cycle charge and discharge capacity. This corresponds to 1026 and 805 $\mathrm{W\,h\,kg^{-1}}$ of energy density, which exceeds both LNMO (635/571 $\mathrm{W\,h\,kg^{-1}}$) and LCP (646/504 $\mathrm{W\,h\,kg^{-1}}$) materials. Additional studies were therefore performed for NMC to evaluate the material as a next generation storage material with high energy density.

First, we studied the effect of current density on the charge-discharge profile of polyol-synthesized NMC. To achieve high rate rechargeable batteries, many studies have focused on controlling the dimensions of the active particles.[80] Nevertheless, as mentioned earlier, reducing the size by producing nanosized particles has drawbacks as a large surface area could promote undesirable side reactions between active material and electrolyte. Consequently, it remains a great challenge to synthesize the desired nanostructured morphology to fulfill both the energy requirement and cycling stability at the same time. Previous work by Kim *et al* showed that polyol synthesis of $LiFePO_4$ nanoparticles showed excellent capacity retention at high current densities with the monodispersed uniform morphology.[81] Similarly,

our synthesized NMC show excellent capacity retention when charged and discharged at different current rate ranging from C/10 to 10C. To illustrate, the result shows that the discharge capacities could reach 131 $\mathrm{mA\,h\,g^{-1}}$, 123 $\mathrm{mA\,h\,g^{-1}}$, 101 $\mathrm{mA\,h\,g^{-1}}$, and 82 $\mathrm{mA\,h\,g^{-1}}$ for C/3, 1C, 5C, and 10C rate (Figure 3.9). The capacity for all current densities is stable with all maintaining reversible capacity retention ratios above 87% even after 50 cycles. The electrochemical performance is superior to that reported in the literature for pristine $LiNi_{0.4}Mn_{0.4}Co_{0.2}O_2$ material tested under standard conditions, especially at high current density (Table 3.4).[82]

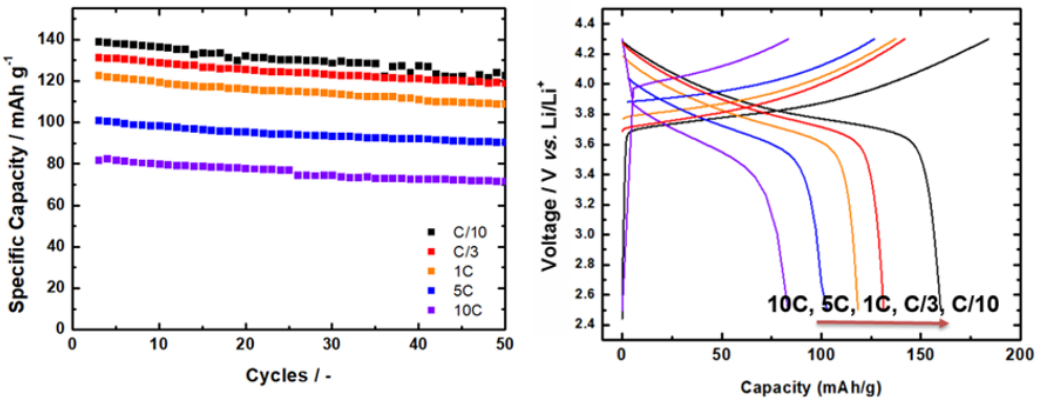

Figure 3.9: Electrochemical performance of polyol-synthesized NMC at various current rates (Charge and discharged at current rate of C/10, C/3, 1C, 5C, and 10C with theoretical capacity of 200 $\mathrm{mA\,h\,g^{-1}}$).

Additionally, we studied the effect of high voltage operation on the cyclability of NMC. Figure 3.10 displays the voltage profile of NMC at high voltage operation ($2.5-4.7\,\mathrm{V}$) with C/10 rate. Although it initially displayed higher specific capacity, the capacity of the NMC electrode continues to decrease during cycling, while lower voltage operation ($2.5-4.3\,\mathrm{V}$) experiences smaller capacity fade. Previous electron microscopy studies show that this high voltage operation in NMC is accompanied by structural transformations at the particle surface from layered to spinel-like and/or rock-salt-like structures. Merely after 1-cycle at 4.7 V cutoff, Lin *et al* observed a surface reconstructed layer from $R\bar{3}m$

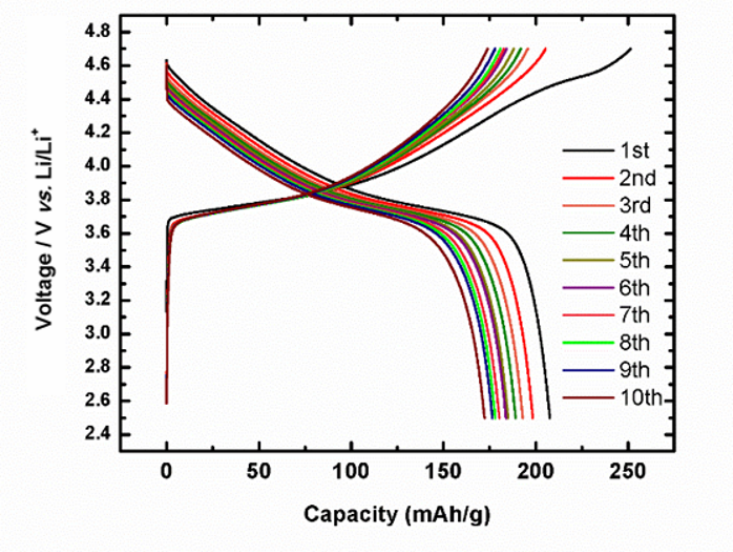

Figure 3.10: Voltage profiles for polyol-synthesized NMC at $2.5-4.7\,\mathrm{V}$ for 10 cycles at C/10.

to $Fm\bar{3}m$.[12] Motivated by this observation, we have investigated the local crystal and electronic structure of the cycled sample using STEM-EELS. Interestingly, even after 10-cycles at $4.7\,\mathrm{V}$ cutoff, the surface structure of some polyol-synthesized NMC particles remains mostly intact, showing a layered structure (Figure 3.11a) similar to the pristine material (shown in Figure 3.5). Multiple regions were analyzed to confirm the consistency of our results (Figure 3.23). Only one out of five particles (Figure 3.11b) showed a surface reconstruction layer for the 10-cycled sample.

Furthermore, EELS was acquired to assess the bulk and surface structure changes of pristine and cycled NMC. EELS data was also collected at several positions to ensure that the results presented in Figure 3.11c are representative of the sample studied. The pre-peak of the O K-edge is associated with the hybridization states between transition metal 3d and oxygen 2p orbitals in the octahedral unit, thus it can be correlated with the oxidation states of transition metals.[12,86] As shown, the oxygen electronic structure is well-maintained both at the bulk and the surface of cycled NMC particles. Such results correlate well with the HAADF-STEM images, since surface reconstruction after cycling

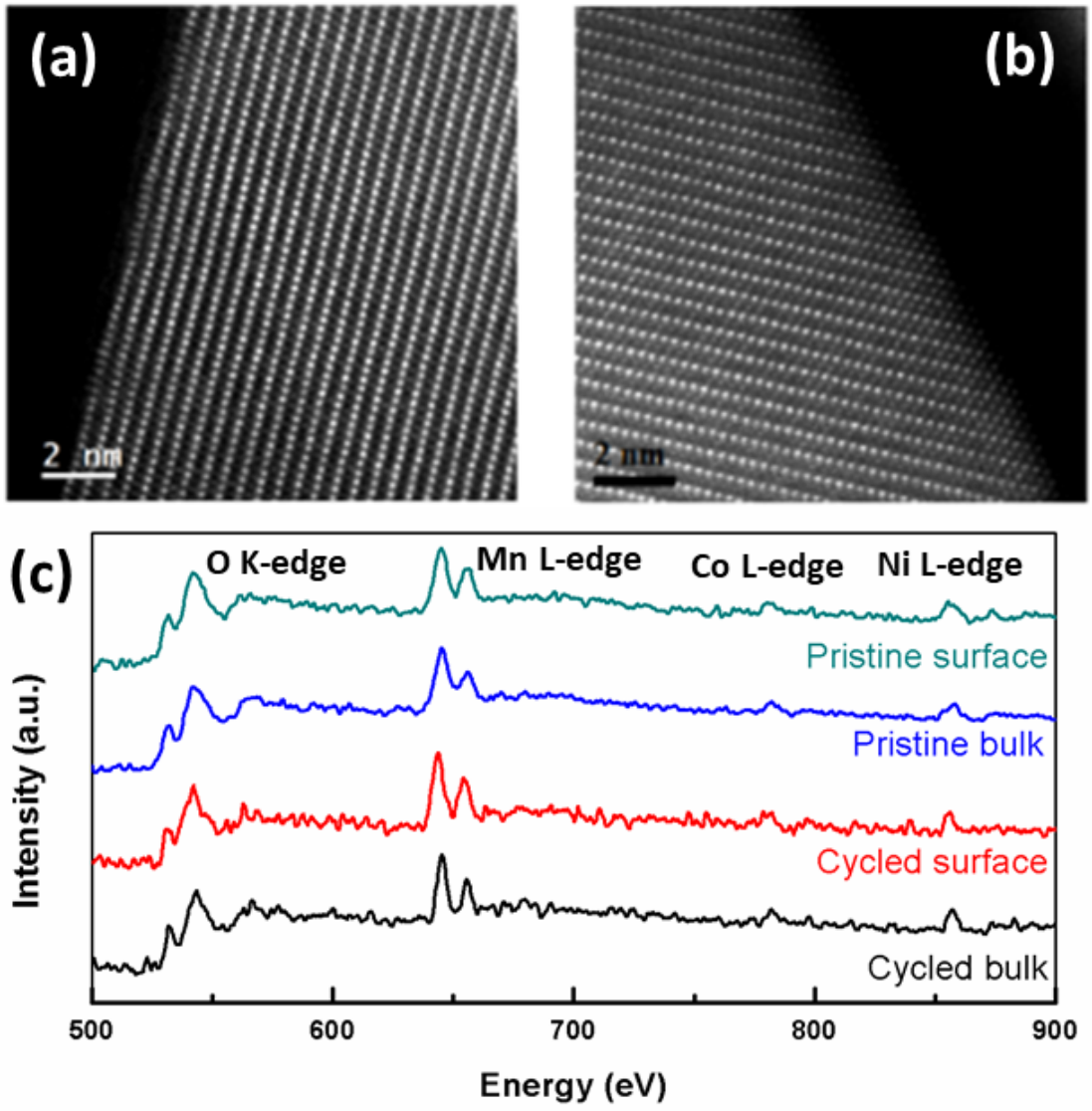

Figure 3.11: HAADF-STEM images and EELS spectra at the surface and bulk regions (c) of NMC cathodes after 10 cycles at C/10 in the voltage range of $2.5 - 4.7\,\mathrm{V}$. (a) and (b) represent different particles observed.

would have led to a reduction of the transition metal valence and oxygen vacancy. Shkrob *et al.* reported that protons from H_2O molecules can exchange with Li ions without changing the lattice symmetry of cathode materials, which leads to the capacity degradation in Li-ion batteries.[87] It is therefore possible that the absence of water during the polyol synthesis helps to prevent proton insertion into NMC structure, creating a more stable atomic

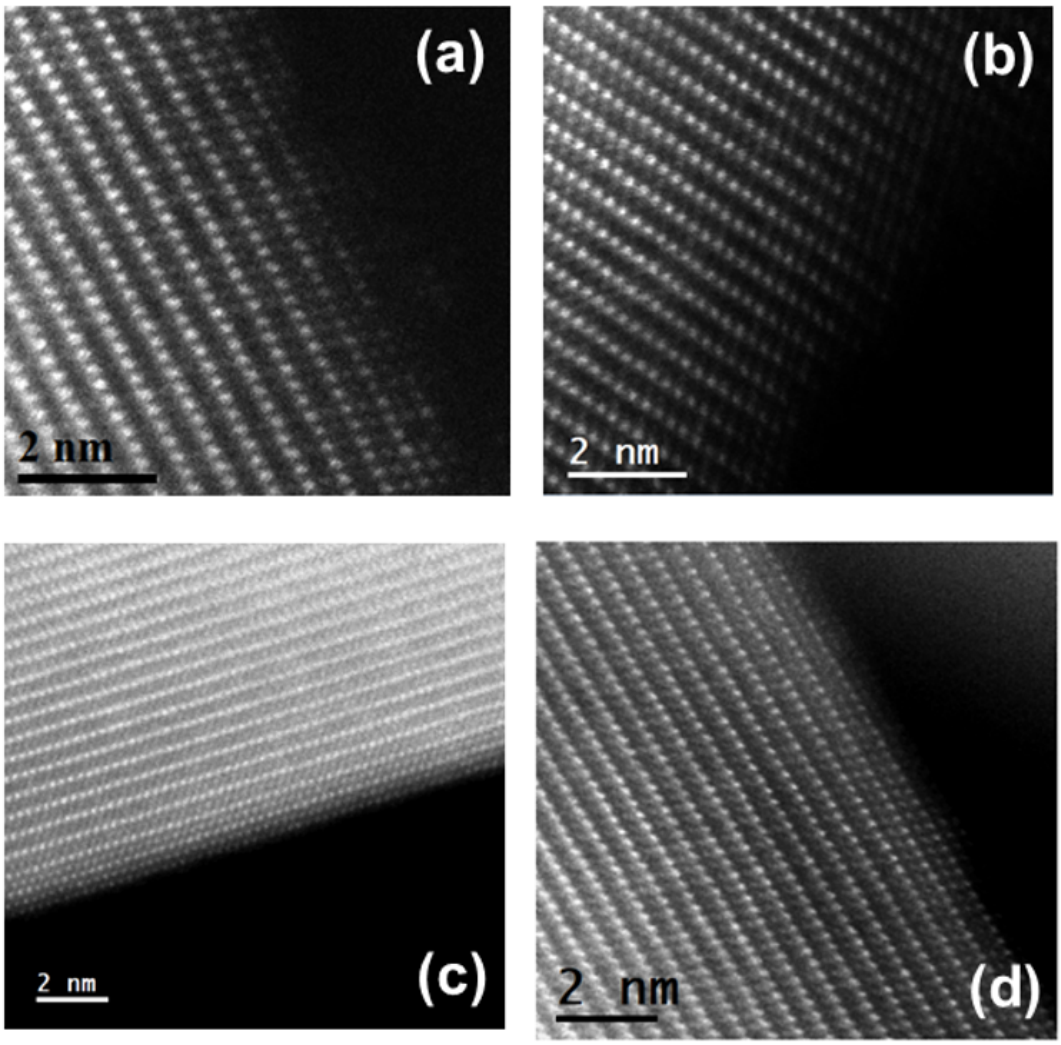

Figure 3.12: Additional HAADF-STEM images of polyol-synthesized NMC after 10-cycles at $2.5-4.7$V with current density of C/10. (a) (b) represents different region for Particle 1. (c) and (d) represents Particle 2 and Particle 3, respectively.

structure in the pristine material that is more resistant to surface reconstruction. Instead of originating from surface reconstruction, continuous capacity degradation for polyol-synthesized NMC could mainly stem from undesirable side reactions with the electrolyte, aggravated by the high state-of-charge and large surface area.[6] We further explored the polyol synthesis mechanism in detail to understand the role of the synthesis conditions on the properties of polyol-synthesized NMC.

3.3.3 Polyol Synthesis Mechanism

Characterization of As-synthesized Precipitate

The precursor was prepared as a one-pot synthesis by first dissolving Li^+, Ni^{2+}, Mn^{2+}, and Co^{2+} ions in the polyol solution. After a high-temperature solution reaction at 230 °C, the precipitate obtained is fluffy in nature, implying that the chelating agent has likely formed a complex with the metal ions in the solid precursor.[88] The typical structural and morphological characterizations of the precipitate are shown in Figure 3.13. After high-temperature polyol solution reaction, HAADF-STEM images reveal that the precipitate is comprised of crystalline nanoparticles of about 5 nm in diameter, completely dispersed in an amorphous organic matrix. Its local chemical composition was analyzed by STEM-EELS mapping (Figure 3.14a). The results show that the synthesized nanocrystals are composed of both Ni and Co, while Mn and O-containing species constitute an amorphous matrix. As the distribution of O is inversely correlated with Ni and Co, it was concluded that in this core/shell-like structure, a Mn-embedded organic "shell" covers a Ni-Co alloy "core". Nanoparticles with only Ni or Co were not observed in other HAADF-STEM images either (Figure 3.16). The closely magnified bright-field image and the corresponding FFT (Figure 3.13c) verified that Ni-Co alloy nanoparticles are well-crystalline with the observed d spacing of 0.20 nm and 0.17 nm between adjacent fringes, corresponding to the (111) and (200) crystal planes of face-centered cubic (fcc) structured Ni-Co alloy.[89–94]

The crystal structure of the precipitate was further analyzed by XRD. The most intense peaks observable on the XRD pattern of the precipitate can be indexed by a face-centered cubic phase (fcc, $Fm\bar{3}m$) with lattice parameter $a = 3.530(2)$ Å as obtained by Le Bail refinement (Figure 3.13a). The value of the lattice parameter obtained here is intermediate between values typically observed for pure Ni metal ($a \approx 3.52$ Å) and Co metal ($a \approx 3.54$ Å), suggesting that Ni and Co form an alloy (Table 3.5). Note that Co

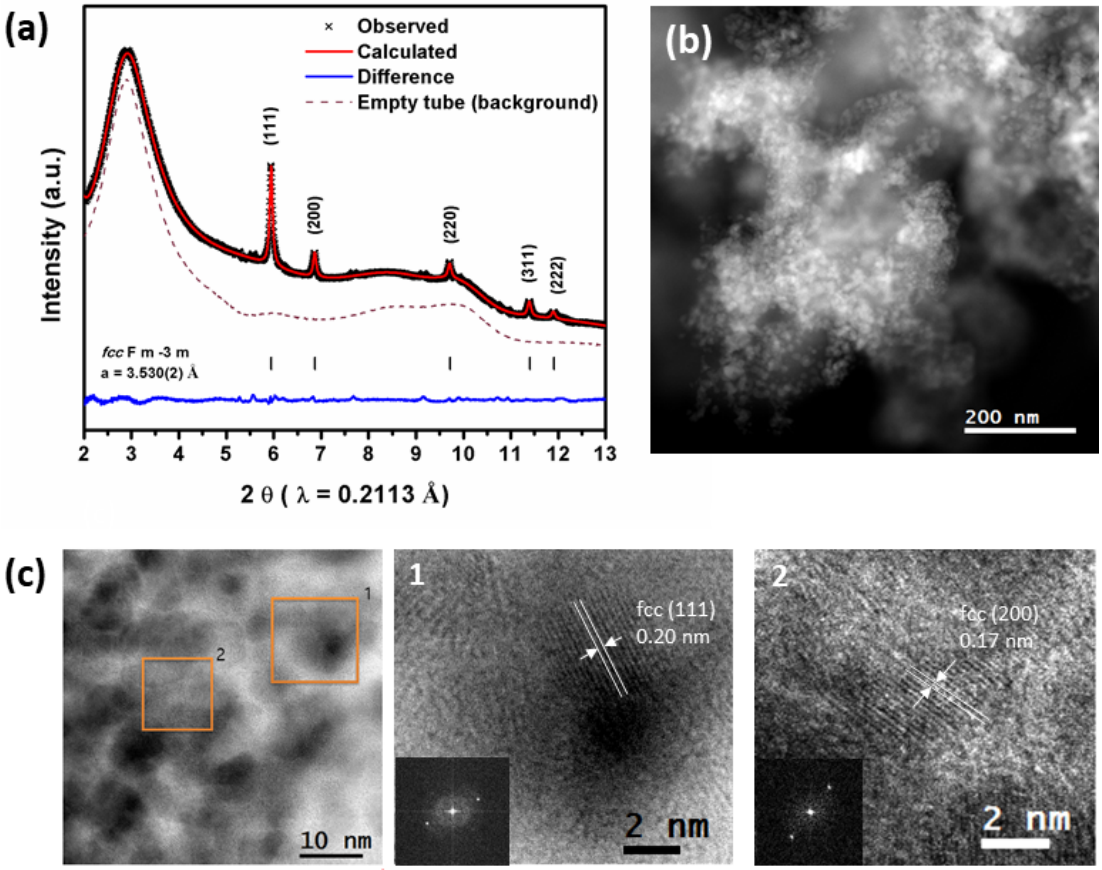

Figure 3.13: Precipitate obtained after polyol-mediated solution reaction characterized by Le Bail Refinement (a) and HAADF images (b). Enlarged bright-field images (c) show crystalline nanoparticles embedded in amorphous matrix.

metal typically stabilizes in hexagonal close-packed (hcp, $P63/mmc$) crystals below 450 °C and in fcc ($Fm\bar{3}m$) crystals above 450 °C. However, the stability of the two phases is heavily influenced by the crystallite size, with smaller crystallite size favoring the fcc polymorph,[95] as we observe here. The residual XRD peaks not indexed by the fcc phase cannot be properly refined by an additional hcp phase, although a hcp phase with lattice parameters $a = 2.659$ Å and $c = 4.354$ Å yields peaks close to those observed experimentally (Figure 3.17). This discrepancy suggest the presence of disorder (e.g. stacking faults) in the hcp-like phase which is likely related to the hcp–fcc intergrowth phenomena previously observed in nanosized Co metal.[96,97]

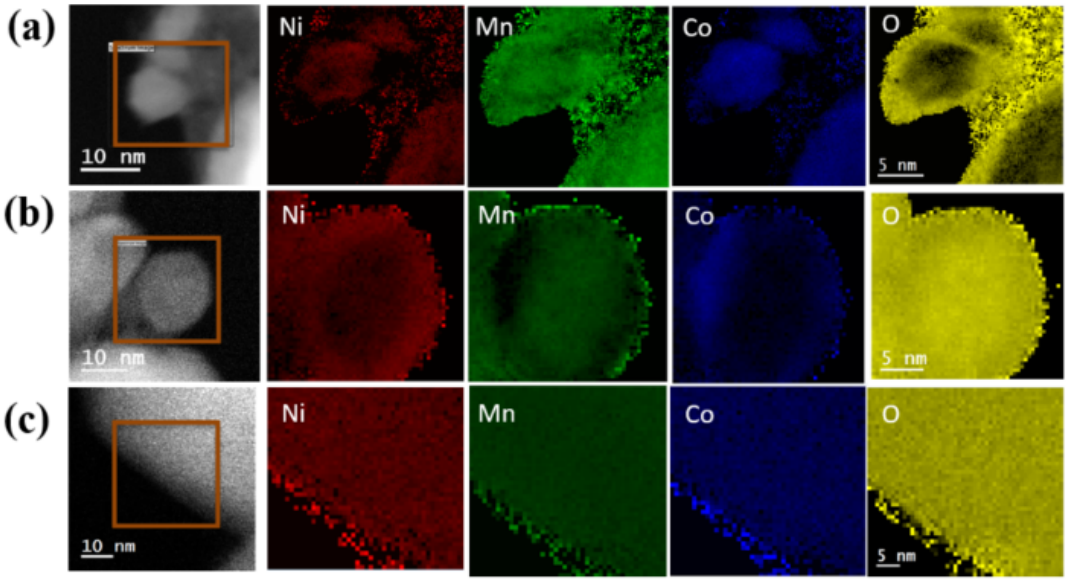

Figure 3.14: STEM/EELS elemental mapping of as-synthesized precipitate before any heat treatment (a), after 450 °C heat treatment (b), and after 850 °C heat treatment (c).

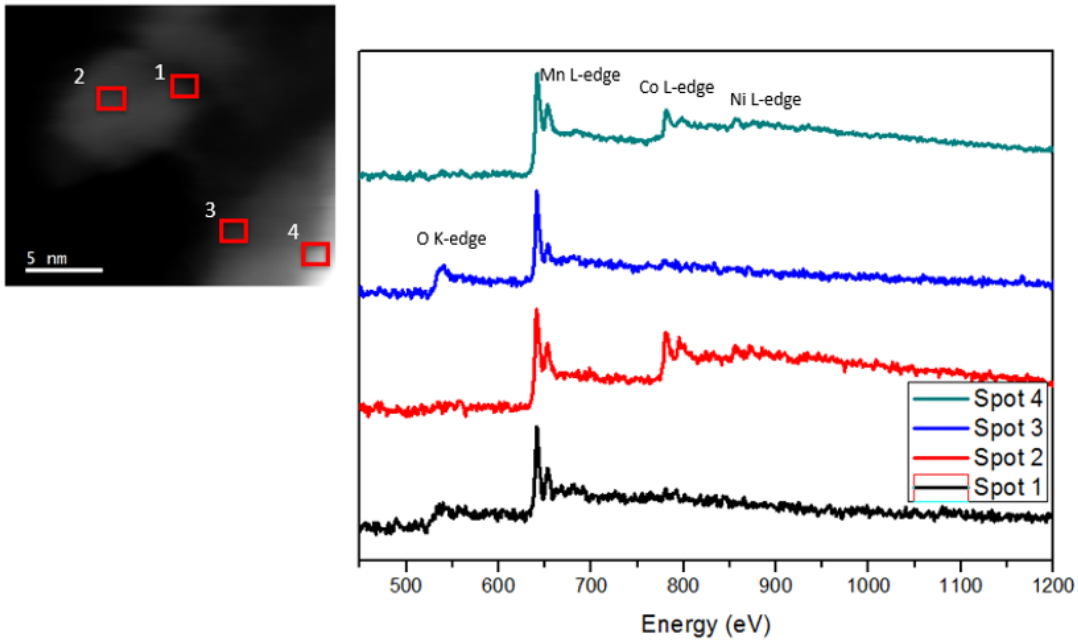

Figure 3.15: EELS Spectra for the precipitate from polyol-mediated solution reaction.

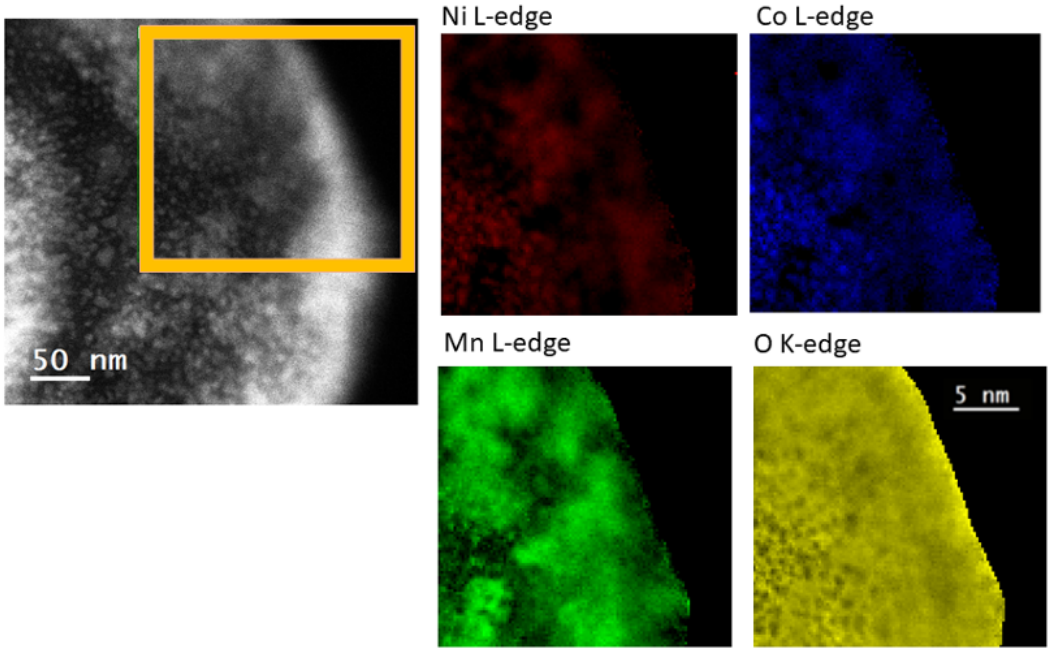

Figure 3.16: STEM/EELS mapping for the precipitate from polyol-mediated solution reaction.

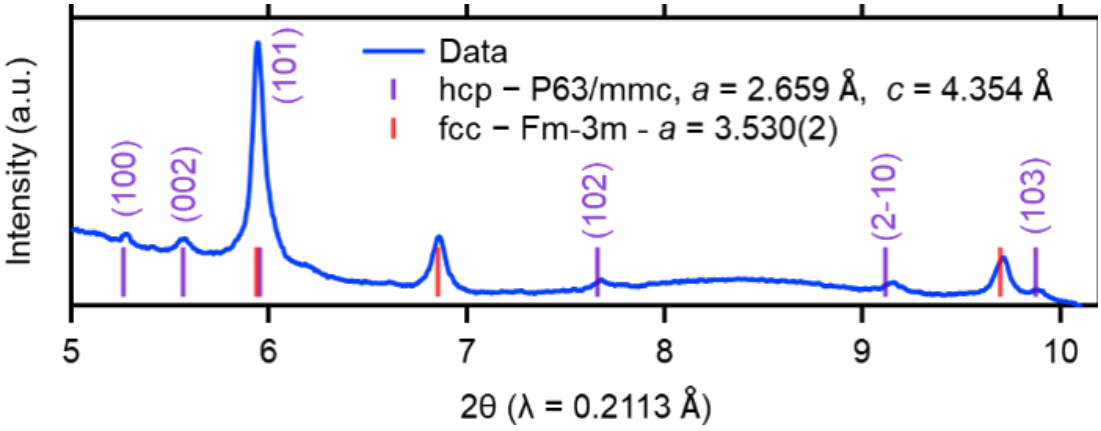

Figure 3.17: Synchrotron XRD data recorded on the polyol-mediated precipitate showing how a hcp ($P63/mmc$) phase shows peaks at 2θ positions close to experimentally observed residual (not fcc) peaks.

Single fcc phase refinement of the PDF data in the intermediate range (15–40 Å) seems to be sufficient to fit the PDF data, as the difference (residual) features a sine-like pattern, suggesting that no other phase is present (Figure 3.18a). Crystallite size is

estimated to be 7(5) nm which is consistent with the HAADF-STEM images (Table 3.6). A two-phase fcc–hcp refinement only marginally improves the quality of the fit, as the R_w decreases from 0.356 to 0.292 (Figure 3.18b). The result of the two-phase fit is characterized by a large standard deviation of the estimated phase fraction — 65 and 35% for the fcc and hcp phases, respectively, with a 27% standard deviation. This further supports the presence of a hcp-like phase in the precipitate. The difference at low r displays the contribution of the Mn-rich and organic species to the PDF (Figure 3.18c). With a coherence size of about 7 Å, the amorphous Mn-rich phase features peaks at 1.3, 2.1 Å which are relatively close to those experimentally observed in Mn-acetate tetrahydrate (1.2 and 2.2 Å),[105] which suggests that Mn is not reduced to its metallic form like Ni and Co. We believe that the unique characteristics of the precipitate described above can be ascribed to the distinctive properties of the polyol medium itself. With a high boiling point, the polyol solvent can reduce dissolved metal cations to synthesize a wide variety of metals, intermetallics, and alloys without the need for high pressure conditions.[44] During the reaction, the solvent, triethylene glycol, reduces both Ni^{2+} and Co^{2+}-ions into an alloy, since these metal cations have similar reductivity.[106,107] On the other hand, Mn^{2+} and Li^{+} keep their original oxidation states and form a precipitate with organic ligands since polyol is not a strong enough reducing agent. The oxidation states of each transition metal (TM) were further verified using soft XAS (Figure 3.19). Here, we present TEY measurements as fluorescence measurements (TFY and PFY) suffer from self-absorption effects that distort the spectra. From comparison with various TM reference compounds, Ni and Mn oxidation states were determined to be 0 and +2, respectively, based on similar energy positions and spectral features. Although Co is expected to be primarily in the metallic state based on XRD, we find sharp spectral features similar to reference Co^{2+} indicating some Co^{2+} in the precipitate. This lineshape likely reflects mixed 0/+2 oxidation state as the broad metallic lineshape is in the same energy range as the sharp Co^{2+} peaks.[108] It is possible that not

all Co-ions are reduced to the metallic state and that a small extent remained embedded in the organic ligands along with the Mn. Smaller concentrations of Co, compared with Mn, Ni, and O, may pose a challenge in detecting Co-ions in our organic "shell" in the EELS elemental mapping described earlier.

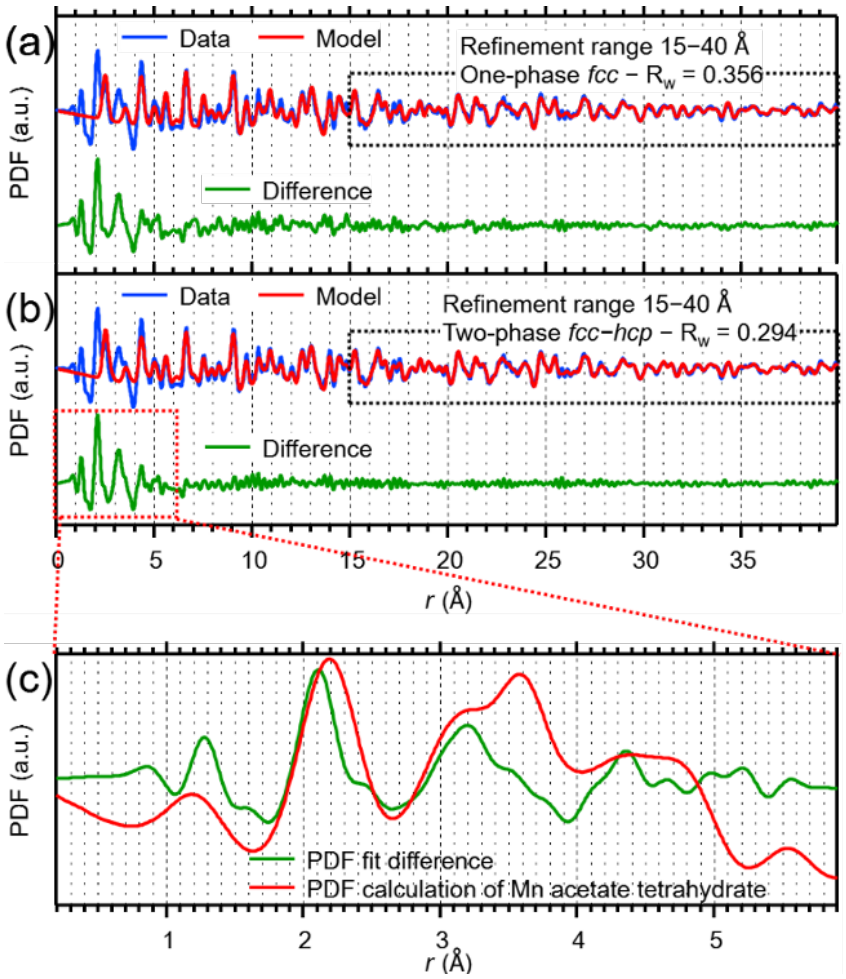

Figure 3.18: Single-phase fcc refinement (15 – 40 Å) of the PDF data recorded on the polyol-synthetized NMC precipitate. (a) Two-phase phase fcc-hcp refinement. (b) comparison of the PDF fit difference and a calculation for Mn acetate tetrahydrate. (c) Results of the (a) - (b) fits are available Table 3.6

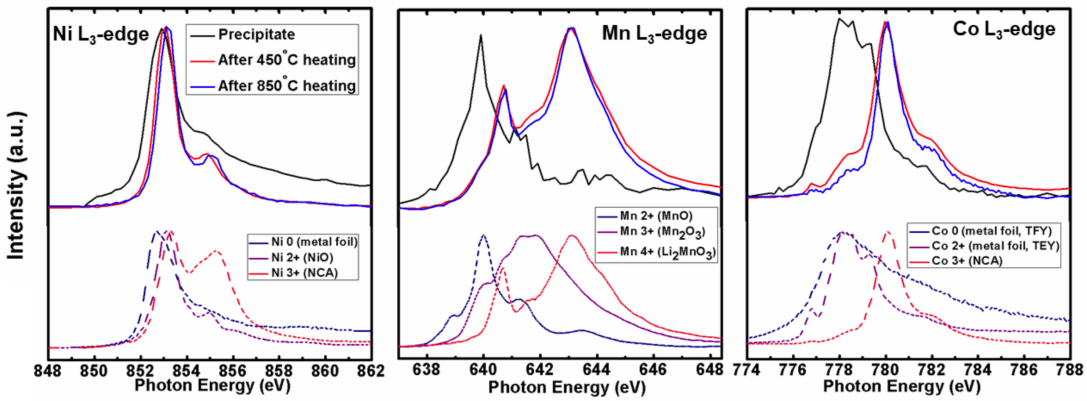

Figure 3.19: Ni, Mn, and Co L3-edge soft XAS spectra of the precipitate, after the first heat treatment at 450 °C, and after the second heat treatment at 850 °C (solid lines) with reference spectra (dash lines).

Structural and Morphological Evolution During the Heat-treatment Process

After the solution reaction, the obtained precipitate goes through the heat treatment process to form the pure layered phase NMC. Although cathode material synthetic methods can vary widely, a heat treatment is one of the most common and important procedures across all methods. Heat treatment conditions influence important material properties such as phase purity, transition metal distribution, particle size, and defect formation. Herein, *in situ* heating XRD studies were conducted to monitor the structural response of a material with the respect to the temperature. Figure 3.23 shows the XRD data recorded during the direct heating of the precipitate. Figure 3.23a represents an image plot of the data recorded in the whole temperature range, while Figure 3.23b shows selected XRD pattern in the $200-450\,^{\circ}\mathrm{C}$ range, where the most obvious structural changes occur. From room temperature to 220 °C, little changes occur besides thermal expansion of fcc and hcp phases observed in the precipitate. The structural changes start to occur around 230 °C. Figure 3.21 shows the subtraction of the XRD pattern collected at 220 °C from the one obtained at 230 °C to more clearly visualize the low intensity peaks appearing at 230 °C. As shown, this pattern can be indexed by a $CdMn_2O_4$-type spinel phase ($I41/amd$) with

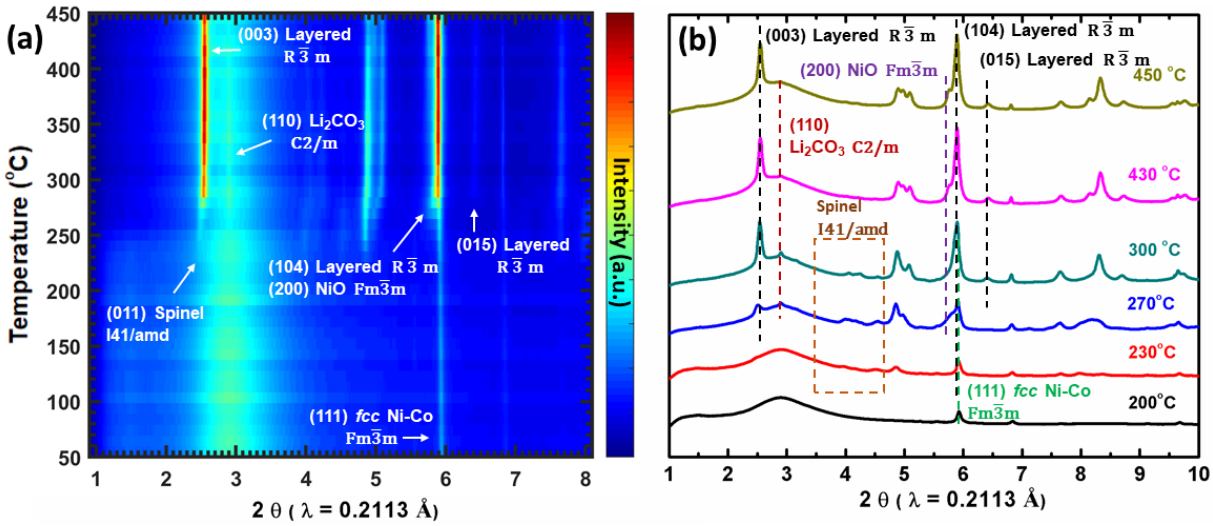

Figure 3.20: *In-situ* synchrotron XRD of the precipitate during heating (a) and the representative patterns (b) up to 450 °C.

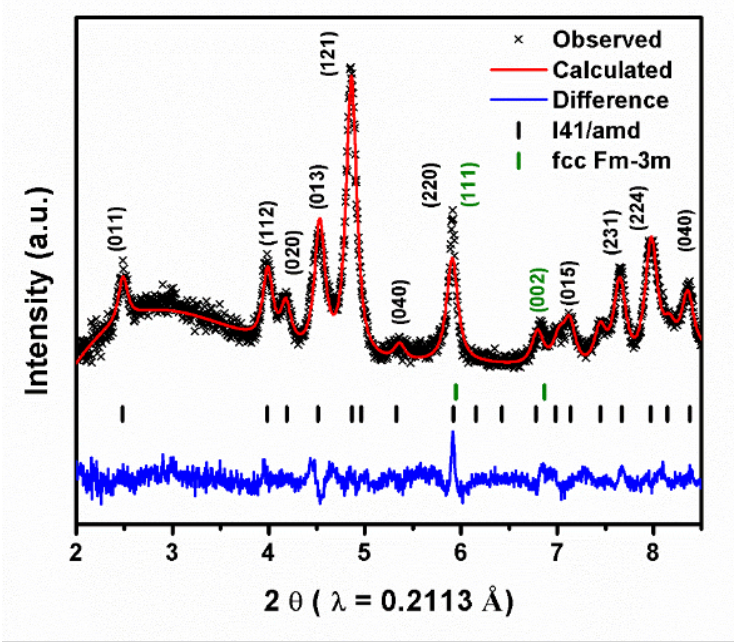

Figure 3.21: Le Bail refinement of the (230 °C – 220 °C) subtracted pattern.

lattice parameters $a = 5.798(1)$ and $c = 9.038(3)$ Å. Comparison of these lattice parameters with literature suggests that the spinel phase features a mixed metal composition, such as in $Co_xMn_{3-x}O_4$, rather than the pure-phase Mn_3O_4 analogue.[109] This observation further

suggests the presence of Co in the amorphous Mn-rich region. The spinel phase remains present and acts as an intermediate in the formation of the structurally-related layered phase ($R\bar{3}m$) up to 430 °C. Formation of the layered phase, albeit disordered, is visible from the growth of the (015) peak growing past 270 °C. The reaction of the spinel phase is consistent with the previous temperature dependence oxidation study of Mn- and Co-species.[109–112] Several studies have reported phase transitions from metallic Co nanoparticles to Co_3O_4 and Mn-glycolate to Mn_3O_4 at a similar temperature range. Also, around 270 °C, a noticeable decrease of the diffuse scattering intensity ($2\theta = 1$–$2°$) is observed, likely due to the decomposition of organic species from the sample and crystallization of the Li- and Mn-species. This coincides with the appearance of another transient peak when amorphous Li-species crystallize to Li_2CO_3 ($C2/m$) as indicated by the (110) reflection.[113,114] We expect that in this temperature range, organic species decompose and release Li that react to form Li_2CO_3. At the same time, the metallic alloy grows, as indicated by increase in peak intensity, and then starts to oxidize. Starting from 250 °C, the apparent asymmetry of the (111) reflection of fcc Ni-Co alloy is due to the growth of the (200) reflection of a cubic phase ($Fm\bar{3}m$), likely NiO and/or CoO. Due to the similar electron-density in Ni and Co and the characteristic peak broadness, it is impossible to distinguish between the two. However, as observed in the previous *in situ* studies, we expect that, once formed, CoO would be short-lived and quickly oxidized again to spinel Co_3O_4 phase.[112,115] In addition, the lattice parameter more closely matches with NiO, therefore, it is more likely that the peaks correspond to NiO.

After 420 °C, (110) reflection from Li_2CO_3 also disappears, leaving only NiO and layered NMC structure. In the typical synthesis condition, the material is dwelled at 450 °C for 12 hours and then cooled back to room temperature to be thoroughly mixed before starting the higher temperature heat-treatment. NiO rocksalt phase still constitute 9.6(4)% of 450 °C annealed sample, therefore, the second heat-treatment at higher temperature is

performed to ensure complete phase transformation to the desired layered NMC.

For the data collected during the second annealing step, Rietveld refinement was employed to diffraction patterns to extract the phase composition and the unit cell parameters as a function of temperature (Table 3.6). As shown in Figure 3.22, the refined cell parameters for both NiO and layered NMC phase mostly follow a linear evolution as a function of annealing temperature. Non-linearity of increase in lattice parameters is observed from 561 °C to 764 °C which is associated with the material transition from two-phase (NiO and layered oxide) to just a single phase of layered oxide. No new intermediate phase was observed during the second annealing step. As mentioned above, the second annealing process starts with 9.6(4)% NiO and 90(2)% of layered NMC. As the temperature increases beyond the first annealing process, NiO is continuously incorporated into layered NMC and becomes no longer visible in the pattern collected at 764 °C. At the same time, significant narrowing of the peaks and increase in intensity are observed, which can be correlated to a process of crystallite growth. Even after a single phase of layered NMC is achieved, temperature was further increased up to 900 °C and then cooled down to room temperature to reduce the percentage of cation mixing down to 7.38%.

Finally, our study was complemented with *ex situ* STEM/EELS (Figure 3.14) and soft XAS (Figure 3.19) studies. As discussed earlier, prior to heat treatment, the precipitate is composed of Ni-Co alloy nanoparticles wrapped by a Mn- and Li-embedded organic matrix. After the low-temperature heat-treatment at 450 °C, HAADF-STEM images show that the crystal size increased from about 5 nm to about 20 nm. Amorphous organic species were no longer observed for the sample. All the nanoparticles are crystalline and well-dispersed without any agglomeration. Interestingly, EELS elemental mapping results show that another core/shell-like feature emerged within the particle. As shown, the transition metals are completely oxidized with uniform distribution of oxygen around the particle. However, the transition metals still show obvious chemical segregation with Ni- and Co-rich

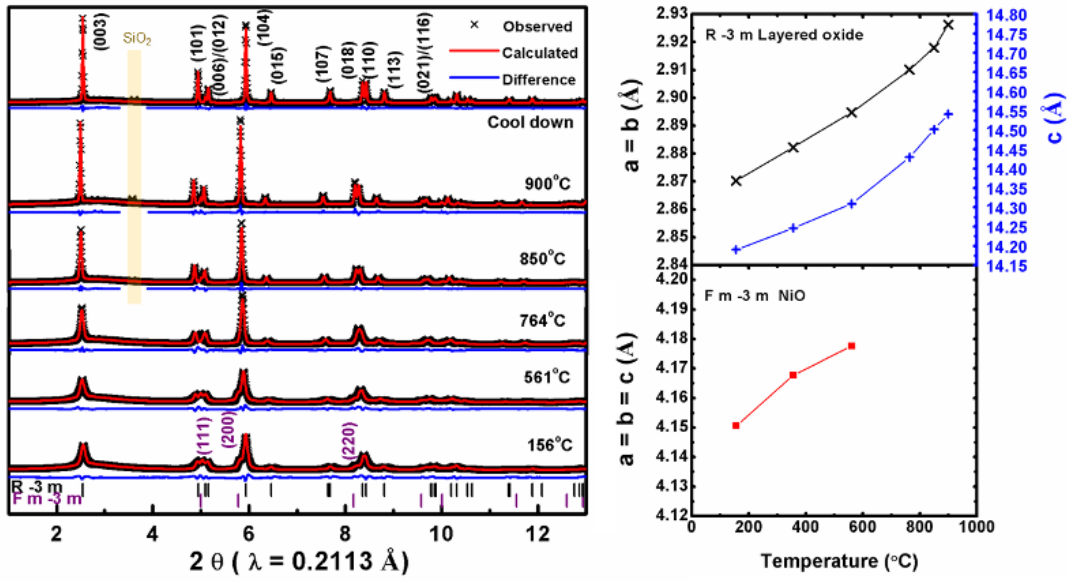

Figure 3.22: Rietveld refinement of high-temperature heat-treatment process.

oxide layer overgrown on a Mn-rich core. We can correlate the elemental segregation of Ni, Co, and Mn with the reaction sequence of the low-temperature heat treatment condition. Mn can form nanocrystals first, due to its proximity to Li in the precipitate form and low reaction temperature. Subsequently, Co from either the Ni-Co alloy and/or organic matrix forms CoO, which quickly transforms into an intermediate spinel phase we observe in XRD. The oxidation state of Co in the spinel would be an approximately +2.7, but further oxidation would shift to +3 as observed in the layered oxide phase. Lastly, the NiO formed from Ni-Co alloy is stable for wide range of temperature, therefore, it persists until the end of the 12-hour 450 °C heat treatment. Moreover, Ni and Co also tends to form a "shell" during the oxidation due to Kirkendall effect.[112,116]

After the second heat-treatment, the size of the particles grows to 138 nm but are still well-dispersed without any agglomeration. STEM/EELS show that all the TM and O are now distributed evenly throughout the sample. Soft XAS results are also in agreement with XRD results. The oxidation states of TM after the first and the second heat treatment

were both confirmed to be +2 for Ni, +3 for Co, and +4 for Mn.[117] Although the 450 °C heat treated sample is still in mixed phase with NiO and the layered NMC, the oxidation state for Ni remains the same for both phases.

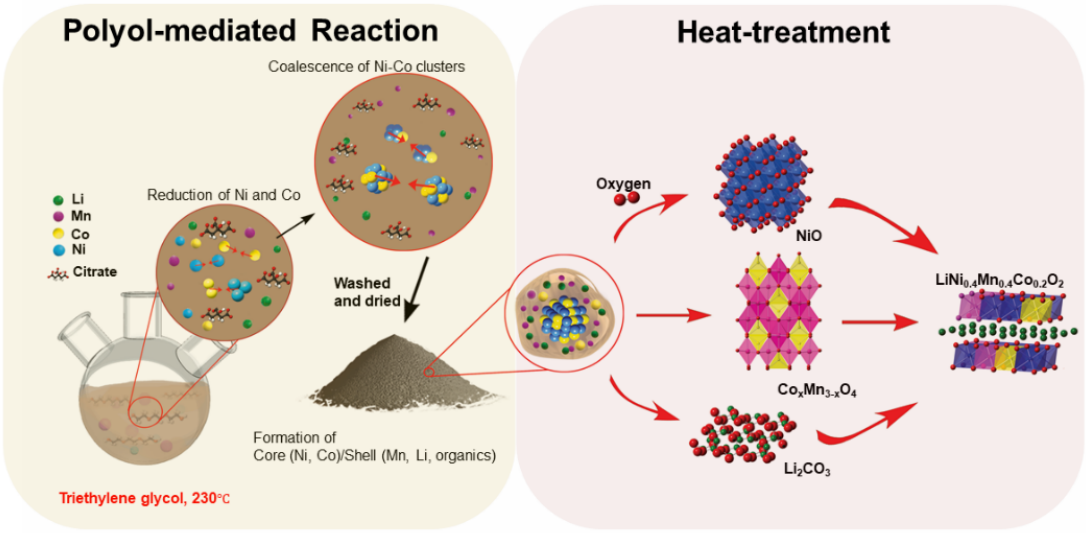

Figure 3.23: Schematic of the polyol reaction and post heat treatment for layered NMC synthesis.

In summary, the preceding discussion lead us to propose more detailed reaction schematics as shown in Figure 3.23. After all the metal ions are completely dissolved in the polyol solution, Ni^{2+} and Co^{2+}-ions get reduced and coalesce as Ni-Co alloy nanoparticles. In the meantime, Li^{+} and Mn^{2+} -ions bond with organic ligands and surrounds Ni-Co alloy in a core/shell-type structure. Then, during the following heat treatment, we observed appearance of the intermediate phases, such as spinel $Co_xMn_{3-x}O_4$ or Li_2CO_3, and transformation to layered oxide phase. On the other hand, the presence of NiO persists through a much larger temperature range and does not fully react until towards the end of the high-temperature treatment. The second heat treatment also results in a decrease of Li/Ni cation mixing and an increase in crystallite size. Similarly, we expect that, during the polyol synthesis of spinel LNMO, Ni^{2+} is reduced Ni^{0} nanometals, while Mn^{2+} -ions precipitate out with organic ligands in amorphous state. As a result, although no crystalline

phase in the precipitate is detected due to the low concentration of Ni compared to Mn, 450 °C heat-treated sample is comprised of NiO and spinel phase (Figure 3.24). Additional high-temperature heat-treatment is needed to transform NiO into a single spinel phase.

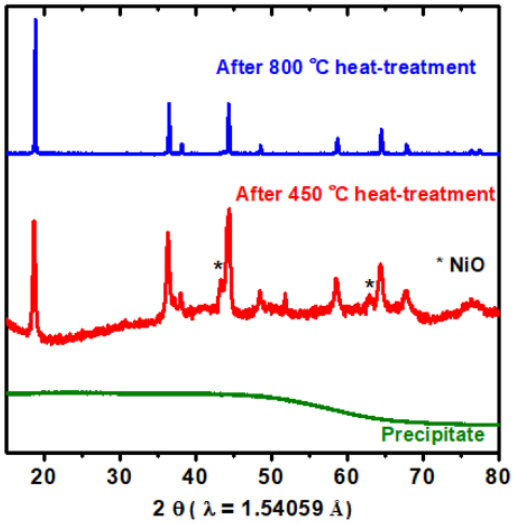

Figure 3.24: Powder XRD pattern collected for spinel LNMO after polyol-synthesis.

3.4 Conclusion

A novel polyol method has been developed to synthesize three cathode materials with different crystal structures. Each product presents uniform elemental and size distribution and exhibited competitive electrochemical performances due to controlled morphology and structural stability. With a dispersive particle morphology, polyol-synthesized cathode materials can also be applied to solid state batteries by providing more intimate contact between solid electrolyte and electrode material. We believe that this method provides a valuable platform for evaluating high-performance, nano-dispersed cathode materials for LIBs. Furthermore, the detailed reaction mechanism has been studied to understand the reaction mechanism underlying each step during the synthesis. Empowered with this knowledge, this novel synthetic method can be employed to develop a wider range of other

stable and low-cost intercalation compounds.

Chapter 3, in full, is a reprint of material, as it appears in: H. Chung; A. Grenier; R. Huang; X. Wang; Z. Lebens-Higgins; J. Doux; S. Sallis; C. Song; P. Ercius; K.W. Chapman; L.F.J. Piper; H. Cho; M. Zhang; Y.S. Meng, "Comprehensive study of a versatile polyol synthesis approach for cathode materials for Li-ion batteries," *Nano Research*, 12, 2238-2249 (2019). The author was the primary investigator and author of this paper. All the experiment parts were performed by the author except sXAS, sXRD, and sol-gel LNMO electrochemical testing.

Table 3.1: Lattice parameters, atomic positions, and site occupancies results from Rietveld refinement of polyol-synthesized (a) layered $LiNi_{0.4}Mn_{0.4}Co_{0.2}O_2$, (b) spinel $LiNi_{0.5}Mn_{1.5}O_4$, and (c) olivine $LiCoPO_4$.

(a)

Atom	Site	X	Y	Z	Occ.
Li	3b	0	0	0.5	0.935(4)
Ni	3b	0	0	0.5	0.065(4)
Li	3a	0	0	0	0.065(4)
Ni	3a	0	0	0	0.335(4)
Co	3a	0	0	0	0.200
Mn	3a	0	0	0	0.400
O	6c	0	0	0.2562(6)	2.000

$a = b = 2.8679(8)$ Å, $c = 14.227(4)$ Å, $\alpha = \beta = 90°$, $\gamma = 120°$
$R\bar{3}m$, $R_{wp} = 1.82, R_B = 10.95$

(b)

Atom	Site	X	Y	Z	Occ.
Li	8b	0.37500	0.37500	0.37500	0.982(4)
Ni	8b	0.37500	0.37500	0.37500	0.018(4)
Li	16c	0.00000	0.00000	0.00000	0.018(4)
Ni	16c	0.00000	0.00000	0.00000	0.482(4)
Mn	16c	0.00000	0.00000	0.00000	1.50000
O	32e	0.2368(3)	0.2368(3)	0.2368(3)	4.00000

$a = b = c = 8.1753(4)$ Å, $\alpha = \beta = \gamma = 90°$
$Fd\bar{3}m$, $R_{wp} = 2.55, R_B = 4.76$

(c)

Atom	Site	X	Y	Z	Occ.
Li	4a	0.00000	0.00000	0.00000	1.00000
Co	4c	0.22204	0.25000	0.52248	1.00000
P	4c	0.40814	0.35000	0.08795	1.00000
O	4c	0.39567	0.25000	0.77290	1.00000
O	4c	0.05556	0.25000	0.28889	1.00000
O	8d	0.33979	0.04121	0.21932	2.00000

$a = 10.194(11)$ Å, $b = 5.9189(6)$ Å, $c = 4.6984(5)$ Å, $\alpha = \beta = \gamma = 90°$
$Pnma$, $R_{wp} = 7.31, R_B = 10.99$

Table 3.2: ICP-AES result of polyol-synthesized cathodes.

Material	**TM ratio**	**Li:TM**
$LiNi_{0.4}Mn0.4Co_{0.2}O_2$	Ni:Mn:Co = 0.404:0.402:0.193	1.012:1
$LiNi_{0.5}Mn_{1.5}O_4$	Ni:Mn = 0.246:0.752	0.975:1
$LiCoPO_4$	-	1.007:1

Table 3.3: First charge and discharge capacity of polyol-synthesized cathodes.

	Charge capacity (mAh/g)	Discharge capacity (mAh/g)	Coulombic Efficiency
NMC	158	140	88.6%
LNMO	137	125	91.2%
LCP	137	108	78.5%

Table 3.4: Rate capability as published in previous studies.

Reference	**Voltage range**	**Rate capability**	**Cycling retention**
NMC442 [83]	$2.0-4.4$	70 (1000mA/g)	90% after 50 cycles with 20mA/g
NMC442 with SWCNT [84]	$2.5-4.5$	130 (800 mA/g) 120 (1600 mA/g)	91% after 500 cycles at 1600 mA/g
NMC442 [80]	$2.5-4.4$	95 (60mA/g) 10 (1800mA/g)	-
NMC442 [85]	$2.5-4.6$	With CMC, 78.4 (10C) With PVDF, 70.5 (10C)	With CMC, 111.8% With PVDF, 79.4%
This work	$2.5-4.3$	101 (1000mA/g) 82 (2000mA/g)	87% after 50 cycles at 20-2000mA/g

Table 3.5: Lattice parameters for fcc Ni and Co metal as published in previous studies

	a = b = c (Å)
fcc Ni [98]	3.510(4)
fcc Ni [99]	3.524
fcc Ni [100]	3.5236
fcc Ni [98]	3.5276(10)
fcc $Ni_{0.7}$ $Co_{0.3}$ [100]	3.5295
fcc Co [99]	3.5441
fcc Co [101]	3.5442

	a = b (Å)	c (Å)
hcp Co [102]	2.520(3)	4.074(9)
hcp Co [103]	2.5054	4.0893
hcp Co [104]	2.506(8)	4.071(1)

Table 3.6: Structural parameters obtained for the one and two-phase PDF refinements of the polyol-synthetized NMC precipitate in the intermediate range (15 – 40 Å).

	Single phase	Two phase refinement	
	fcc	fcc	hcp
Lattice parameters (Å)	a = 3.546(5)	a = 3.547(5)	a = 2.66(3), c = 4.36(8)
Phase fraction (%)	100	65(27)	35(27)
spdiameter (Å)	69(45)	72(23)	84(120)
Ni/Co ADP (Å^2)	0.009(5)	0.008(3)	0.013(17)
R_w	0.356	0.292	

Table 3.7: Structural parameters and composition of layered oxide and NiO rocksalt for high-temperature treatment. n represents Li/Ni cation mixing represented by $[Li_{1-n}Ni_n]^{3b}[Ni_{0.4-n}Li_nMn_{0.4}Co_{0.2}]^{3a}[O_2]^{6c}$.

Layered NMC, R−3 m, $\alpha = \beta = 90°$, $\gamma = 120°$

Temperature °C	Composition (%)	a = b (Å)	c (Å)	O z pos.	n Ni in Li layer
156	90(2)	2.8703(3)	14.190(3)	0.2579(10)	-
356	91(1)	2.8823(3)	14.246(3)	0.2586(10)	-
561	92(1)	2.8948(3)	14.309(3)	0.2586(4)	-
764	100	2.9101(16)	14.430(15)	0.2589(3)	15.9(3)
850	100	2.9180(8)	14.502(6)	0.2584(19)	13.0(5)
900	100	2.9263(6)	14.541(5)	0.2577(2)	13.2(2)
20 (cool down)	100	2.8734(4)	14.262(3)	0.2581(17)	7.38(10)

NiO, F m −3 m, $\alpha = \beta = \gamma = 90°$

Temperature °C	Composition (%)	a=b=c
156	9.6(4)	4.150(4)
356	8.7(4)	4.167(4)
561	7.8(4)	4.178(4)

Chapter 4

Insights into Twin Boundary Defect and Mitigation of Anisotropy Change in Classical Layered Oxide Material for Li-ion batteries

The classical layered oxides $LiNi_xMn_yCo_{1-x-y}O_2$ are promising high energy density cathodes in Li-ion battery, but repeated anisotropic volume changes during lithium extraction/insertion make them intrinsically vulnerable to intergranular and intragranular fractures that leads to capacity decay. Here, we synthesized nano sized $LiNi_{0.4}Mn_{0.4}Co_{0.4}O_2$ (nNMC) cathode materials with highly coherent twin boundaries that may alleviate such degradation. High resolution scanning transmission electron microscopy images show that twin boundaries in nNMC are preferentially aligned in radial direction, propagating from center to surface of the particles. Increased cation disordering is observed along twin boundary and leads to formation of a single layer of rock salt-like phase, which may act an electrochemically inactive framework that mitigates volume changes during cycling. Using

operando XRD, reduced change of the c-lattice parameter and the degree of anisotropy were confirmed. As a result, despite larger surface area that promotes parasitic reaction with electrolyte, nNMC shows enhanced electrochemical performance compared to the micro-sized reference material with the identical composition. While severe pulverization was observed for the reference material after 100 cycles, no change in morphology was observed between pristine and 100-cycled nNMC. Analysis on twin enriched nNMC sheds light on a novel approach of considering twin boundary defect in the design of stable intercalation compounds.

4.1 Introduction

Rechargeable Li-ion batteries (LIB) have become indispensable part of our daily lives as they became the most widely used energy storage devices for portable electronics and electric vehicles. With increasing market demand, intensive research efforts are still ongoing to further improve the energy density, cost, and safety of LIB. Since cathode materials typically have only half of the energy density as the partner anode materials and twice the cost, its advancement is critical for a major breakthrough of the current LIB technology.

In search of the best cathode material, early work focused on discovering novel materials and how their crystal structures and chemical compositions influence overall battery performances. This has led to the discoveries of widely commercialized cathode materials, such as $LiCoO_2$, $LiNi_xMn_yCo_{1-x-y}O_2$, $LiNi_{0.80}Co_{0.15}Al_{0.05}O_2$, and $LiFePO_4$ discovered mainly in the 1970s and 1980s.[10] Then, tremendous progress has been made thanks to high-accuracy characterization tools for nanotechnology, giving us deeper insights into the materials. More studies realized the significant influence of nanoscale interface and defect on the performance of batteries. Thus, the defect engineering was adopted as

material design strategies to tailor these properties to our advantages.[118,119]

Defects or disorders in crystalline materials are inherent to the equilibrium state and cannot be completely avoided due to the second law of thermodynamics. The defects such as cation disordering in cathode materials have traditionally been considered as 'mistakes' in the perfect structure, leading poor battery performance. In recent studies, these defects was exploited to modify materials' transport and surface properties, and electronic structure and to circumvent long standing shortcomings of the parent materials.[120] Oxygen vacancy defects introduced in $Li[Li_{0.144}Ni_{0.136}Co_{0.136}Mn_{0.544}]O_2$ cathode material provided favorable ionic diffusion environment in the bulk and significantly suppressed irreversible oxygen gas release.[121] Antisite defects enhance the rate capability of $LiFePO_4$ by increasing the active surface area for Li intercalation.[122,123]

Herein, we report the potential role of highly coherent twin boundaries (TBs) defects observed in the classical layered oxide $LiNi_{0.4}Mn_{0.4}Co_{0.2}O_2$ nanoparticles (nNMC) produced by polyol synthesis method. A TB is a plane of lattice points where the crystals on either side of the interface possess mirror symmetry. The formation of atomically sharp TBs has been observed in several metals and ceramics[124] but rarely reported in battery cathode materials.[12] Using scanning transmission electron microscopy (STEM), we have analyzed the crystallographic structure at TBs. Also, influence of the TBs on the formation of facets which the surface of the nNMC particles are terminated by were investigated. Despite the high concentration of defects and larger cathode-electrolyte-interphase observed, nNMC still show enhanced electrochemical performance with higher long-term cycling retention compared to the reference $LiNi_{0.4}Mn_{0.4}Co_{0.2}O_2$ (μNMC). The structure evolutions observed with operando XRD show that nNMC experience mitigated c-lattice expansion and contraction during charge and discharge process compared to μNMC. It was proposed that the formation of electrochemically inactive rock-salt like phase along TBs worked as a framework to mitigate volume expansion during cycling. We believe that our results can

propose a novel approach of considering TB defect in the design of stable intercalation compounds with low internal stress.

4.2 Experimental Methods

4.2.1 Electrochemistry

Synthesis of $LiNi_{0.4}Mn_{0.4}Co_{0.2}O_2$ nanoparticles has been followed by the previous study.[125] Using 80 ml of tetraethylene glycol (Aldrich, 80 ml) solvent, all the transition metal acetates – $(NiCH_3COO)_2{\cdot}4H_2O$ (Acros, 0.012 mol), $(MnCH_3COO)_2 \cdot 4H_2O$ (Acros, 0.012 mol), and $(CoCH_3COO)_2{\cdot}4H_2O$ (0.006 mol)– and $LiOH{\cdot}H_2O$ (Sigma-Aldrich, 0.0345 mol) were mixed with citric acid (Sigma-Aldrich). All the salt precursors dissolved when the mixture was heated to 230 °C for 3 h in a round-bottom flask connected to a reflux. Once the mixture cooled down to room temperature, the precipitate was washed with ethanol, dried overnight, and heat-treated at 450 °C for 12 h in air. The powder was then ground with agate mortar and pestle, pelletized, and then went through a second heat-treatment at 850 °C for 5 h in air. Commercial $LiNi_{0.4}Mn_{0.4}Co_{0.2}O_2$ powder was heated to 500 °C in air to remove proton-containing surface species.[126] All the $LiNi_{0.4}Mn_{0.4}Co_{0.2}O_2$ powders were stored in an Ar-filled glovebox (MBraun, < 1 ppm H_2O).

Table 4.1 summarizes the coin cell configuration used for our study. For both TEM and FIB characterization, all cells were cycled with the current rate of C/10. For long-term electrochemical results, C/10 was used for the first two formation cycles, while a current rate of 1 C or C/3 was applied for the rest of the cycles. All three characterizations used the voltage range of $2.5 - 4.7$ V with the theoretical capacity defined as $200\,\mathrm{mA\,h\,g^{-1}}$. Arbin BT2000 cycler (Arbin instrument, USA) was employed to carry out all the galvanostatic cycling tests.

Table 4.1: Coin cell testing specifications.

Half-cell Configuration	
Active material	$LiNi_{0.4}Mn_{0.4}Co_{0.2}O_2$ - 80%
Conductive agent	SPC65 - 10%
Binder	HSV900 - 10%
Counter electrode	Li metal chip (Thickness: 1 mm, diameter: 15.4 mm)
Separators	Celgard 2325
Electrolyte type	1M $LiPF_6$ in EC:DMC = 3:7 vol%
Electrolyte amount	55 µl
Cell type	CR2032
Coin cell setup	0.5 mm thick spacer and one spring at anode side
Voltage range	1.5 - 4.8 V
Test protocols	Rest for 6 h after assembling, then 20 $mA\,g^{-1}$ the rest at 66.7 $mA\,g^{-1}$ (C/3) or 200 $mA\,g^{-1}$ (1C) at room temperature
Active material loading	3.7 - 4.4 $mg\,cm^{-2}$

4.2.2 Material Characterization (FIB, SEM, XPS, ICP)

All high-resolution STEM images were taken using the double aberration-corrected scanning TEM (TEAM 0.5) operated at an acceleration voltage of 300 kV installed at the Molecular Foundry at Lawrence Berkeley National Laboratory. All annular dark-field STEM micrographs were recorded in TEAM 0.5 with a convergence angle of 30 mrad and a probe size of < 1 Å after fine-tuning of the probe corrector at 300 kV. The morphologies of the particles were identified using a Zeiss Sigma 500 or FEI Apreo scanning electron microscope (SEM) with an accelerating voltage of 5 kV. Cross-sectional images of commercial NMC were collected from focused ion beam (FIB) using FEI Scios^{TM} Dual beam^{TM} FIB. The chemical compositions of $LiNi_{0.4}Mn_{0.4}Co_{0.2}O_2$ materials were confirmed by ICP-MS (iCAP RQ, Thermo Fisher Scientific. Table 4.2 shows that both samples are close to their intended ratios with variance in the range of experimental error.

X-ray photoelectron spectroscopy was performed using a Kratos AXIS Supra by Analytica with Al anode source operated at 15 kV. High-resolution spectra were calibrated

using hydrocarbon C 1s peak at 284.5 eV.

4.2.3 Operando XRD

Electrode pellets were prepared by mixing the NMC powders with carbon black (Timcal Super C65), and polytetrafluoroethylene powder (Sigma-Aldrich, 1 µm particle size), in a 7:1:2 weight ratio. Approximately 6 mg of the mixture was pressed in a 3 mm diameter die to form ~ 400 µm thick pellets. The NMC electrode pellets were assembled into modified RATIX electrochemical cells[127] using lithium foil (MTI Corp) as a counter electrode, and two layers of glass fiber (Whatman GF/B). A picture of the modified RATIX cell setup is shown in Figure 4.1. The electrolyte used was 1 M $LiPF_6$ dissolved in a mixture of ethylene carbonate and dimethyl carbonate (1:1 volume ratio, Sigma-Aldrich). All preparations were carried out in a glovebox filled with argon containing less than 1 ppm O_2 and H_2O. Electrochemical measurements were carried out at a rate of 18.58 $mA\,g^{-1}$ of NMC between 4.8 and 2.7 V, with a 2 h potentiostatic hold at each voltage limit followed by a 2-hour rest period (Bio-logic BCS-810).

Operando synchrotron X-ray diffraction data were recorded during electrochemical measurements using high-energy X-rays ($\lambda = 0.1668$ Å) provided by beamline 28-ID-1 at the National Synchrotron Light Source II (NSLS-II) at Brookhaven National Laboratory. Each diffraction image was obtained from a 30 s summed exposure recorded in transmission geometry as the electrode was scanned horizontally in transverse mode,[128] gauging the whole diameter of the electrode. XRD patterns were obtained from integration of the

Table 4.2: ICP-MS result of $LiNi_{0.4}Mn_{0.4}Co_{0.2}O_2$ Cathode.

sample	Ni : Mn : Co	Li : (Ni+Mn+Co)
nNMC	0.400 : 0.400 : 0.200	1.008:1
μNMC	0.396 : 0.398 : 0.206	1.034:1

images using the GSAS-II software,[47] and using LaB_6 (NIST SRM 660c) as standard for calibration.

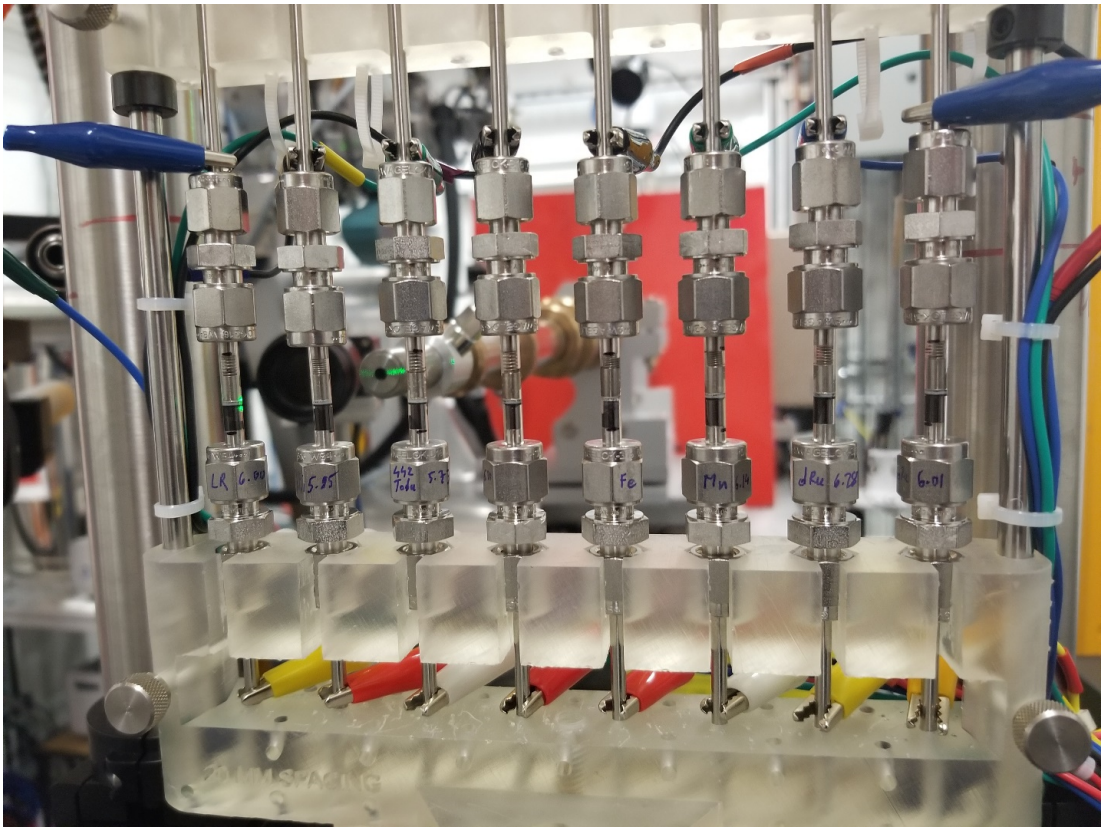

Figure 4.1: RATIX electrochemical cell set up.

4.2.4 XRD Refinements

Rietveld refinements to the XRD data were performed with Topas-Academic V6 using a model based on the $R\bar{3}m$ space group, with TM site (3a) and O site (6c) occupancy based on the nominal composition, and Li site (3b) occupancy based on the electrochemical data. Refined parameters included lattice parameters (a, c), Li-Ni antisite mixing (3a-3b site exchange), O z coordinate, scale factor, isotropic atomic displacement parameters (B_{iso}) for TM and O (fixed to $1\,Å^2$ for Li), and peak profile parameters (5 parameters) as introduced by Stephen in his anisotropic peak broadening model.[129] Background and

additional peaks from the cell inactive components (e.g., from the glass tube container or PTFE additive) were fit using a combination of a 6-coefficient Chebyshev polynomial function and a series of pseudo-Voigt functions. For the sequential Rietveld refinements, the pseudo-Voigt functions' parameters were fixed to values obtained for the 1st XRD pattern.

4.2.5 DFT Calculation

A spin-polarized GGA+U approximation to Density Functional Theory (DFT) was employed, to account for electron correlations in transition metals.[130] Projector augmented-wave method (PAW)[118] pseudopotentials[131] were used as implemented in the Vienna Ab initio Simulation Package (VASP).[132,133] The Perdew–Burke–Ernzerhof exchange correlation and a plane wave representation for the wavefunction with a cut-off energy of 520 eV were used. An effective U values of 3.32 used for Co applying the rotationally invariant approach.[134] The Brillouin zone was sampled with k-point meshes of $15 \times 15 \times 3$, $3 \times 3 \times 1$, $2 \times 3 \times 1$, and $3 \times 5 \times 1$ for the bulk structure, (1-12), (107), and (1-18) surfaces by Gamma packing, respectively. Atomic coordinates and lattice vectors were fully relaxed for each structure. Surface energies, γ, are calculated by the following equation:

$$\gamma = \frac{E_{\text{slab}} - nE_{\text{bulk}}}{2A} \tag{4.1}$$

where the E_{slab} and E_{bulk} and the free energies of the surface structures and bulk structure, respectively, n normalizes the number of formula units, and A is the surface area of a supercell.[135]

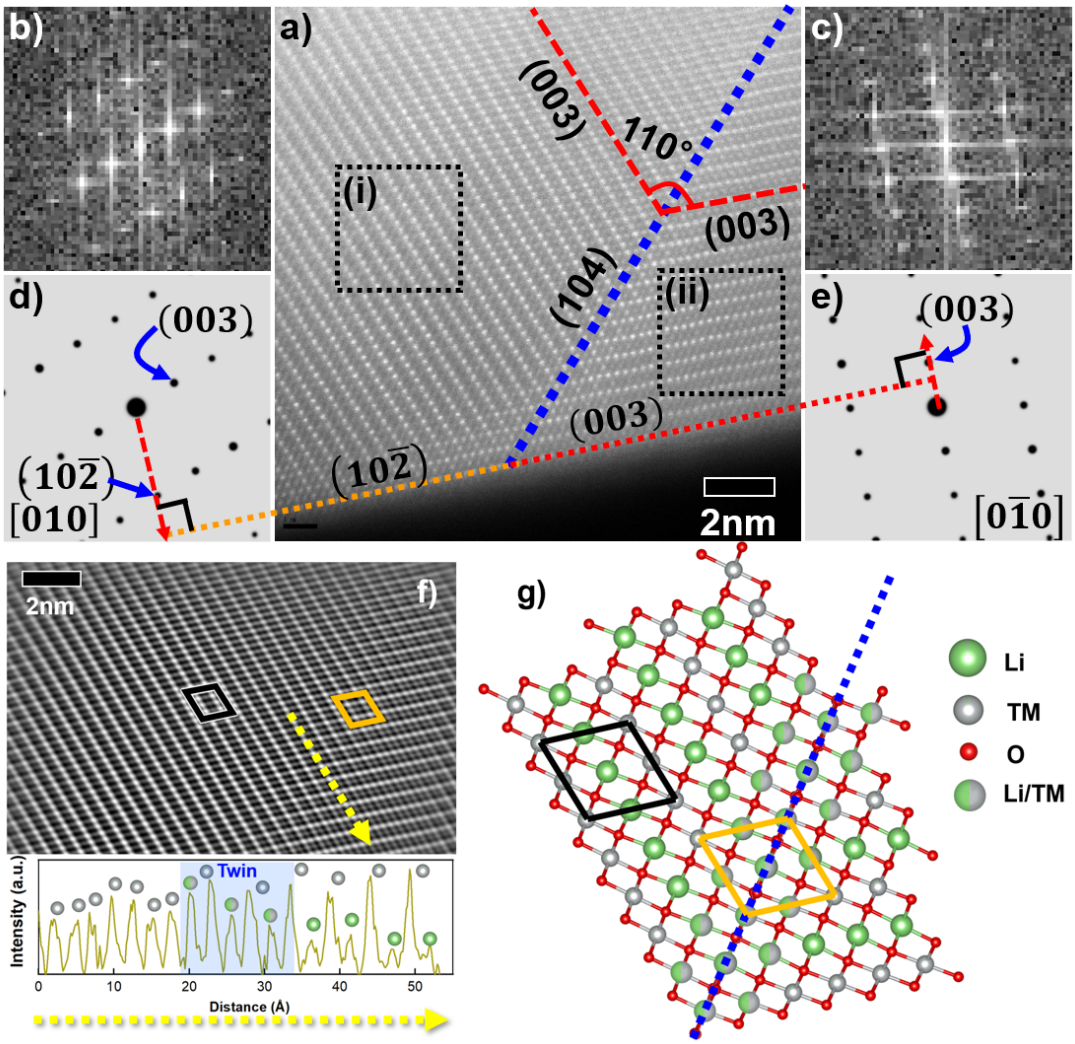

Figure 4.2: a) STEM image of a nNMC particle. The contained angle between two (003) planes (indicated by red dotted line) on two regions divided by the twin boundary (TB, blue dotted line) is 110°. Comparison of Fourier transform patterns from b) region (*i*) and (c) region (*ii*) on (a) and simulated diffraction patterns of $LiCoO_2$ with d) [010] and e) [0$\bar{1}$0] zone axis. f) Fourier filtered image of Figure 1a, which clearly exhibits transition near the TB. g) Atomic structure near the TB as indicated by blue dotted line. Black and orange boxes in (f) and (g) indicate unit cells without and with cation mixing, respectively. Cation mixing is schematically represented as mixed color circle of Li (green) and TM (grey).

4.3 Results and Discussion

4.3.1 Twin boundary defect of pristine nNMC

Twin boundaries formed in radial direction in the polyol synthesized nNMC. Figure 4.2 shows HAADF-STEM image of the nNMC taken along the [010] zone axis. In addition to the well-defined layered structure as seen in the literature,[12] we observe the bonding of two slabs across a (104) plane, forming an atomically sharp boundary. This interphase, as marked by the blue dotted line in Figure 4.2a, was identified as a crystallographic TB with a mirror symmetry in the structure. The TB extends radially from center to surface of the particle with two (003) planes across TB forming 110°. Symmetry and rotation were further confirmed by Fourier transform (FT) images obtained in two areas indicated by (*i*) and (*ii*) on Figure 4.2a. The results were compared to the simulated diffraction patterns of $LiCoO_2$ (LCO) with zone axis of [010] and $[0\bar{1}0]$ since it shares the same space group of $R\bar{3}m$ with $LiNi_{0.4}Mn_{0.4}Co_{0.2}O_2$.[136] The FT images in Figure 4.2b and 4.2c match closely with simulated diffraction patterns in Figure 4.2d and 4.2e, respectively, confirming the complete symmetry observed in the STEM image.

Figure 4.2f represents Fourier-filtered image of Figure 4.2a to more clearly visualize the atomic structure formed along the TB. In this image, the line intensity profile that runs across TB was collected as indicated by yellow arrow. High and low intensity peaks in line profile represents the location of transition metal ions (TM) and Li, respectively, as Li would be invisible due to the low atomic mass in Z-contrast image. As shown, when the line starts on the left side of TB, similar intensity peak is observed in about 2.5 Å increment as it passes along (003) plane. Then approaching to TB, each alternating peak starts losing intensity as more Li starts to occupy the alternating TM location. Such disordering is gradually alleviated after passing TB where Li and TM are now alternatively arranged. Severe cation disordering observed on TB and the sites adjacent to it leads to

phase transition of layered structure to rock-salt like phase as indicated by the unit cells selected as orange box in Figure 4.2f and 4.2g. The rock-salt like phase clearly contrasts in perfect layered structure observed in black box unit cell located away from TB. The formation of TBs in radial direction and the presence of rock-salt like phase along the TB appears general phenomena in the classical layered oxide synthesized by polyol method as shown in Figure 4.3 and 4.4. It is important to note that cation disordering observed

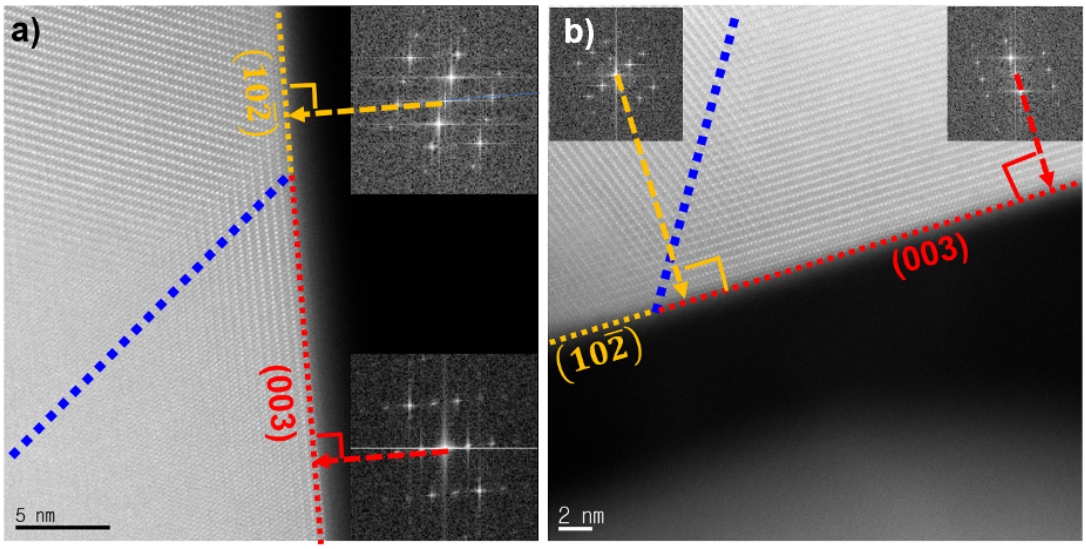

Figure 4.3: Additional images of nNMC with twin boundary.

here contrasts with cation disordered reported in previous studies where cation disordering is typically confined to the surface of cathode particles.[137] Herein, a few atomic layers of rock-salt like phase is aligned radially, propagating from the center to the surface the particle along the TBs.

The surface planes were identified by the reciprocal vectors of (10$\bar{2}$) on Figure 4.2d and (003) on Figure 4.2e indicated by red dotted arrows that are perpendicular to the corresponding planes in real space on (a). By forming TB, it is expected that the facets with high surface energy were replaced by those of low surface energy in order to reduce the total surface energy per particle. All the particles observed with TB in Figure 4.2, 4.3,

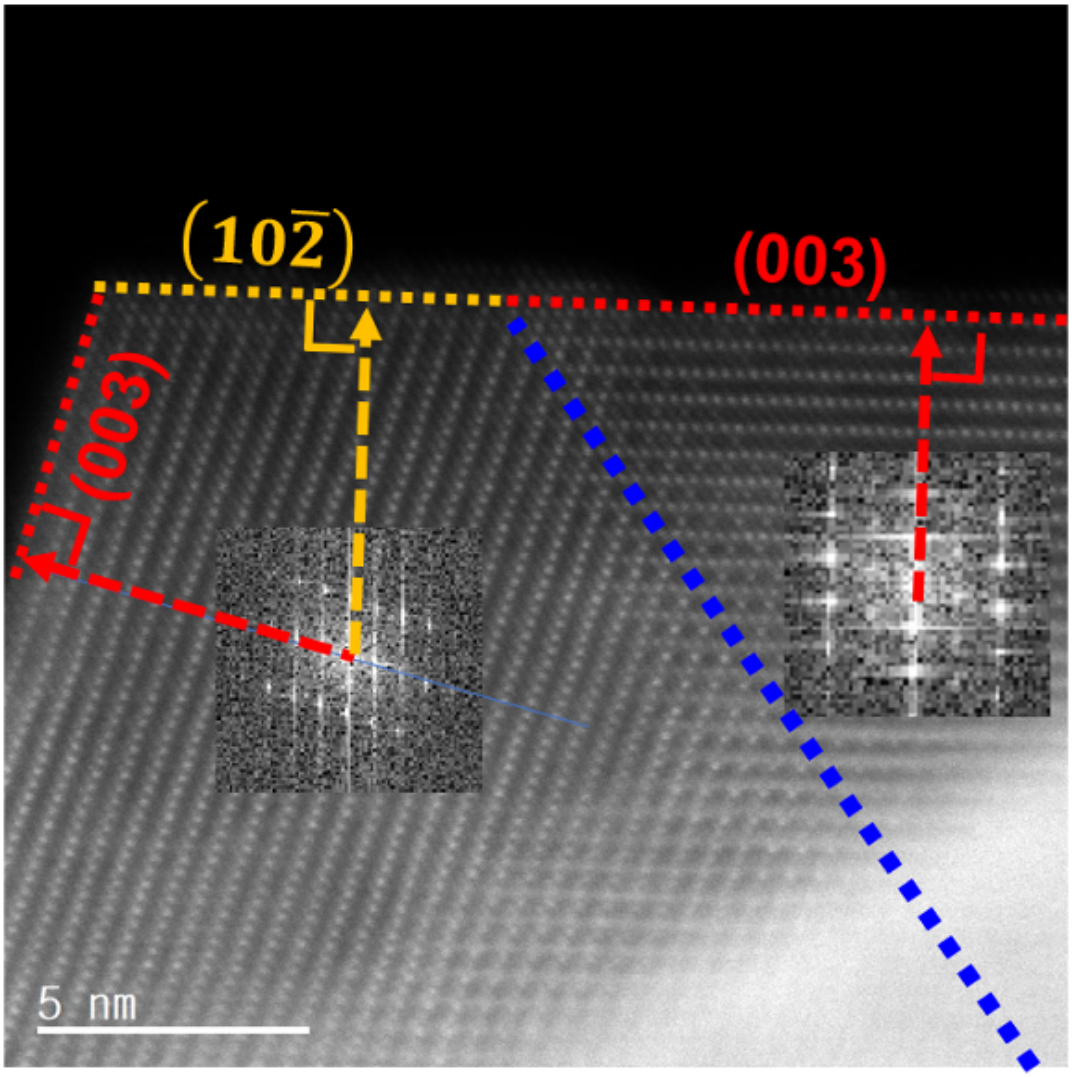

Figure 4.4: Additional images of polyol synthesized $LiNi_{0.33}Mn_{0.34}Co_{0.33}O_2$ with twin boundary.

and 4.4 have the similar terminating surface planes.

The surfaces of nNMC particles without twins were also observed, which contain some facets with high surface energy such as (11-8), (11$\bar{2}$), and (107) as shown in Figure 4.5. In contrast, the facets closed to TBs are terminated by the planes with low surface energy such as (003), (104), and (10$\bar{2}$). According to a previous report, (003), (104), and (10$\bar{2}$) of LCO, whose crystal structure was identical to NMC, have low surface energy

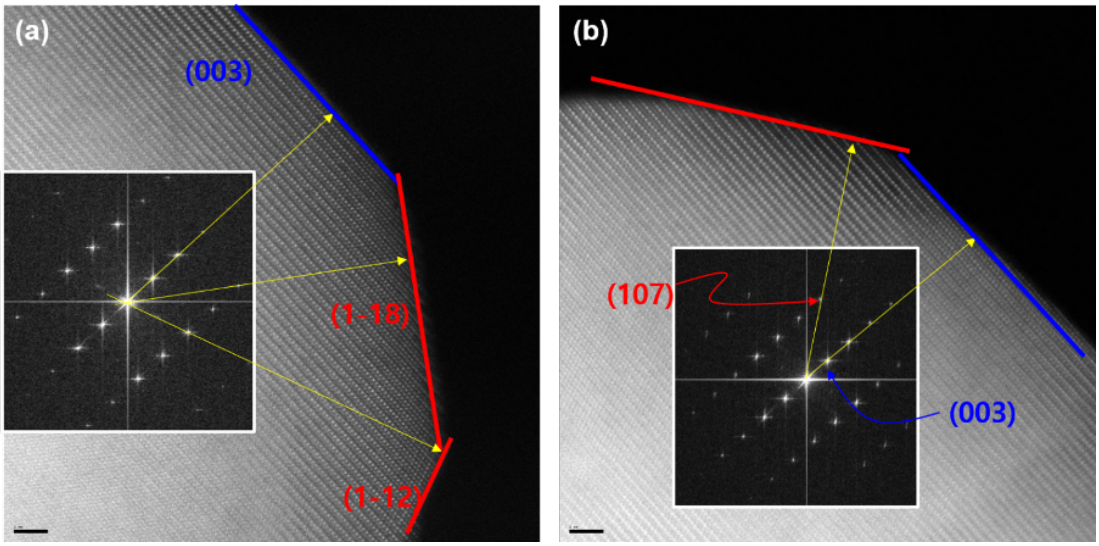

Figure 4.5: Two STEM images of areas without a twin boundary in nNMC particles. The insets show the FFT images of the particles. The FFT patterns confirm that surfaces of the particles were terminated by (a) (003), $(1\bar{1}8)$ and $(1\bar{1}2)$ and (b) (003) and (107) with twin boundary.

around $\sim 1\,\mathrm{J\,m^{-2}}$ compared to other planes such as (110) with $2.241\,\mathrm{J\,m^{-2}}$ and (100) with $2.943\,\mathrm{J\,m^{-2}}$.[138] Similar to other twinned materials,[124] it is expected the TBs primarily forms in order to minimize total surface energy per volume during the synthesis of nNMC. Energy minimization argument is widely studied as the Wulf construction that is the equilibrium shape for large single crystal particles. In nano-crystallites, the studies by Howie and Marks show that TBs leads to the surface with even lower energy than surfaces developed by the Wulf construction.[139–141] These previous studies are consistent with the results in this report.

4.3.2 Electrochemical Characterization

Figure 4.6 shows the electrochemical performance of nNMC tested in half-cell configuration using the voltage range of $2.5 - 4.7\,\mathrm{V}$. The high voltage cutoff was used to evaluate the material stability near the theoretical capacity ($\sim 274\,\mathrm{mA\,g^{-1}}$) when almost all the Li extracted out of the structure. All the results were compared with the reference

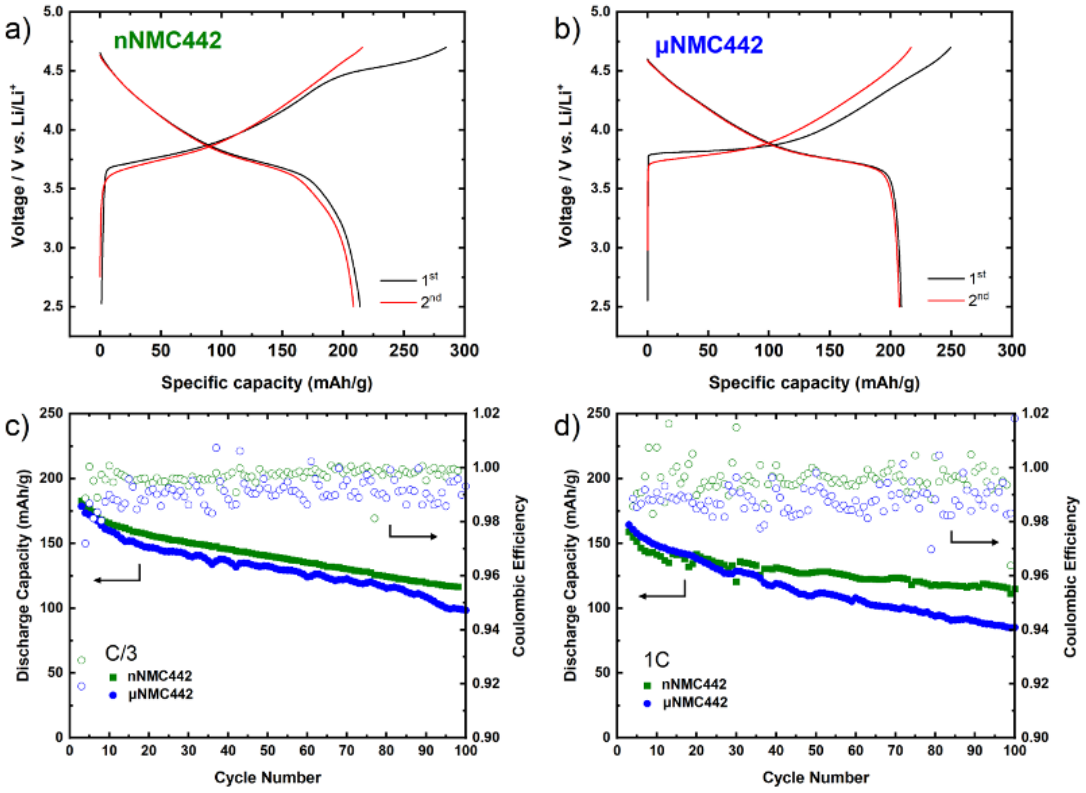

Figure 4.6: Electrochemical performance of nNMC and μNMC. (a, b) Voltage profile of the first and second cycle and (c, d) Cycling performance in the voltage range of $2.5-4.7\,\mathrm{V}$

material obtained commercially (μNMC). As shown, both nNMC and μNMC samples demonstrate the typical behavior of layered oxide materials with high voltage cutoffs: high initial capacity but followed by capacity decay with prolonged cycling. Initially, nNMC has charge capacities of $284\,\mathrm{mA\,g^{-1}}$, compared to $250\,\mathrm{mA\,g^{-1}}$ of μNMC. The large initial charge capacity of nNMC mainly stems from the increased side reactions with electrolyte with its large surface area per volume. Figure 4.7 shows that nNMC has dispersed nanoparticle morphology without agglomeration, while μNMC exist as tightly packed micro-sized aggregates of smaller primary particles. Thus, nNMC has a surface area of $2.83\,\mathrm{m^2\,g^{-1}}$, 5 times more than the μNMC sample ($0.5\,\mathrm{m^2\,g^{-1}}$),[125] where large amounts of cathode-electrolyte-interphase (CEI) can form in the first cycle and contribute to the additional

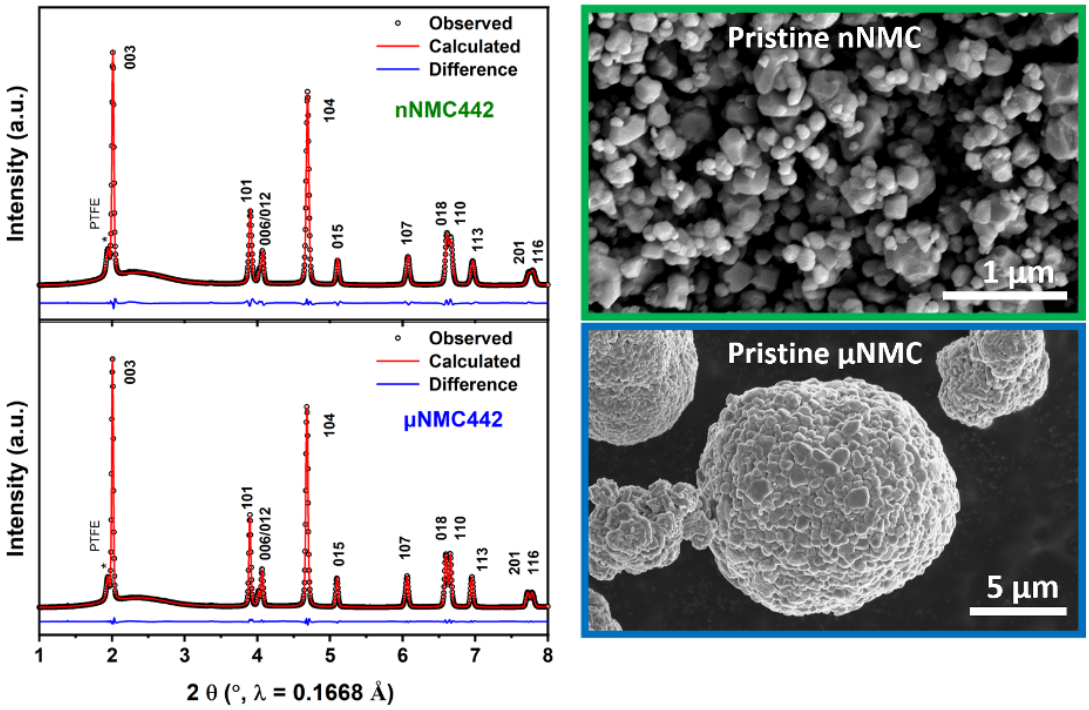

Figure 4.7: Rietveld refinements of high-resolution synchrotron XRD data for uncycled electrode mixture prepared with nNMC (top left) and μNMC (bottom left). Morphology of pristine powder of nNMC (top right) and μNMC (bottom right).

charge capacity. This additional first charge capacity of nNMC is mainly irreversible, and both samples show more similar first discharge capacity of 214 and 209 $\mathrm{mA\,g^{-1}}$. Figure 4.8 shows the comparison of XPS result to confirm that relative amount of CEI as proposed above. The spectra were normalized to lattice O peak to clearly visualize the relative peak intensity between lattice O and surface species. The result also confirms that, although the pristine samples look similar, larger amount of surface species developed for nNMC after the first 10 cycles. However, after both NMCs were repeatedly charged and discharged for long-term, nNMC showed improved capacity retention compared to μNMC. After 100 cycles, nNMC retained the capacity of 116 and 124 $\mathrm{mA\,g^{-1}}$ at C/3 and 1C, compared to 98 and 85 $\mathrm{mA\,g^{-1}}$ for μNMC, respectively. Moreover, CE of nNMC were also higher showing the average efficiency of 99.6% and 99.7% from the 3^{rd} to the 100^{th} cycle for C/3 and 1C rates, respectively. Traditionally, it was reported that high concentrations of defects and

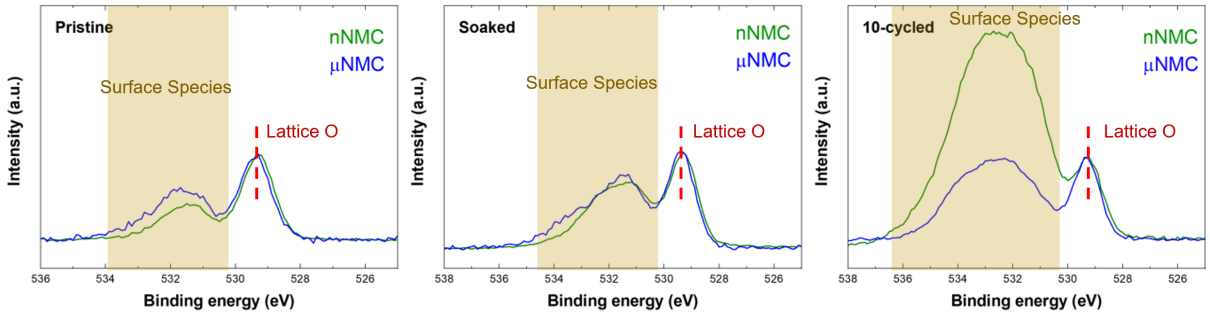

Figure 4.8: XPS result of O 1s core region for pristine, 6 h electrolyte soaked, 10-cycled nNMC and μNMC electrode,

increased side reaction with electrolyte adversely affect the electrochemical performance of the material. However, the enhanced electrochemical performance for nNMC indicates that there is even more critical factor that needs to be considered. This has motivated us to investigate the bulk structural evolution during charge-discharge process with operando XRD.

4.3.3 Operando XRD

Figure 4.7 shows XRD of two samples in an as-assembled state before any current was applied. The result shows that all peaks can be indexed by the α-$NaFeO_2$-type structure with $R\bar{3}m$ space group or by the PTFE binder additive. Table 4.3 presents the results from Rietveld refinement analysis. The results show that the acquired lattice parameters and Li/Ni cation mixing of nNMC shows slightly smaller a and c lattice parameter with 2.86868(4) 2.86868(4) Å and 14.2304(3) Å, compared to 2.87265(2) Å and 14.2692(1) Å, respectively, for μNMC. Slightly larger Li/ Ni mixing of 5.66(8)% for nNMC was also observed compared to 5.10(5)% of μNMC. This correlates well with earlier TEM observations that nNMC shows a rock-salt like phase along the abundant twin boundaries which typically has a smaller lattice parameter than layered oxide.

After the characterization of the initial states, both NMC samples were charged to

Table 4.3: Lattice parameters, degree of Li/Ni cation mixing, and R factors estimated by Rieveld refinement.

sample	nNMC442	μNMC442
a = b (Å)	2.86868(4)	2.87265(2)
c (Å)	14.2304(3)	14.2692(1)
V (Å^3)	101.417(4)	101.975(2)
O z coord.	0.2589(1)	0.25841(6)
Ni-Li exch.	0.0566(8)	0.0510(5)
B_{iso} 3a/TM site (Å^2)	0.22(2)	0.33(1)
B_{iso} 6c/O site (Å^2)	0.34(4)	0.66(2)
R_{wp} (%)	3.470	2.233
R_b (%)	0.293	0.284

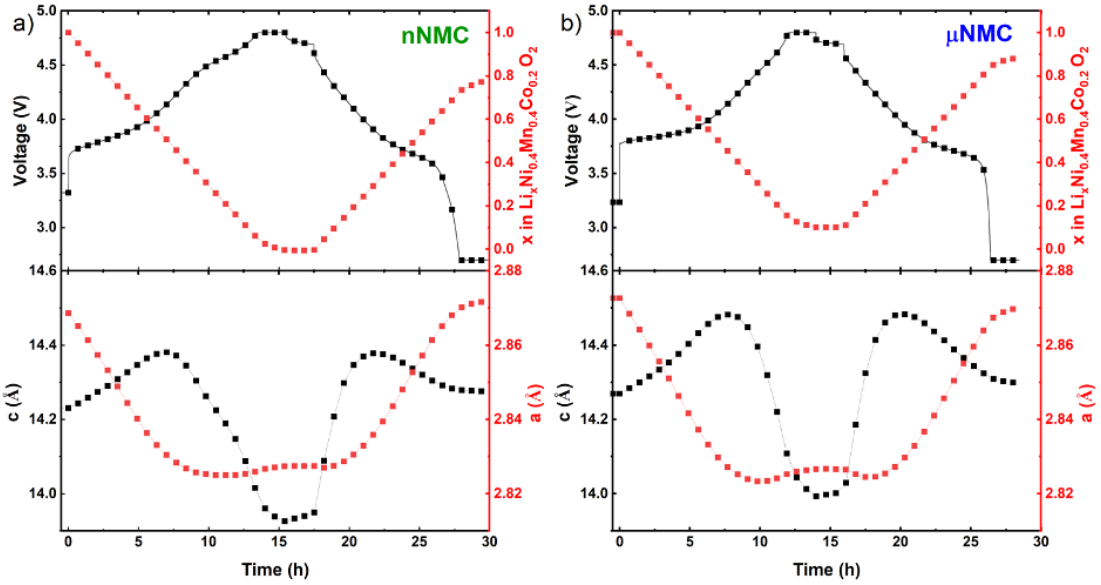

Figure 4.9: Electrochemical charge/discharge voltage profile with corresponding lattice parameters at different states of Li content for nNMC and μNMC.

4.8 V and discharged to 2.7 V, as shown with the voltage profile in Figure 4.9. Figure 4.10a, b represent 2D image plots of the operando XRD patterns corresponding to the 003 and 110 reflections during one charge-discharge cycle. The 003 peak represents lattice changes occurring along the c-direction while 110 represents changes along the a-direction. Consistent with previous studies with other layered oxides, 003 peak shifts to higher angles

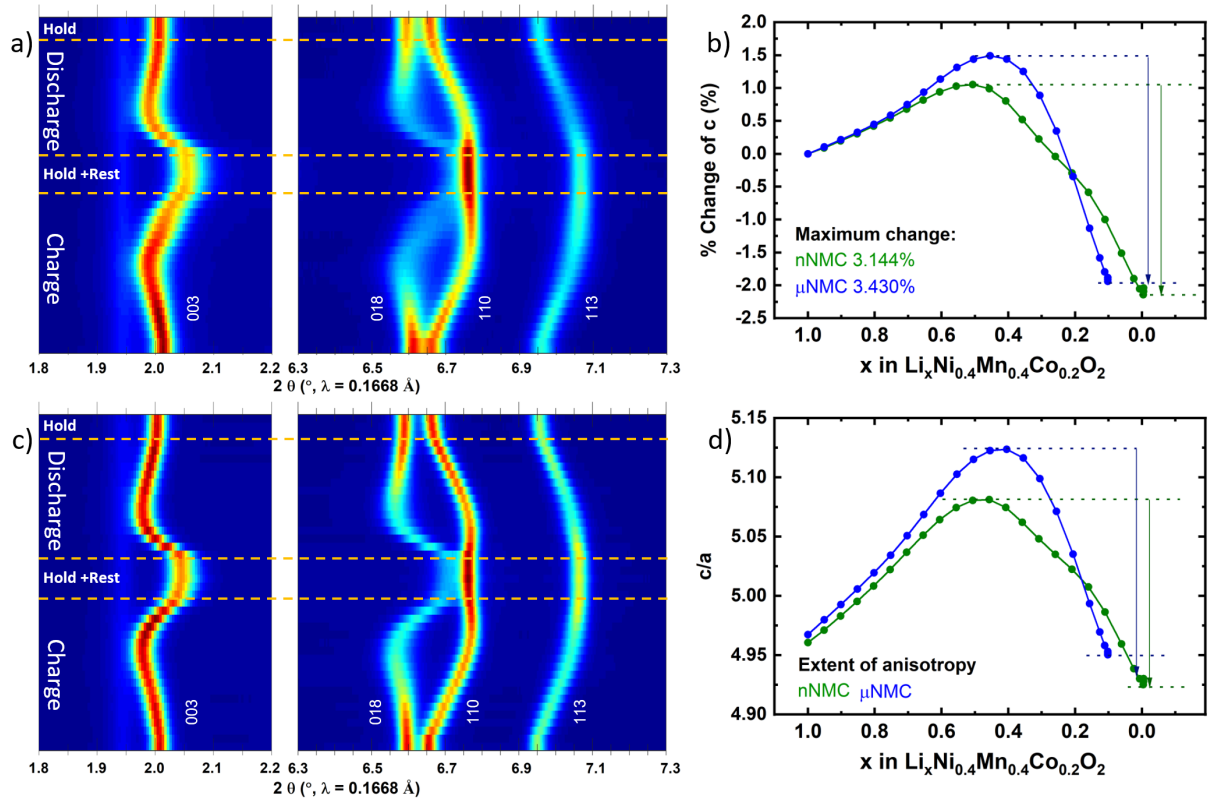

Figure 4.10: Operando X-ray diffraction results of $LiNi_{0.4}Mn_{0.4}Co_{0.2}O_2$: Contour plot of the diffraction peak evolution of (003), (018), and (110) planes during the first cycle of a) nNMC and c) μNMC. Comparison of the corresponding calculated lattice parameters along b) c-axis and d) the c/a ratio, showing the degree of "anisotropy" of the lattice changes as a function of Li content during charge to 4.8 V followed by 2 h hold at 4.8 V and rest for 2 h.

during charge as oxygen atoms in TM layer repulse after Li diffuse out of the structure. Meanwhile, a-lattice contracts at a high state of charge consistent with other the classical layered oxide with low Ni content observed in the literature.[142] Lattice parameters are calculated with LeBail refinement and presented with respect to Li content in Figure 4.10c, d and Figure 4.9.

Interestingly, the result shows that nNMC experienced less c-lattice expansion and contraction during the charge process although both samples show the identical composition as shown in Figure 4.12. Note that the Li content from $x = 0 - 0.2$ has been shifted to lower value due to additional charge capacity observed due to side reaction with electrolyte.

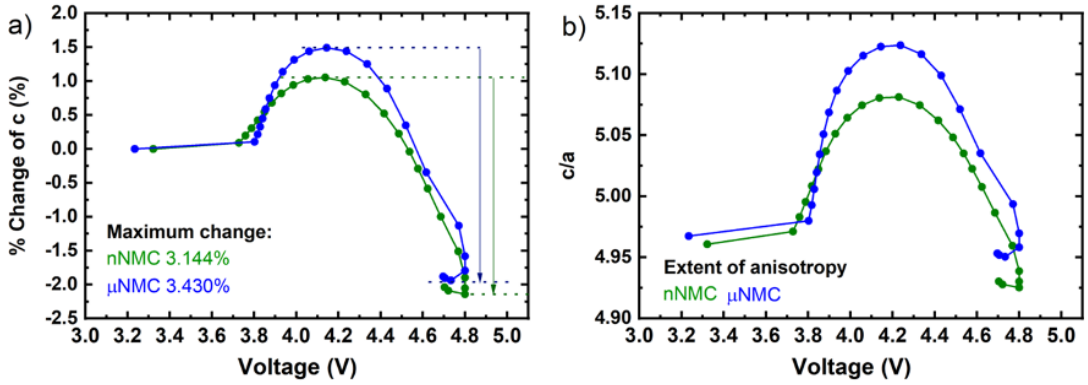

Figure 4.11: Comparison of the corresponding calculated lattice parameters along b) c-axis and d) the c/a ratio, showing the degree of "anisotropy" of the lattice changes as a function of voltage (vs. Li/Li^+) during charge to 4.8 V followed by 2 h hold at 4.8 V and rest for 2 h.

This trend is absent when the calculated parameters are shown with respect to voltage as shown in Figure 4.11.

If we compare the total percentage of c lattice parameter change during cycling, nNMC is 3.144%, which is smaller than 3.430% of μNMC. This leads to also smaller anisotropy changes, which indicates that nNMC is subjected to much less strain in the structure compared to μNMC. Anisotropic changes (expansion in c, contraction in a) in lattice dimensions during Li extraction and insertion have been considered as the major cause of the capacity loss after cycles as it was linked to intergranular and intragranular cracking observed at the boundary between primary particles in micro-sized samples. We expect that the rock-salt like phase formed along the TBs can contribute to the mitigation of c lattice parameter changes observed in nNMC. The rock-salt like phase is known to show negligible volume change because it is electrochemically inactive, thus can act as a framework during the volume expansion and contraction.

Figure 4.12 shows that the cross-section images of μNMC exhibit significant cracking behaviour after 100-cycles in contrast to the pristine material. The microcracks led to more exposed surfaces for parasitic reaction with electrolyte and an increase of electrical

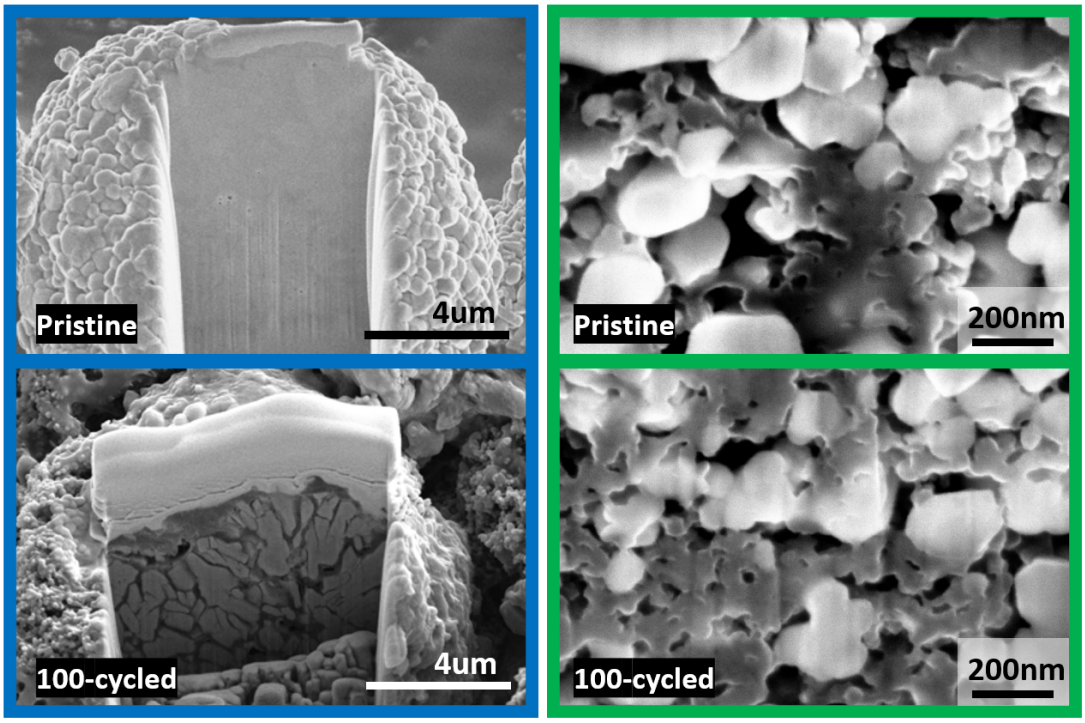

Figure 4.12: Cross sectional images of pristine and 100-cycled μNMC (blue frame) and nNMC (green frame)

resistivity by disconnecting the charge transport pathway in the electrode. It is also important to note that the facets exposed to the electrolyte by the formation of microcracks may be more vulnerable to electrolyte attacks compared to the facets on the surface of the secondary μNMC particles. This is because surface of primary particles exposed by cracking have higher surface energy compared to the surface of the secondary particles. It was attributed to the fact that these surfaces tend to form to minimizing grain boundary energy rather than its surface energy.[143] Thus, it leads to higher activation energy for phase transformation to the rock-salt phase.

4.4 Conclusion

In summary, we have presented an atomic scale analysis of twin boundary defects observed in the classical layered $LiNi_{0.4}Mn_{0.4}Co0.2O_2$ cathode nanoparticles synthesized by polyol method. Cation disordering observed adjacent to twin boundary leads to the formation of a single layer of rock salt-like phase at the boundary. This propagates from center to surface of the particle in radial direction. Furthermore, enhanced electrochemical performance is observed for polyol synthesized $LiNi_{0.4}Mn_{0.4}Co0.2O_2$ compared to the reference material with the identical composition, despite increase parasitic reaction with electrolyte due to larger surface area. Operando XRD shows that electrochemically inactive twin boundary may act as a framework that mitigates c lattice parameter expansion and contraction during charge and discharge process. Cross section images after 100 cycles show that intragranular cracking observed due to repeated volume changes in the reference material is absent in polyol-synthesized sample. We believe that our results can propose a novel approach of considering TB defect in the design of stable intercalation compounds with low internal stress.

Chapter 4, in full, is currently being prepared for submission for publication as: H. Chung; A. Grenier; C. Mejia; R. Huang; K.W, Chapman; S.J. Kim; Y.S. Meng, "Insights into Twin Boundary Defect and Mitigation of Anisotropy Change in Classical Layered Oxide Material for Li-ion batteries," The author was the primary investigator and author of this paper. All the experiment parts were performed by the author except operando XRD analysis.

Chapter 5

Experimental Considerations to Study Li-Excess Disordered Rock Salt Cathode Materials

Cation-disordered rock salt materials have attracted much interest as high energy density cathode materials due to their anionic electrochemical activity, providing them extra capacity, along with their lower cost. They are, however, still the subject of numerous studies as they suffer from poor cyclability and relatively slow kinetics compared to traditional intercalation materials. In this work, several important experimental considerations, that must be taken into account when studying Li-excess cation disordered rock salt cathode materials, are introduced. First, the key synthesis parameters were identified to enable a lower-temperature, morphology-controlled synthesis of the Li_3NbO_4-based disordered rock salt cathodes $Li_{1.3}TM_{0.4}Nb_{0.3}O_2$ (TM = Fe, Mn), using nano-sized precursors. After evaluating the influence of the morphology on the cyclability of the electrode, two key challenges that hinder the practical implementation of these systems are revealed – ambient air-induced surface contamination and electrolyte compatibility. Thermal gravimetric

analysis and X-ray diffraction on the nano-sized cathodes confirmed that prolonged air exposure generates a large amount of surface species, responsible for the large decrease in the first discharge capacity. Moreover, the influence of the electrolyte on the evolution of the cathode electrolyte interphase was investigated via a combination of electrochemical impedance spectroscopy and X-ray photoelectron spectroscopy. The results show that cation-disordered rock salt cathodes go through significant Li-salt degredation and develop thick cathode-electrolyte interphase with the electrolytes compatible with Li-excess layered cathode materials $Li[Li_{0.144}Ni_{0.136}Co_{0.136}Mn_{0.544}]O_2$ highlighting the importance of evaluating and finding compatible battery chemistries.

5.1 Introduction

The ever-growing demand in energy storage has a large impact on the research of high capacity electrode materials for Li-ion batteries. In previous decades, lithium-excess transition metal (TM) oxides have attracted attention, both in academia and industry, as one of the most promising next-generation cathode materials.[144,145] This class of materials pushes the limits of the TM redox storage capacity by additionally activating the anionic redox of the lattice oxygen. Recently, several groups introduced a new paradigm with the cation-disordered rock salt (DRS) structured cathode materials.[23,146,147] These materials were previously believed not to be electrochemically active as the random distribution of the cations in the cell prevents the formation of distinct Li diffusion pathways required for cycling.[148] However, computational and experimental studies confirmed that a percolation network of 0-TM channels develops when the Li content exceeds ≈ 1.09, leading to a reversible capacity as in traditional intercalation cathode materials.[149] This discovery, by changing the design principles of cathode materials, vastly expanded the chemical space of possible cathodes. Over the last few years, several Li-excess DRS cathode materials were

synthesized, developed, and characterized to evaluate their potential as the next generation of cathode materials.[24,147,150,151]

Despite the growing interest in DRS cathode materials, there are still limited studies of their synthesis mechanisms and how the synthesis conditions affect their morphology and electrochemical performances. As one of the most studied classes of DRS materials, TM-substituted Li_3NbO_4 exhibits high discharge capacities - around $300\,mA\,h\,g^{-1}$ at $60\,°C$.[23] These materials are usually prepared by either high-temperature solid-state synthesis or mechanochemical synthesis, starting from TM oxide precursors and a Li-source, such as Li_2CO_3 or Li_2O. Nevertheless, the solid-state synthesis method comes with its own disadvantages. For instance, its long dwelling at high temperature leads to Li evaporation and particle agglomeration.[151–153] The mechanochemical synthesis process, which involves high energy ball-milling of the reagents without heat-treatment, allows for the obtention of smaller particles compared to those obtained through the solid-state methods.[147,154–156] Unfortunately, it also generates defects and/or amorphous species during synthesis, making the characterization of the product extremely challenging. Additionally, the long high energy ball milling step often generates impurities coming from the grinding media, such as ZrO_2 or WC.[154,157] As a result, both of these methods are not adequate to characterize the effect of particle morphology on the kinetic limitations of DRS materials.[23]

Herein, we conducted a comprehensive study of the synthesis of Li_3NbO_4-based cathode materials and analyzed various parameters of the solid-state reaction that can affect both the transition metal segregation and the particle morphology. Using nano-sized precursors, we have successfully produced phase-pure DRS material at reduced temperature, while controlling the particle morphology. The electrochemical performances were then evaluated and compared with those of micron-sized materials reported in literature.[158,159] Based on this study, the cycling stability of these materials, although improved, is still limited compared with other anionic redox cathodes, such as Li-excess layered materials.

Thus, we have identified two important challenges that hinder the practical implementation of DRS cathode materials. First, we have investigated how ambient air exposure can lead to the formation of surface species using X-ray diffraction (XRD), thermogravimetric analysis (TGA), and X-ray photoelectron spectroscopy (XPS). We then proposed a heat-treatment process to partially reverse the contamination of the air-exposed samples. Finally, we have investigated the electrolyte compatibility by testing DRS materials with two other advanced electrolytes, commonly used in the literature for Li-excess layered material. Even compared with other high-voltage cathode materials, the improper choice of electrolyte for a DRS material has a drastic effect associated with the formation of an excessive cathode electrolyte interphase (CEI) layer. The study of these two main factors aims at providing guidelines to the scientific community when evaluating the practical performances of DRS cathode materials.

5.2 Experimental Methods

5.2.1 Synthesis of Materials

Li_3NbO_4, $Li_{1.3}Fe_{0.4}Nb_{0.3}O_2$, and $Li_{1.3}Mn_{0.4}Nb_{0.3}O_2$ were synthesized by solid-state reaction using two different sized metal oxide precursors. Nano-sized metal oxide precursors were used for nanoparticle cathode synthesis, whereas micron-sized metal oxide precursors were used for non-morphology-controlled cathode synthesis.

Nano-sized Nb_2O_5 precursor (n-Nb_2O_5) was synthesized via solvothermal method. 0.5 g of Nb_2Cl_5 (Alfa Aesar, $> 99.9\%$) was added to 50 ml of anhydrous benzyl alcohol (Sigma-Aldrich, $> 99.8\%$) while continuously stirring. The mixture was transferred into a 100 ml Teflon cup, slid into a stainless-steel autoclave, and carefully sealed in an Ar-filled glovebox (MBraun, Germany). The autoclave was heated in a furnace at 240 °C for 31 hours. The resulting solution was centrifuged to separate the white Nb_2O_5 product. The product

was repeatedly washed with ethanol and finally dried in vacuum at 60 °C.

Nano-sized Mn_2O_3 precursor (n-Mn_2O_3) was prepared by polyol method. In this set up, 0.02 mol of $Mn(CH_3COO)_2 \cdot 4H_2O$ (Acros, > 99%) and 0.02 mol of citric acid (Sigma-Aldrich, > 99.5%) were added to 100 ml of diethylene glycol (Sigma, > 99%) in a 250 ml round bottom flask connected to a reflux. The mixture was continuously stirred while it was heated to 220 °C for 2 h and cooled back down to room temperature. Through this solution reaction, a light brown coloured precipitate was harvested. The precipitate was washed with ethanol several times via centrifugation-redispersion cycles to remove any possible residual reactants. Afterward, the precipitate was heated at 450 °C for 12 h, manually mixed with an agate mortar and pestle, and then heated again at 600 °C for 2 h to obtain the final product. All the reactions and heat-treatments were conducted in air. Nano-sized Fe_2O_3 (n-Fe_2O_3) has been purchased (Aldrich, nanopowder) and used without further treatment. XRD and SEM of all metal oxide precursors are shown in Figure 5.1 and 5.2. For Li_3NbO_4 nanoparticle preparation, stoichiometric amounts of

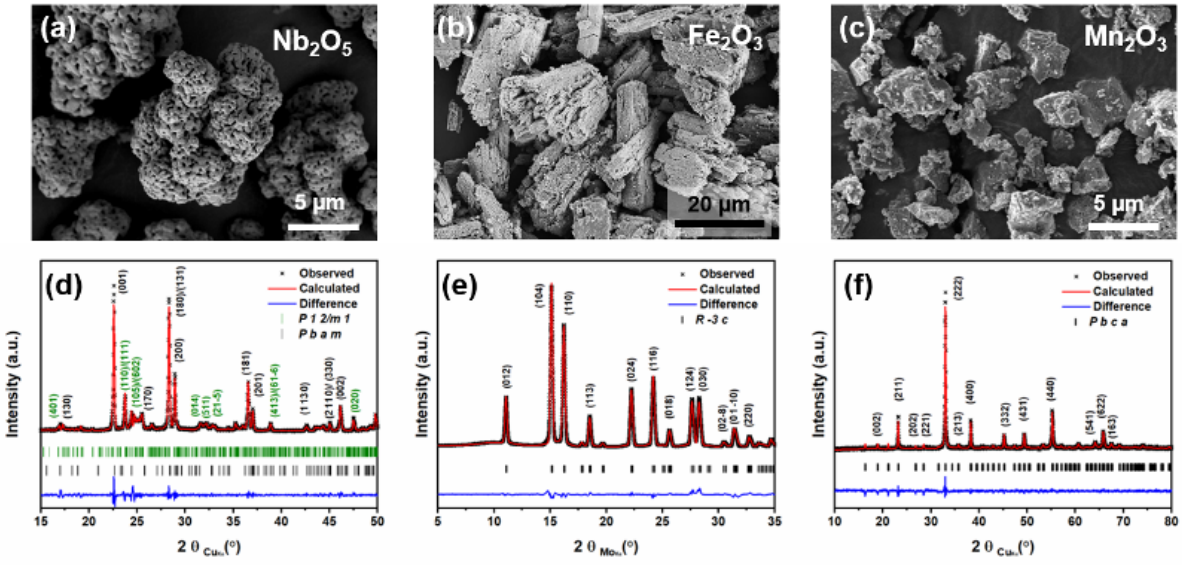

Figure 5.1: SEM images and XRD patterns of commercial micron-sized a, d) Nb_2O_5, b, e) Fe_2O_3, and c, f) Mn_2O_3 precursors used for the solid-state synthesis.

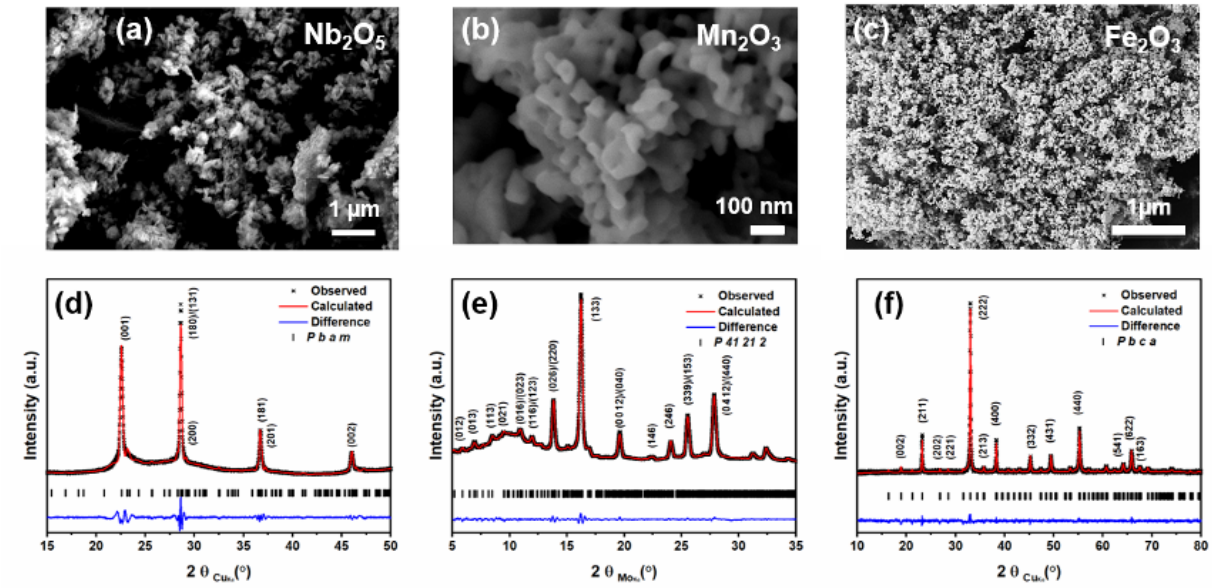

Figure 5.2: SEM images and XRD patterns of nano-sized a, d) Nb_2O_5, b, e) Fe_2O_3, and c, f) Mn_2O_3 precursors used for the solid-state synthesis.

LiOH·H2O (Sigma-Aldrich, $> 98\%$) and n-Nb_2O_5 were manually mixed in an agate mortar and pestle for 15 min. The mixed powder was then pelletized, put into a quartz tube, and heated at 700 °C for 1 h in air. The pellet in the quartz tube was then quenched in a dry ice/isopropanol bath.

$Li_{1.3}Fe_{0.4}Nb_{0.3}O_2$ and $Li_{1.3}Mn_{0.4}Nb_{0.3}O_2$nanoparticles were prepared from stoichiometric amounts of Li_2CO_3, n-Nb_2O_5, and n-Fe_2O_3 or n-Mn_2O_3 respectively. These precursors were first thoroughly mixed by wet mechanical ball milling (Retsch PM 100) at 400 rpm for 2 h. A zirconia jar and 5 mm-diameter yttria-stabilized zirconia balls were used with isopropanol solvent. The obtained product was dried in air and pressed into a pellet before heat-treatment. In a typical synthesis, $Li_{1.3}Fe_{0.4}Nb_{0.3}O_2$ was calcined at 750 °C for 5 h in air, and $Li_{1.3}Mn_{0.4}Nb_{0.3}O_2$was calcined at 750 °C for 5 h in Ar in a tube furnace. During the study of the effect of the temperature, a 10% excess of Li_2CO_3 was added for the samples when high temperature heat treatments were performed (950 °C and 1050 °C) in order to compensate for Li evaporation.

Non-morphology controlled Li_3NbO_4, $Li_{1.3}Fe_{0.4}Nb_{0.3}O_2$, and $Li_{1.3}Mn_{0.4}Nb_{0.3}O_2$ were prepared from Li_2CO_3 and micron-sized metal oxide precursors – Nb_2O_5 (Alfa Aesar, $> 99.9985\%$) and Fe_2O_3 (Strem, $> 99.995\%$) or Mn_2O_3 (Strem, $> 99\%$). Li_3NbO_4 was prepared similarly to previous reports.[23] For $Li_{1.3}Fe_{0.4}Nb_{0.3}O_2$ and $Li_{1.3}Mn_{0.4}Nb_{0.3}O_2$, Li_2CO_3, Nb_2O_5, and Fe_2O_3 or Mn_2O_3 were mixed by wet mechanical ball milling at 400 rpm for 2 h in a zirconia jar using 5 mm-diameter yttria-stabilized zirconia balls and isopropanol solvent. The obtained products were also dried and pelletized before heat-treatment. In a typical synthesis, non-morphology controlled $Li_{1.3}Fe_{0.4}Nb_{0.3}O_2$ and $Li_{1.3}Mn_{0.4}Nb_{0.3}O_2$were heat-treated for 24 h at 950 °C in air (for Fe sample) or in Ar (for Mn sample). Here again, a 10% excess of Li_2CO_3 was added for 950 °C and 1050 °C heat-treatments to compensate for Li evaporation at high temperatures, while a stoichiometric amount was used for lower temperatures. All the disordered rock salt cathode materials in this study were stored in an Ar-filled glovebox before use. Li-excess NMC ($Li[Li_{0.144}Ni_{0.136}Co_{0.136}Mn_{0.544}]O_2$), used for the electrolyte study, was synthesized as in a previous study.[121]

5.2.2 Material Characterization

The crystal structures were characterized by X-ray diffraction (XRD) using Cu K_α ($\lambda = 1.54059$ Å) or Mo K_α ($\lambda = 0.71073$ Å) radiations. For Cu K_α radiation, a Bruker D8 diffractometer was used, and the data was collected by continuous scanning of a detector covering an angular range from 10.0° to 80.0°. A Bruker APEX II Ultra diffractometer was used for Mo K_α radiation. The diffraction images gathered by the 2D detector were merged and integrated in DIFFRAC.EVA (Bruker, 2018) to produce 2d-plots. All Rietveld refinements were conducted using a pseudo-Voigt profile in FullProf software.[51] Zeiss Sigma 500 or FEI Apreo scanning electron microscope (SEM) with energy dispersive X-ray spectroscopy (EDS) was used to characterize the particle morphology and the elemental distribution. Thermogravimetric analysis (TGA) experiments were performed using a

Perkin-Elmer Simultaneous Thermal Analyzer (STA) 6000. The sample was placed on a ceramic pan under a continuous 20 ml/min N_2 gas flow during the measurement. The testing procedure consisted of ramping up the temperature at a rate of 5 °C/min, with isothermal dwell time of 1 hour at 150 °C, 350 °C, and 500 °C. X-ray photoelectron spectroscopy (XPS) was performed using a Kratos Axis Supra spectrometer with an Al anode source operated at 15 kV. For surface contamination study, all the spectra were calibrated to Nb 3d peak associated with Nb^{5+} at 207.1 eV. O 1s core region was scaled with lattice O peak at 530.2 eV. C 1s core region was scaled according to the nearby Nb 3d peak area. For the Li-rich NMC and pristine Mn DRS samples in the electrolyte compatibility study, the C-C peak associated with carbon black was aligned to 284.8 eV for energy calibration. Due to differential charging effects for the Mn-DRS samples (see Figure 5.3 on CB/PVdF), the Nb 3d peak associated with Nb^{5+} was aligned to 207.1 eV to identify changes relative to the active material. The compositional analysis was determined based on the relative sensitivity

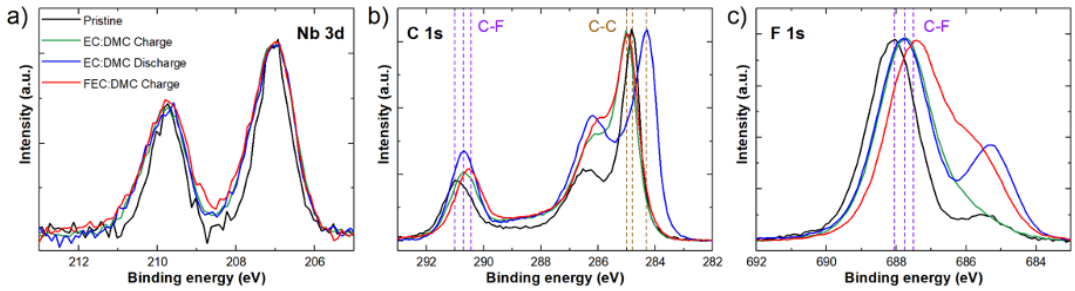

Figure 5.3: XPS spectra of the C 1s region, F 1s region, and Nb 3d region of $Li_{1.3}Mn_{0.4}Nb_{0.3}O_2$ in pristine state, after first charge and discharge for EC:DMC (3:7) with 1M $LiPF_6$, and after the first charge for FEC:DMC (1:4) with 1M $LiPF_6$.

factors of the Li 1s, P 2p, F 1s, and O 1s. The Li 1s has a very low sensitivity factor and can strongly depends on the choice of background. As such, the Li 1s is included in the compositional analysis in Figure 5.20 mainly to highlight the large variation in lithium at the CEI observed with different electrolytes for Li-rich NMC and Mn-DRS. The thickness calculation was based on approximating the cathode particles as a spherical system with a

uniform CEI overlayer, following other CEI studies,[137,160,161] and using the model given by Baer *et al.*[162] For simplicity, the thickness was based on the relative intensity of O 1s CEI components versus the O 1s TM-O lattice peak. All spectra were normalized based on the closest active material peak in binding energy so that collected photoelectrons were from a similar probing depth. The F 1s (687 eV) was scaled by the Mn 2p (640 eV), the O 1s was scaled by the lattice oxygen peak, and the P 2p (135 eV) and Li 1s (56) were scaled by the Mn 3p (50 eV). A table of peak positions for CEI components are detailed in Table 5.1.

Table 5.1: Summary of XPS peak assignments.

Peak	**Binding energy (eV)**	**Assignment**
Li 1s	∼55.6	Li_2CO_3
	∼56.1	LiF
	∼56.3	Lattice Li
	∼57.53	Li-P-F
P 2p	∼134.2	P-O/P-O-F
	∼136.2	Li-P-O-F
	∼137.3	Li-P-F
O 1s	∼530.2	Lattice O
	∼531.2	-O-H
	∼532.3	C=O/CO_3
	∼533.5	C-O
	∼534.5	P-O-F
F 1s	∼685.6	LiF

5.2.3 Electrochemical Characterization

The summary of the electrochemical testing conditions used in this study, including details on the coin cell fabrication, is listed in Table 5.2 and Table 5.3.

To fabricate $Li_{1.3}Fe_{0.4}Nb_{0.3}O_2$, and $Li_{1.3}Mn_{0.4}Nb_{0.3}O_2$cathode electrodes, the powder of active material and carbon black were first mixed in 4:1 weight ratio using a planetary ball mill (Retsch PM 100) for 2 h at 300 rpm, in a zirconia jar with 3 mm-diameter yttria-

Table 5.2: Coin cell testing specifications used for nanosized $Li_{1.3}TM_{0.4}Nb_{0.3}O_2$ (TM = Fe, Mn).

Fe-/Mn-DRS Specification	
Active material	$Li_{1.3}Fe_{0.4}Nb_{0.3}O_2$ or $Li_{1.3}Mn_{0.4}Nb_{0.3}O_2$ - 72%
Conductive agent	SPC65 - 18%
Binder	HSV900 - 10%
Counter electrode	Li metal chip (Thickness: 1 mm, diameter: 15.4 mm)
Separators	Celgard 2325
Electrolyte type	1M $LiPF_6$ in EC:DMC = 3:7 vol%
Electrolyte amount	55 µl
Cell type	CR2032
Coin cell setup	0.5 mm thick spacer and one spring at anode side
Voltage range	1.5 - 4.8 V
Test protocols	Rest for 6 h after assembling, then 20 $mA\,g^{-1}$ (equivalent to 0.75 - 0.89 $mA\,cm^{-2}$) for all cycles at room temperature
Active material loading	3.7 - 4.4 $mg\,cm^{-2}$

stabilized zirconia balls. Polyvinylidene fluoride (PVDF) was then added to the mixture in a Thinky mixer vial, such that the composite consists of 72 wt.% active materials, 18 wt.% carbon black, and 10 wt.% PVDF. After adding N-methyl pyrrolidone (NMP) to the mixture, the slurry was made by mechanical mixing in a Thinky mixer. The slurry was casted on an aluminium foil used as current collector and dried at 80 °C in vacuum overnight. As-prepared electrodes were punched, uniaxially pressed about 180 MPa, and then stored in an Ar-filled glovebox before cell assembly.

For electrochemical characterization, lithium metal was used as the negative (counter) electrode. The baseline electrolyte was a 1 M solution of lithium hexafluorophosphate ($LiPF_6$) in a 3:7 volume mixture of ethylene carbonate (EC) and dimethyl carbonate (DMC). For the electrolyte compatibility study, two additional electrolytes were prepared: (i) 1 M of lithium hexafluorophosphate ($LiPF_6$) in a 3:7 volume mixture of ethylene carbonate (EC) and dimethyl carbonate (DMC) with 2 wt.% lithium difluoro(oxalate)borate (LiDFOB) as an additive (denoted as LiDFOB electrolyte), and (ii) 1 M $LiPF_6$ in a 1:4 volume

Table 5.3: Coin cell testing specifications used in electrolyte compatibility study.

LR-NMC Specification	
Active material	$Li[Li_{0.144}Ni_{0.136}Co_{0.136}Mn_{0.544}]O_2$ - 80%
Conductive agent	CPS65 - 10%
Binder	HSV900 - 10%
Counter electrode	Li metal chip (Thickness: 1 mm, diameter: 15.4 mm)
Separators	Celgard 2325
Electrolyte type	1) Baseline: 1M $LiPF_6$ in EC:DMC = 3:7 vol% 2) LiDFOB: 1M $LiPF_6$ in EC:DMC = 3:7 vol% with 2 wt.% LiDFOB additives 3) FEC: 1M $LiPF_6$ in FEC:DMC = 1:4 vol%
Electrolyte amount	55 µl
Cell type	CR2032
Coin cell setup	0.5 mm thick spacer and one spring at anode side
Voltage range	2.0 - 4.8 V
Test protocols	Rest for 6 h after assembling, then 12.5 $mA\,g^{-1}$ (equivalent to 0.044 - 0.050 $mg\,cm^{-2}$) for first cycle, the rest at 25 $mA\,g^{-1}$ (equivalent to 0.088 - 0.100 $mg\,cm^{-2}$) at room temperature
Active material loading	3.5 - 4.0 $mg\,cm^{-2}$

Mn-DRS Specification	
Active material	$Li_{1.3}Mn_{0.4}Nb_{0.3}O_2$ - 72%
Conductive agent	SPC65 - 18%
Binder	HSV900 - 10%
Counter electrode	Li metal chip (Thickness: 1 mm, diameter: 15.4 mm)
Separators	Celgard 2325
Electrolyte type	1) Baseline: 1M $LiPF_6$ in EC:DMC = 3:7 vol% 2) LiDFOB: 1M $LiPF_6$ in EC:DMC = 3:7 vol% with 2 wt.% LiDFOB additives 3) FEC: 1M $LiPF_6$ in FEC:DMC = 1:4 vol%
Electrolyte amount	55 µl
Cell type	CR2032
Coin cell setup	0.5 mm thick spacer and one spring at anode side
Voltage range	1.5 - 4.8 V
Test protocols	Rest for 6 h after assembling, then 10 $mA\,g^{-1}$ (equivalent to 0.034 - 0.036 $mg\,cm^{-2}$) for all cycles at room temperature
Active material loading	3.4 - 3.6 $mg\,cm^{-2}$

mixture of fluoroethylene carbonate (FEC) and dimethyl carbonate (DMC) (denoted as FEC electrolyte). The moisture contents of the three electrolytes were verified using a Coulometric Karl Fisher Titrator and were in the range of $10-15$ ppm.

All the cells used for the electrochemical tests were assembled using R2032-type coin cells in an Ar-filled glovebox. n-Li_3NbO_4 cell was charged and discharged between 1.0 and 4.8 V with 0.0229 mA/cm^2 (equivalent to 10 $mA\,g^{-1}$) as in the literature.[23] $Li_{1.3}TM_{0.4}Nb_{0.3}O_2$(TM = Fe, Mn) cells were cycled between 1.5 and 4.8 V with a current density of $0.075-0.089\,mA/cm^2$ (equivalent to 20 $mA\,g^{-1}$) for synthesis and air contamination section. For the electrolyte compatibility study, a lower current was used to ensure that any degradation reactions were not kinetically limited. Therefore, all the $Li_{1.3}Mn_{0.4}Nb_{0.3}O_2$ cells were cycled between 1.5 and 4.8 V with a current density of $0.034-0.036\,mA/cm^2$ (equivalent to 10 $mA\,g^{-1}$). Both an Arbin BT2000 (Arbin Instruments, USA) and a Neware Battery Test System (Neware Technology Ltd., China) battery cyclers were employed to carry out all the galvanostatic cycling tests.

Additionally, electrochemical impedance spectroscopy (EIS) was performed using a Solartron 1260 impedance analyzer, with an applied AC potential of 10 mV in the frequency range of 1 MHz to 0.1 Hz. The EIS measurements for each electrolyte were performed on the same coin cell in four steps: as assembled, after a 6 h resting time, after the first charge, and after the first discharge. The Nyquist impedances were fit using Zview software (ver. 3.5f, Scribner Associates, Inc.). Equivalent circuits are shown in Figure 5.4 with the fitted parameters listed in Table 5.4.

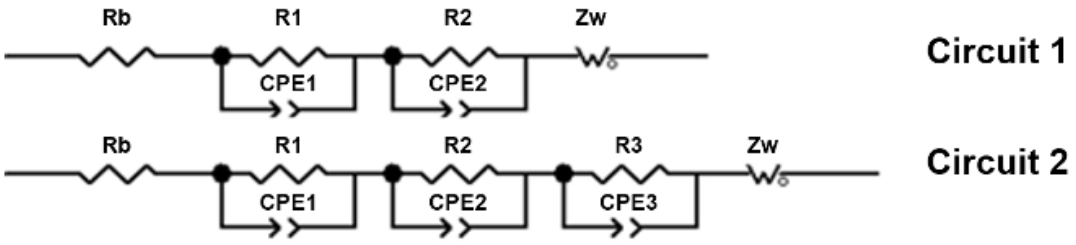

Figure 5.4: Equivalent circuits used for the fitting of the Nyquist plots. Circuit 1 was used for the pristine, rested, and 1st charge samples, whereas Circuit 2 was used for the 1st discharge samples.

Table 5.4: Fitting parameters in the equivalent circuit models (Figure 5.4) used in the electrochemical impedance (EIS) data for $Li_{1.3}Mn_{0.4}Nb_{0.3}O_2$ (Mn-DRS) and $Li[Li_{0.144}Ni_{0.136}Co_{0.136}Mn_{0.544}]O_2$ (LR-NMC) materials in different electrolytes.

	Electrolyte	Samples	R_b (Ω)	R1 (Ω)	R2 (Ω)	R3 (Ω)
Disordered rock salt $Li_{1.3}Mn_{0.4}Nb_{0.3}O_2$	EC:DMC (3:7) with 1M $LiPF_6$	Bare	1.319	24.61	70.36	/
		Rest	1.714	24.06	89.35	/
		1st Charge	1.947	26.05	72.28	/
		1st Discharge	1.804	19.08	93.97	102.8
	EC:DMC (3:7) with 1M $LiPF_6$ + 2% LiDFOB	Bare	1.705	26.04	76.64	/
		Rest	1.734	19.87	51.68	/
		1st Charge	1.985	31.4	70.27	/
		1st Discharge	2.028	21.45	197.3	81.54
	FEC:DMC (1:4) with 1M $LiPF_6$	Bare	1.196	23.08	62.84	/
		Rest	1.104	28.13	66.23	/
		1st Charge	1.566	25.24	149.5	/
		1st Discharge	1.54	43.15	262.1	205.6
Lithium-rich Layered Oxide $Li[Li_{0.144}Ni_{0.136}Co_{0.136}Mn_{0.544}]O_2$	EC:DMC (3:7) with 1M $LiPF_6$	Bare	1.315	3.809	44.27	/
		Rest	1.158	4.21	49.2	/
		1st Charge	3.84	7.31	32.62	/
		1st Discharge	1.363	4.356	10.39	18.36
	EC:DMC (3:7) with 1M $LiPF_6$ + 2% LiDFOB	Bare	1.156	2.868	48.8	/
		Rest	1.426	3.077	60.64	/
		1st Charge	2.734	5.517	46.54	/
		1st Discharge	1.712	6.311	16.63	26.52
	FEC:DMC (1:4) with 1M $LiPF_6$	Bare	2.466	7.102	135.6	/
		Rest	2.441	19.1	178.2	/
		1st Charge	4.696	2.488	53.32	/
		1st Discharge	1.693	2.244	9.755	47.71

5.2.4 Synchrotron XRD

X-ray scattering data was recorded using high-energy X-rays ($\lambda = 0.1666\,Å$) provided by beamline 28-ID-1 at the National Synchrotron Light Source II (NSLS-II) at Brookhaven National Laboratory. Powders were loaded in amorphous SiO_2 tubes (1.1 mm outer diameter, 1 mm wall thickness, F&D Glass) and placed in the furnace for heating.[46] Temperature was increased up to 960 °C in 20 °C steps in air. Two-dimensional images were recorded in

transmission geometry using an amorphous-Si detector, and integrated into one-dimensional XRD patterns using GSAS-II,[47] using LaB_6 (SRM 660c) standards as calibrants.

5.3 Results and discussion

5.3.1 Synthesis Parameters

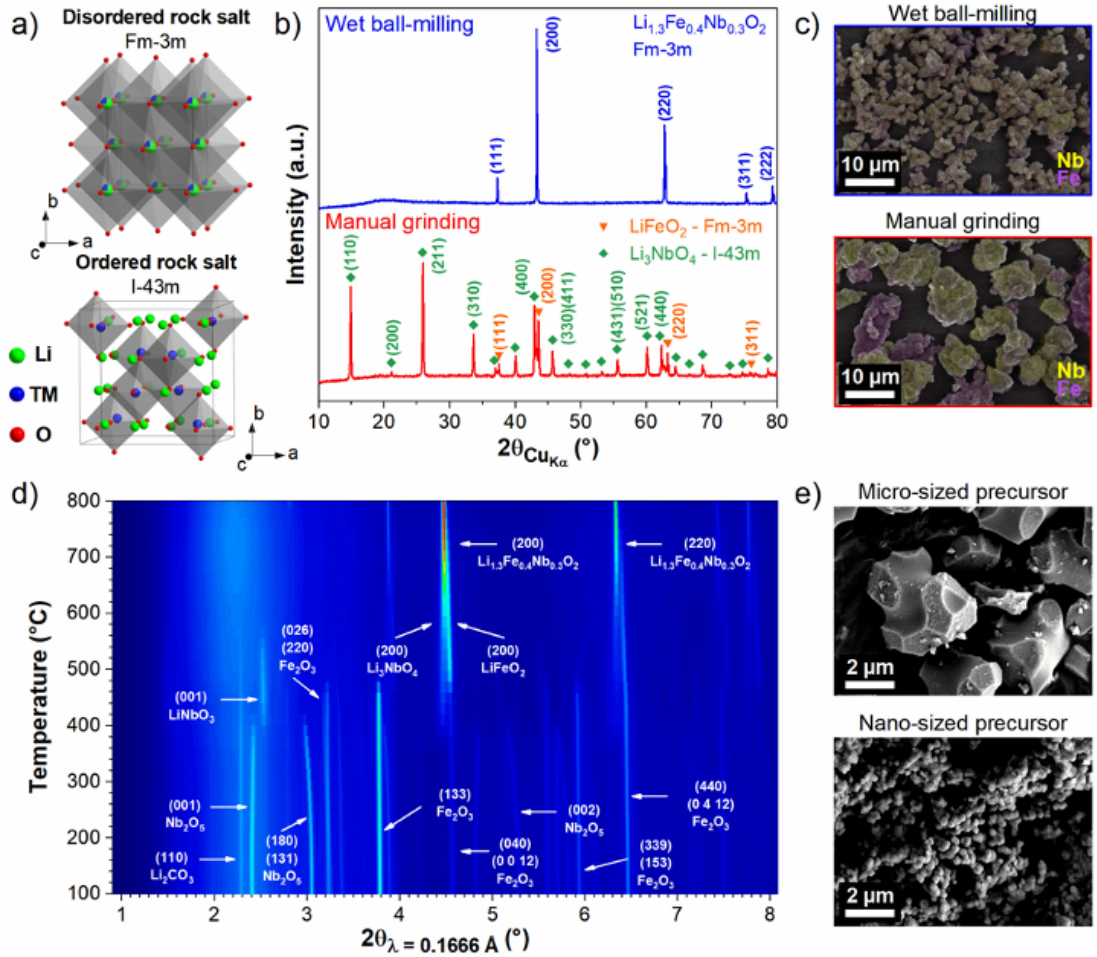

Figure 5.5: a) Crystal structures of disordered and ordered rock salt. Key parameters influencing the morphology and phase obtained during the solid-state synthesis of $Li_{1.3}Fe_{0.4}Nb_{0.3}O_2$: b, c) Precursor mixing process, d) synthesis temperature, and e) morphology of the precursors.

Each step of the synthesis process can have a dramatic effect on the electrochemical

performances of cathode materials. Figure 5.5 highlights three of the parameters that have a major influence on the morphology and phase obtained during the solid-state synthesis of $Li_{1.3}Fe_{0.4}Nb_{0.3}O_2$. These three parameters are: 1) the precursor mixing process, 2) the temperature of the heat-treatment, and 3) the morphology of the precursors used.

Figure 5.5a shows the crystal structures of "disordered" and "ordered" rock salt types Li_3NbO_4. Ordered phase consists of four edge-shared NbO_6 octahedra with Li-ion accommodated in a body-centered cubic lattice, while Nb and Li are randomly distributed in the disordered phase.[23,163] The disordered rock salt phase can be electrochemically active when transition metals (TM), such as Fe or Mn, are used to substitute the Li and Nb. However, as shown on Figure 5.5b, different precursor mixing techniques can affect the material obtained during the synthesis of cation-disordered rock salt phases. When the precursors are mixed manually, the X-ray diffraction (XRD) pattern acquired after the high-temperature heat treatment (24 hours at 950 °C under air) shows a simple mixture of Li_3NbO_4 (cation-ordered rock salt structure, $I\bar{4}3m$) and $LiFeO_2$ (cation-disordered rock salt, $Fm\bar{3}m$). EDS mapping of this same material also indicates that Nb and Fe are segregated, as different particles are either Nb- or Fe-rich, as shown on Figure 5.5c. Figure 5.1 presents the morphology and crystal structure of commercially available Nb_2O_5, Fe_2O_3, and Mn_2O_3, which are the common precursors used for the synthesis of $Li_{1.3}TM_{0.4}Nb_{0.3}O_2$(TM = Fe, Mn).[23,164] All these precursors have micron-sized particles (5–20 µm) and intrinsically high melting points, well beyond typical DRS synthesis temperatures. These chracteristics can hinder the diffusion of the transition metals during synthesis, thus preventing the obtention of a pure phase. Contrary to manual grinding, wet ball-milling can provide a significant reduction of the particle size of the reagents, because it is energetic enough to break down metal oxide particles. Consequently, this effective mixing process alleviates the phase segregation of the final product. XRD shows that a pure $Fm\bar{3}m$ phase is obtained with the same synthesis condition when using ball milling (Figure 5.5b). EDS map also confirms a

homogeneous distribution of Fe and Nb in the synthesized product (Figure 5.5c). These first results show that an effective mixing of the precursors is mandatory to suppress the segregation of the transition metal phases. Based on these findings, all the subsequent syntheses were performed using wet-ball milling.

The *in situ* heating synchrotron XRD experiment conducted for the synthesis of $Li_{1.3}Fe_{0.4}Nb_{0.3}O_2$ using nano-sized precursors is shown in Figure 5.5d. This result gives insight on the range of possible synthesis temperatures, which is another principal synthesis parameter. At lower temperatures, the main peaks of the reagents (Li_2CO_3, Nb_2O_5, and Fe_2O_3) are present, confirming that the wet ball-milling process does not induce any chemical reaction. An intermediate phase, LiNbO3, is formed around 360 °C by the reaction of Li_2CO_3 and Nb_2O_5. As the temperature increases, more Li gets incorporated, generating the cation-disordered rock salt phase Li_3NbO_4 ($Fm\bar{3}m$). In parallel, $LiFeO_2$ ($Fm\bar{3}m$) starts appearing at around 400 °C. By observing the (200) peak of these two DRS phases, it appears that their two different lattices merge into one when the temperature exceeds 760 °C, where the pure $Li_{1.3}Fe_{0.4}Nb_{0.3}O_2$ material is finally obtained. A complementary ex situ XRD study with 5 h of dwell time at each temperature (Figure 5.6) shows that this material has a phase stability window of about 200 °C (between 750 and 950 °C). Beyond this point, the temperature induces phase segregation by forming $LiFe_5O_8$ (P 43 3 2) and Li_3NbO_4 ($I\bar{4}3m$). It is possible that the continued Li evaporation at high temperature partially leads to the formation of $LiFe_5O_8$ and,[46] without Fe substitution, Nb-rich DRS starts to form Li_3NbO_4 ($I\bar{4}3m$) impurities. This indicates that the synthesis temperature of the material should be chosen carefully: higher temperature generally favors complete phase formation, but can also lead to particle agglomeration, higher cost, and partial Li evaporation.

The last critical parameter, also affecting the phase and the morphology of the synthesized product, is the choice of the precursors. In our study, we used two different

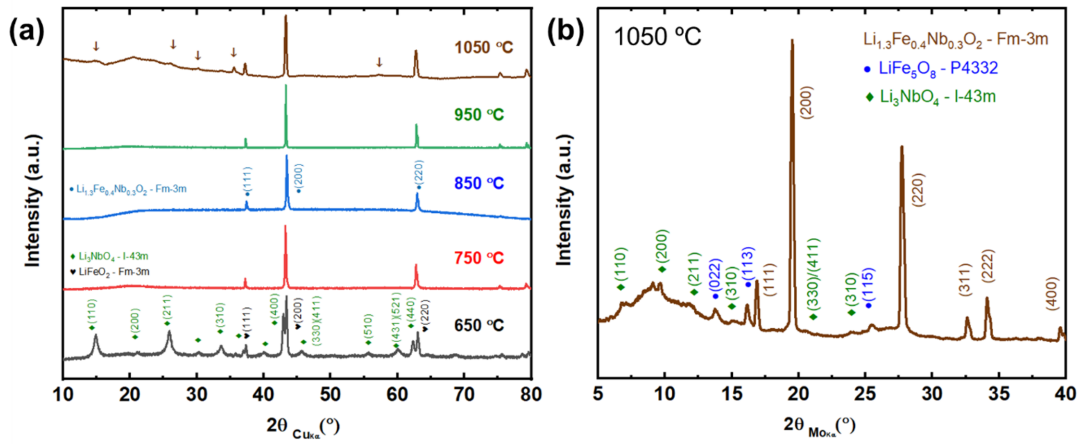

Figure 5.6: a) XRD pattern of $Li_{1.3}Fe_{0.4}Nb_{0.3}O_2$ nano-sized precursor heated treated at different temperature. Arrows mark decomposition species present in 1050 °C heat-treated sample. b) Higher resolution XRD with same sample identifies the impurities to be $LiFe_5O_8$ and Li_3NbO_4.

sized precursors – nano-sized and micron-sized – and compared the resulting materials using XRD and SEM. It appears that nano-sized precursors promote an effective mixing and allow to obtain a pure phase at only 750 °C. This low synthesis temperature is crucial in order to control the particle morphology, because high temperature inevitably leads to increased grain size of the synthesized product. However, for the micron-sized precursor, a temperature of 950 °C is necessary to obtain a pure phase (Figure 5.7). Thus, the control of the morphology is only possible when using nano-sized precursors as they offer a wider synthesis temperature range. While the particle size of $Li_{1.3}Fe_{0.4}Nb_{0.3}O_2$ is around 4 µm in diameter using micron-sized precursors, 200 nm DRS material can be accomplished using nano-sized precursors (Figure 5.5e).

Based on these findings, pure phases of morphology-controlled Li_3NbO_4, $Li_{1.3}Fe_{0.4}Nb_{0.3}O_2$, and $Li_{1.3}Mn_{0.4}Nb_{0.3}O_2$ materials were synthesized using nano-sized metal oxide precursors, as shown in Figure 5.8. All the synthesis conditions, including the synthesis of the nano-sized metal oxide precursors, are described in detail in the Experimental Methods section. In order to study the effect of the particle morphology on the electrochemical

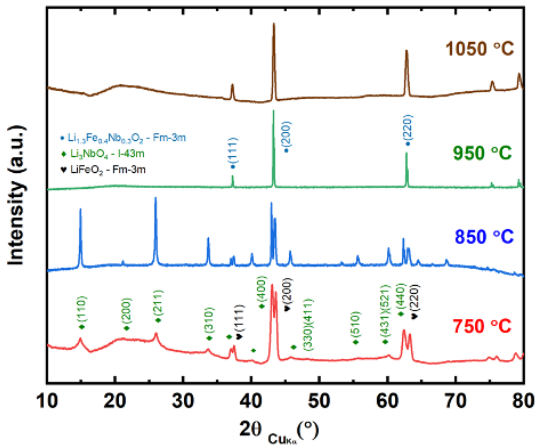

Figure 5.7: XRD pattern of $Li_{1.3}Fe_{0.4}Nb_{0.3}O_2$ micro-sized precursor heated treated at different temperature.

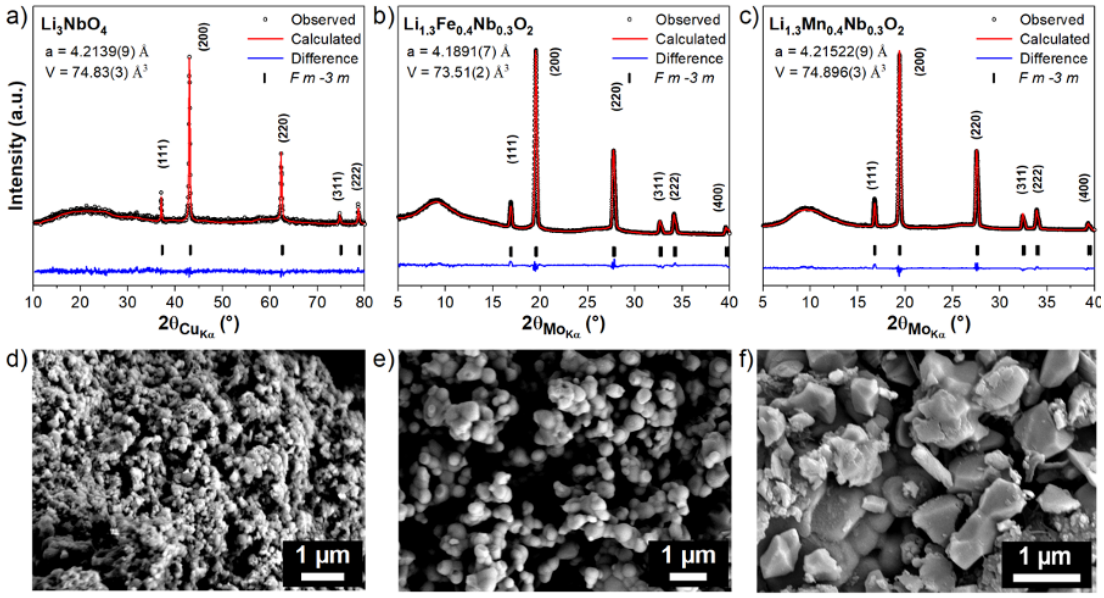

Figure 5.8: Rietveld refinements of the XRD patterns and associated SEM images of a, d) Li_3NbO_4; b, e) $Li_{1.3}Fe_{0.4}Nb_{0.3}O_2$; and c, f) $Li_{1.3}Mn_{0.4}Nb_{0.3}O_2$ obtained by using nano-sized precursors.

performances of DRS materials, low synthesis temperatures (700 to 750 °C) were used to limit the particle growth. For all three samples, XRD patterns can be indexed with the disordered rock salt structure in the $Fm\bar{3}m$ space group, with no noticeable second phase. The broad peaks at $2\theta_{\mathrm{Mo}} \approx 10°$ and $2\theta_{\mathrm{Mo}} \approx 26°$ can be attributed to low-intensity

superstructure peaks.[165] Interestingly, for the non-substituted material (Li_3NbO_4), the use of nano-sized Nb_2O_5 precursor allows to obtain a single-phase disordered rock salt structure, in contrast with the micron-sized precursor conventionally used. During the synthesis, $LiNbO_3$ is formed first (as explained previously) and then temperatures above 700 °C are needed for all the Li to diffuse into the structure and form Li_3NbO_4. However, for non-substituted Li_3NbO_4, the disordered rock salt phase transitions to ordered rock salt ($I\bar{4}3m$ space group) at a similar temperature. Thus, only the ordered rock salt structure can be obtained by solid-state reaction with micron-sized precursors (Figure 5.9a) as reported in the literature.[166] However, using nano-sized Nb_2O_5 and LiOH precursor, the disordered rock salt phase is obtained after 1 hour at 700 °C.

It appears that the increased surface of contact between the reagents favors a fast and homogeneous diffusion of the Li during the synthesis, making the intermediate $LiNbO_3$ phase only short-lived. For both $Li_{1.3}Fe_{0.4}Nb_{0.3}O_2$ and for $Li_{1.3}Mn_{0.4}Nb_{0.3}O_2$, pure phases are obtained with a 5 hours heat-treatment at 750 °C – compared to 24 hours

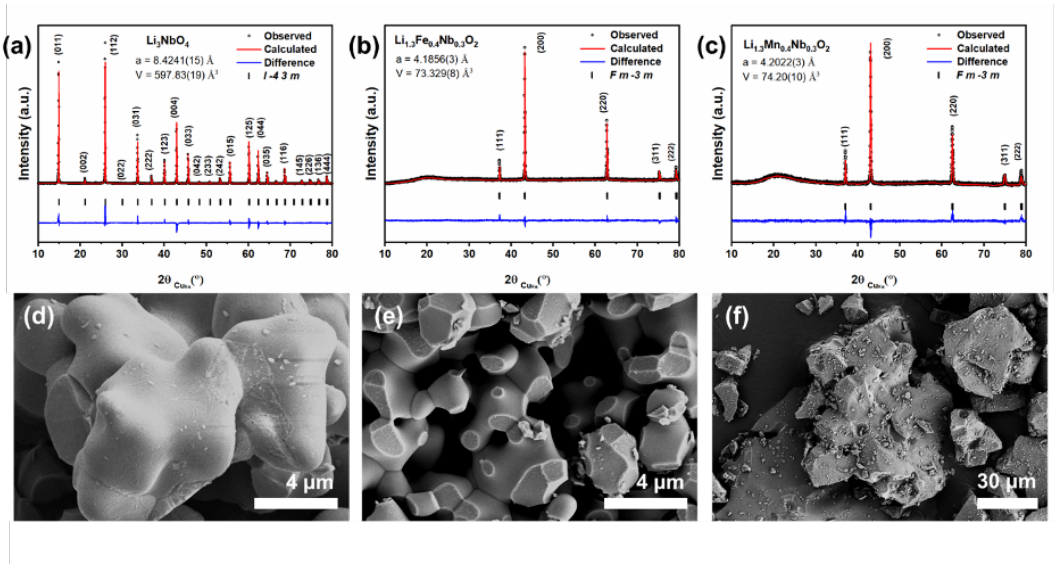

Figure 5.9: Rietveld refinements of the XRD patterns and SEM images of a, d) Li_3NbO_4, b, e) $Li_{1.3}Fe_{0.4}Nb_{0.3}O_2$ and c, f) $Li_{1.3}Mn_{0.4}Nb_{0.3}O_2$ obtained by solid-state synthesis with commercial micron-sized precursors.

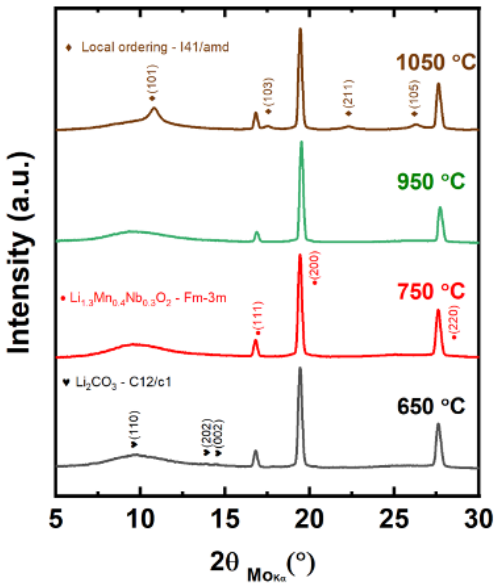

Figure 5.10: XRD pattern of $Li_{1.3}Mn_{0.4}Nb_{0.3}O_2$ nano-sized precursor heated treated at different temperature.

at 950 °C with micron-sized precursors. Figure 5.8d-f shows the resulting morphology of the samples synthesized using these nano-precursors. The particle size of Li_3NbO_4 and $Li_{1.3}Fe_{0.4}Nb_{0.3}O_2$ is limited to 150 nm and 200 nm, respectively, whereas $Li_{1.3}Mn_{0.4}Nb_{0.3}O_2$ particles are around 1 µm. Further efforts were made to reduce the particle size of this last sample by adjusting the temperature and the length of the heat-treatment or the Li source used, but resulted in a non-complete synthesis or impurity formation (Figure 5.10). The morphology of all these samples contrasts from the samples made using micron-sized precursors, presented in Figure 5.9, which show much larger average sizes and wider size distributions.

As reported previously, non-substituted Li_3NbO_4 is not electrochemically active (Figure 5.11). Therefore, we evaluated the electrochemical performances of the Fe- and Mn-substituted materials, at room temperature, in the voltage range of 1.5 to 4.8 V. The 1st, 2nd, 5th, and 10th cycle voltage profiles of $Li_{1.3}Fe_{0.4}Nb_{0.3}O_2$ and $Li_{1.3}Mn_{0.4}Nb_{0.3}O_2$ are shown in Figure 5.12a and c, respectively. Both materials deliver large initial capacities

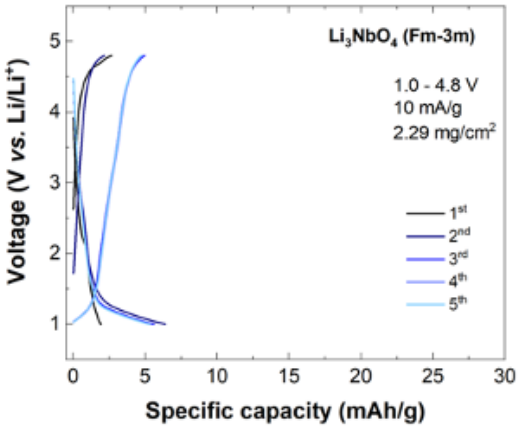

Figure 5.11: Voltage profile of disordered Li_3NbO_4 nanoparticles.

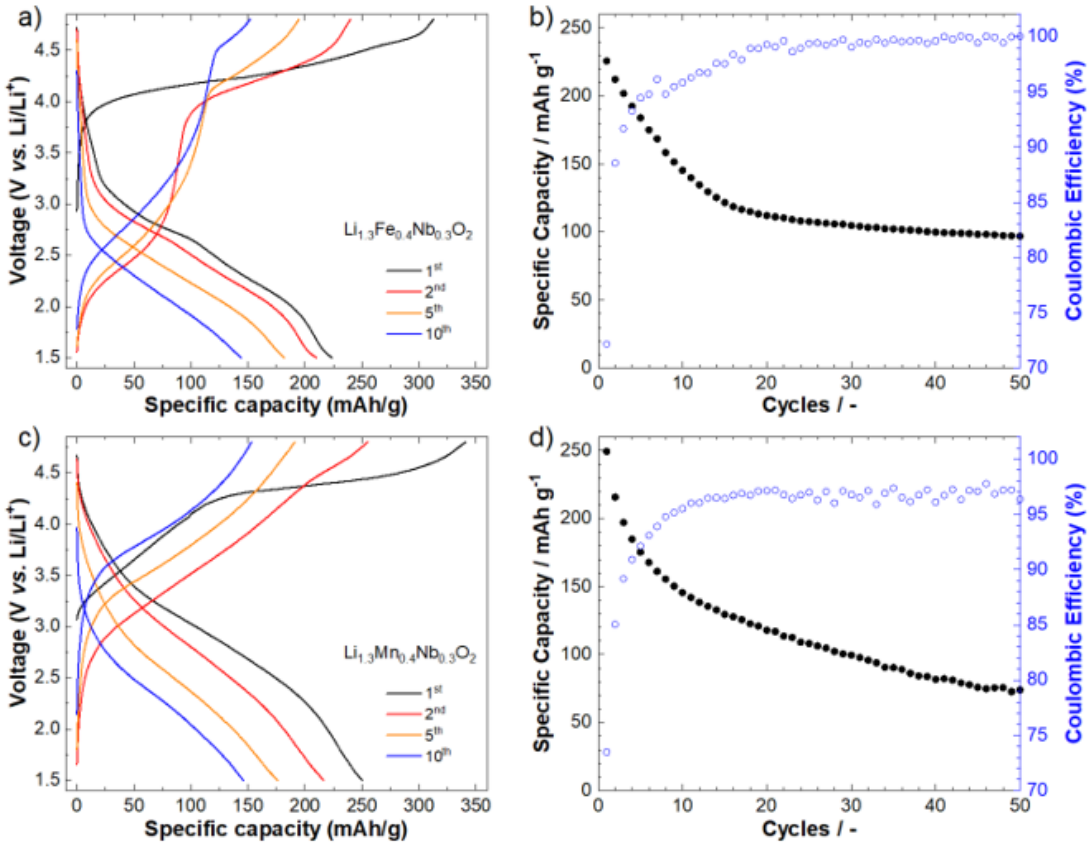

Figure 5.12: Voltage profile and cycling stability of morphology-controlled samples of a, b) $Li_{1.3}Fe_{0.4}Nb_{0.3}O_2$ and c, d) $Li_{1.3}Mn_{0.4}Nb_{0.3}O_2$ in the voltage range of 1.5 - 4.8 V vs. Li/Li^+ at room temperature.

- 312.9 mA h g^{-1} for $Li_{1.3}Fe_{0.4}Nb_{0.3}O_2$ and 339.4 mA h g^{-1} for $Li_{1.3}Mn_{0.4}Nb_{0.3}O_2$ - which indicate that nearly all the lithium was extracted out of the structure. These values are well-beyond the theoretical capacity of $TM^{3+/4+}$ redox couples (118 mA h g^{-1}), as already observed in the literature.[23] Previous studies suggest that,[167] in the case of Fe-substituted DRS, small amounts of Fe^{3+} oxidize to Fe^{4+} during the first charge, similar to what has been observed for Li_4FeSbO_6.[168] Then, with further delithiation, oxygen starts to participate in the reaction as Fe^{4+} is reduced back to Fe^{3+}.[164,167] A follow up work is in preparation to assess the origin of the excess capacity in $Li_{1.3}Fe_{0.4}Nb_{0.3}O_2$. Afterward, the material delivers a discharge capacity of 225.8 mA h g^{-1}. Although subsequent cycles result in the decay of the reversible capacity, the extent is significantly reduced in the 750 °C synthesized nanoparticles, compared to the 950 °C synthesized material as shown in Figure 5.13. In $Li_{1.3}Mn_{0.4}Nb_{0.3}O_2$, Mn oxidizes from 3+ to 4+ similar to Fe-substituted DRS but keeps a 4+ valence state in the bulk even when the extra capacity is accessed.[164] Luo *et al.*, however, reported that repeated oxygen redox leads to significant oxygen loss on the surface, thus causing reduction of surface Mn to 2+.[169] Although both materials display excess capacities beyond the expected $TM^{3+/4+}$ redox, oxidized oxygen or released oxygen gas trigger the formation of a surface layer, causing faster capacity decay than traditional TM redox materials.[167,169] Studies on other cathode materials have shown that nanosizing the material can shorten the distance of lithium diffusion and improve its electrochemical performance.[170] However, despite the improved control in morphology, the continued capacity degradation during cycling shows that the DRS system suffers from additional limitations as well. Therefore, we investigated two other factors that are important for practical performance and strongly intertwined with the cathode morphology – 1) the sensitivity of these materials to surface contamination and 2) the electrolyte compatibility.

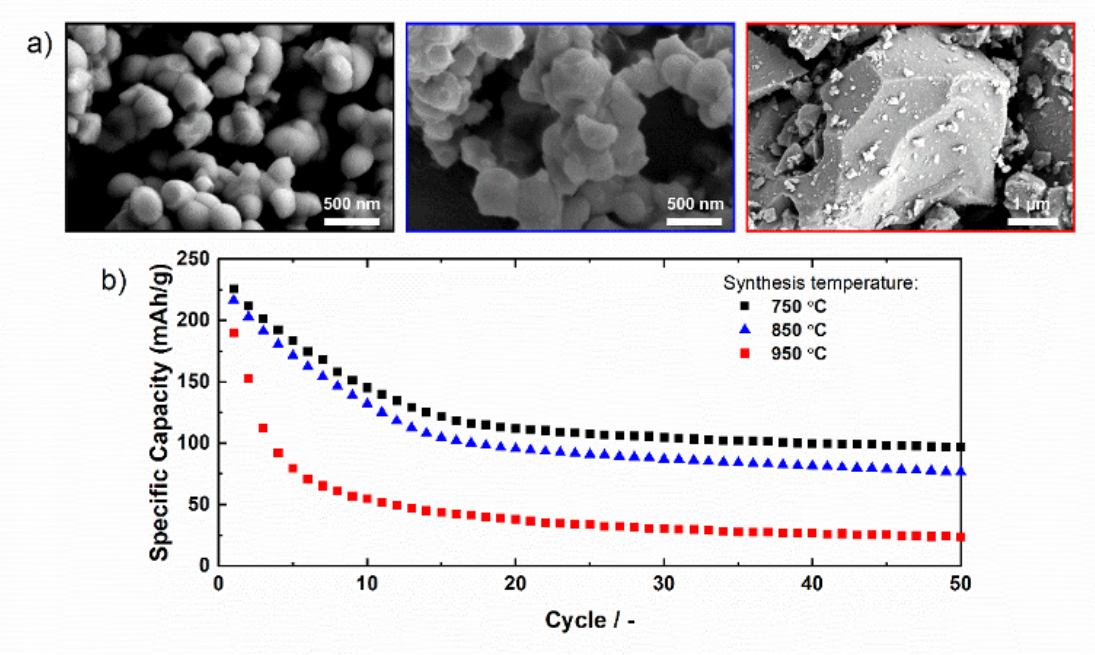

Figure 5.13: a) SEM images and b) cycling stability of $Li_{1.3}Fe_{0.4}Nb_{0.3}O_2$ synthesized at a temperature of 750 °C (black), 850 °C (blue), and 950 °C (red).

5.3.2 Ambient-induced Surface Contamination

It is well-established that impurity species on the surface, caused by the material instability in ambient atmosphere, can have a drastic impact on the performances of the cathode.[126,171,172] Impurity species formed on the surface of active materials can decrease both electronic and ionic conductivities while also consuming part of the active lithium.[173] Nanoparticles, with large surface area, typically have enhanced sensitivity to surface chemistry. Thus, the synthesized nanoparticles were utilized here to help understand how sample handling and storage can affect the DRS material's properties. In this experiment, pristine cathode powders of morphology-controlled $Li_{1.3}Fe_{0.4}Nb_{0.3}O_2$ and $Li_{1.3}Mn_{0.4}Nb_{0.3}O_2$were split into three different vials and exposed to the following conditions: one vial was sealed and stored in an Ar-filled glovebox (Pristine); the second vial was left open under a continuous air flow for 4 weeks (Air-exposed); the third sample was prepared by heat-treating the air-exposed sample at 500 °C for 2 h under air for

$Li_{1.3}Fe_{0.4}Nb_{0.3}O_2$, and under Ar for $Li_{1.3}Mn_{0.4}Nb_{0.3}O_2$(Regenerated). This heat-treatment temperature was selected based on a previous study of the surface contamination of high Ni layered oxide,[126] and then confirmed by the TGA measurements.

Figure 5.14 shows the TGA, electrochemical performances, XRD, and XPS of pristine, air-exposed, and regenerated $Li_{1.3}Fe_{0.4}Nb_{0.3}O_2$ nanoparticles. For the thermogravimetric analysis, presented in Figure 5.14a, all three samples were heated to 750 °C with isothermal segments at 150, 350, and 500 °C, as detailed in the Experimental Methods part. These segments were designed to ensure the complete removal of surface species such as H_2O, $LiHCO_3$, LiOH, and Li_2CO_3, as these evaporate or decompose at temperatures comprised between 100 and 710 °C.[126] The pristine $Li_{1.3}Fe_{0.4}Nb_{0.3}O_2$ material shows negligible weight loss compared with the alumina reference (Figure 5.15), indicating that minimal amount of surface species is present in the sample after the synthesis. On the other hand, the mass loss of the air-exposed sample exceeds 4%, suggesting a severe reaction takes place with the ambient atmosphere. It appears that a large part of the weight loss corresponds to $LiHCO_3$ and LiOH, similar to observations on air-exposed $LiNi_{0.85}Co_{0.10}Al_{0.05}O_2$.[126,174] These results also show that the majority of the impurities can be removed by annealing at 500 °C. As a result, we investigated the possibility of regenerating the air-exposed sample using a heat-treatment at this temperature.

Electrochemical performance of all three samples are presented in Figure 5.14b and c. After the pristine baseline material has been exposed to air, the first discharge is significantly reduced compared to the pristine baseline material, from 225.8 $mA\,h\,g^{-1}$ to 188.5 $mA\,h\,g^{-1}$. This is accompanied by a drastic increase in the polarization of the cell from 80 mV to 650 mV. The regeneration of the sample reduces this polarization and the first discharge capacity is improved, reaching 210.0 $mA\,h\,g^{-1}$. The original capacity and cycling retention are not fully recovered, however, suggesting that a small amount of surface species remains after the heat treatment, such as Li_2CO_3 with higher decomposition

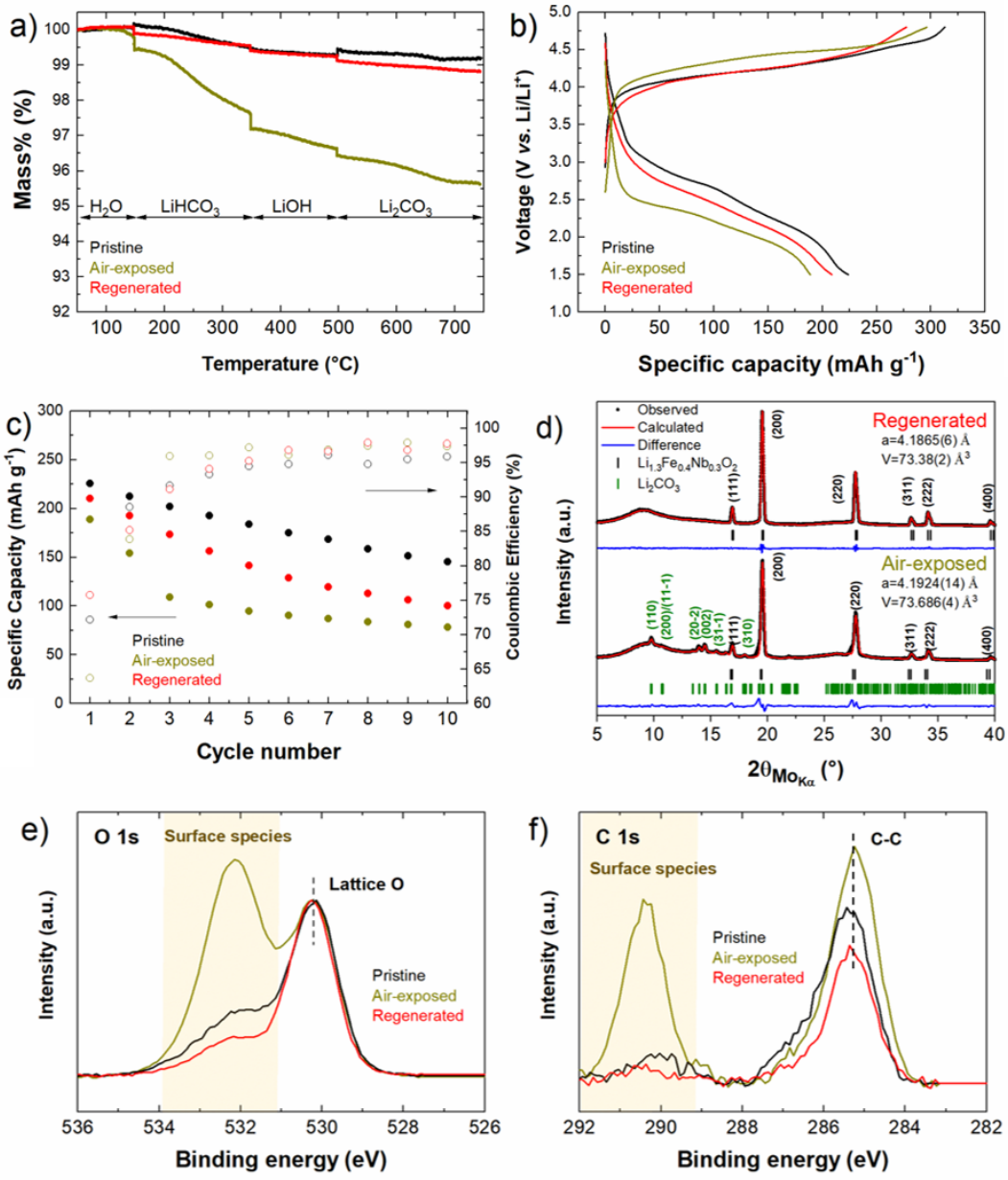

Figure 5.14: Study of the effect of surface contamination on the morphology-controlled sample of $Li_{1.3}Fe_{0.4}Nb_{0.3}O_2$ in pristine state, after 4 weeks of air exposure, and after regeneration by heat treatment: a) Thermogravimetric analysis, b) First voltage profiles, c) Cycling stability, d) Profile matching refinement of the XRD patterns, and XPS measurements of the e) O 1s and f) C 1s core regions.

temperature. This leads to a permanent loss of the active lithium that can then adversely affect the electrochemistry. X-ray diffraction and XPS were additionally conducted to

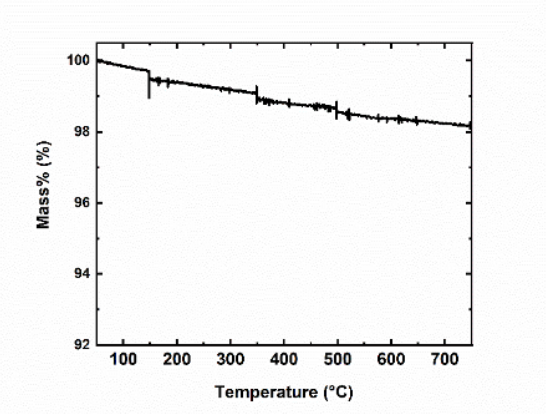

Figure 5.15: Thermogravimetric analysis of Al_2O_3 reference.

compare in detail the structure and surface chemistry of the three samples and understand the origin of the difference in electrochemical performance.

Figure 5.14d presents the X-ray diffraction pattern of air-exposed and regenerated samples. As shown, the diffraction pattern of the air-exposed sample confirms the presence of impurity peaks which were not present in the pristine sample (presented in Figure 5.8b). These peaks can be indexed as lithium carbonate with the C2/c space group. This observation contrasts with most conventional cathode materials, where the impurities formed during air exposure can usually not be detected by XRD, because they are present in limited amounts and in an amorphous state.[113,126] Furthermore, the main diffraction peaks of the phase exhibit a widening at a lower angle (Figure 5.16). This can indicate the formation of other DRS phases, such as FeO, with larger lattice parameters. It is however difficult to determine with certainty the nature of this second impurity as it shares the same space group as the cathode material. Both the peak asymmetry and impurity peaks disappeared by annealing the air-exposed sample at 500 °C. The cell parameters of all three samples are similar - 4.1891(7) Å for the pristine, 4.1924(14) Å for the air-exposed, and 4.1865(6) Å for the regenerated sample- indicating the reactivity of the material with air does not affect the bulk structure.

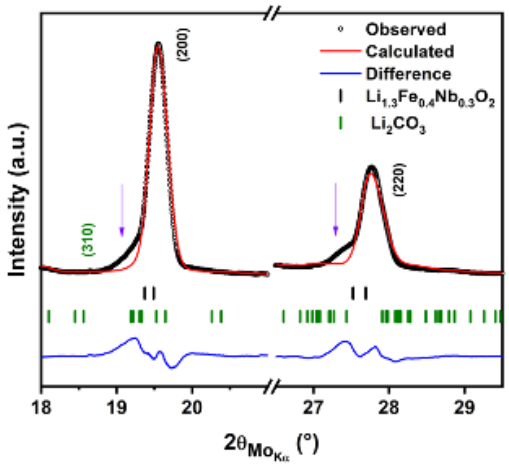

Figure 5.16: Selective theta range of profile matched XRD patterns of air-exposed nanosized $Li_{1.3}Fe_{0.4}Nb_{0.3}O_2$ that highlights the widening at lower angle (marked by purple arrows).

Surface-sensitive XPS measurements, presented in Figure 5.14e and f, clearly show how air-exposure and regeneration affect the cation-disordered rock salt surface chemistry. The O 1s spectra were normalized with respect to the intensity of the peak at 530.2 eV, indexed to $Li_{1.3}Fe_{0.4}Nb_{0.3}O_2$ lattice oxygen. Our results show that, relative to lattice oxygen, a higher binding energy peak around 532.7 eV significantly increases in intensity after air exposure, and then decreases even below the level of the pristine sample after regeneration. This broad peak for the air exposed sample arises from a combination of Li_2CO_3/$LiHCO_3$ ($\approx 532.0 - 532.5$ eV) and LiOH (≈ 531.2 eV) at the surface. Complementary measurements of the C 1s core region further support this assignment, with the air-exposed sample showing a strong peak centered at 290.0 eV that is consistent with Li_2CO_3 (or $LiHCO_3$) formation.[113] This peak is again significantly reduced in the regenerated sample in agreement with the trend observed in the O 1s core region. When approximating the surface oxygen species as a continuous surface layer,[175] the layer thickness can be estimated as 0.46, 1.24, and 0.32 nm for pristine, air-exposed, and regenerated samples, respectively. In conclusion, although small amount of surface species, such as LiOH and Li_2CO_3, develop during the

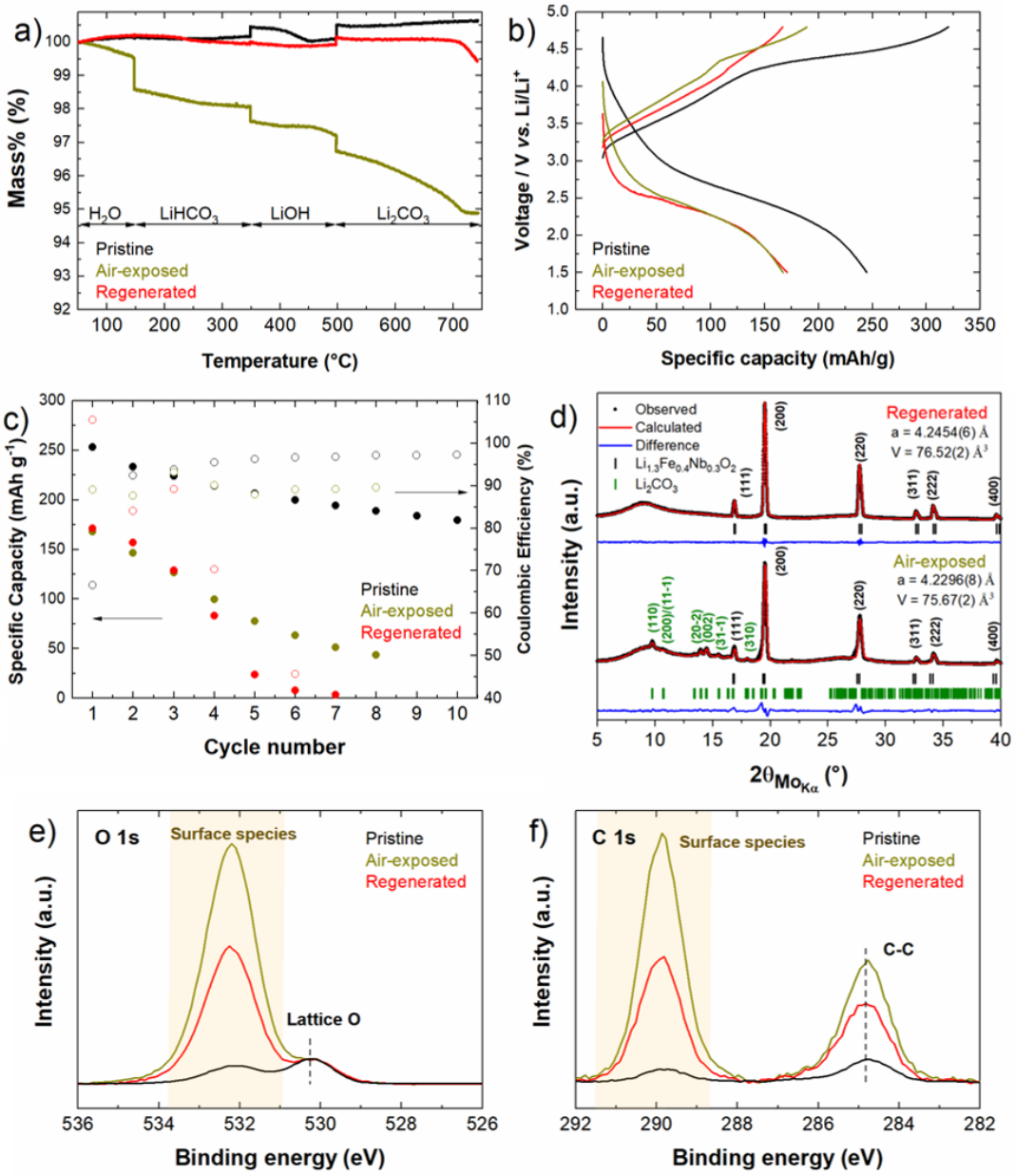

Figure 5.17: a) Rietveld refinement of the XRD patterns of nano-$Li_{1.3}Mn_{0.4}Nb_{0.3}O_2$ after 10 days of air exposure and after regeneration by heat treatment. b) Thermogravimetric analysis of nano-$Li_{1.3}Mn_{0.4}Nb_{0.3}O_2$ in the pristine state, after 10 days of air exposure, and after regeneration by heat treatment. c) First voltage profiles and cycling performances the same three samples.

synthesis of $Li_{1.3}Fe_{0.4}Nb_{0.3}O_2$, the amount significantly increases during the storage in ambient air. Post-annealing mostly decomposes the surface species developed during the

synthesis and storage, resulting in the thinnest surface overlayer.

A similar study was performed on the nanoparticles of $Li_{1.3}Mn_{0.4}Nb_{0.3}O_2$ and the results are presented in the supplementary information (Figure 5.17). In this case, Li_2CO_3 was only detected as a trace amount on the diffraction pattern, which can be explained by the smaller surface area of this material compared to the Fe-substituted sample. The TGA and XPS results nevertheless demonstrate a larger amount of impurities, suggesting the presence of amorphous phases at the surface of the cathode. This is also confirmed by the drastic degradation of the capacity of the material. The first discharge capacity of the air-exposed sample was only $167.8\,\mathrm{mA\,h\,g^{-1}}$ compared to $253.3\,\mathrm{mA\,h\,g^{-1}}$ for pristine sample. Crystalline lithium carbonate is not detected anymore by XRD after heat-treatment of the air-exposed sample, and the TGA shows a large reduction of the amount of impurities. The mass loss when the temperature exceeds $700\,^{\circ}\mathrm{C}$ nevertheless indicates that some impurities might still be present after regeneration. This result was also consistent with significant surface species still observed in XPS for regenerated sample despite the amount being reduced from the air-exposed sample. As a result, the voltage profile of the regenerated sample does not show a major improvement compared to the air-exposed sample indicating that air exposure is more detrimental to the Mn-substituted material than its Fe counterpart.

5.3.3 Electrolyte compatibility

Cathode electrolyte interphase (CEI) layer plays an essential role in determining the electrochemical performance of Li-ion batteries.[161,176] While a well-functioning interphase layer will passivate the electrolyte/electrode interphase and prevent further degradation of the material without hindering Li-ion diffusion, an unstable surface layer that fails to passivate the surface can result in the consequential breakdown of the active material. Despite its importance, detailed study on the formation and evolution of this interphase is

still limited, as it depends on a lot of factors such as the cathode material's crystal structure, chemical constitution, and operating voltage as well as the choice of electrolyte.[158]

Most previous studies on DRS cathodes were performed with standard carbonate-based electrolyte, which has been best engineered for conventional cathode materials operating at voltages lower than 4.5 V. Unfortunately, anionic redox cathode materials, including Li-excess layered oxides and DRS materials, rely on a high voltage cut-off (≈ 4.8 V) to achieve high capacity. Moreover, oxidized oxygen or released oxygen gas can further trigger reactions with the electrolyte and form a surface layer.[161] These reactions can be even more exacerbated by high surface area cathode materials such as nanoparticles.

Herein, we investigated two additional advanced electrolytes to understand the interphase formed by the electrolytes with disordered rock salt cathode materials. $Li_{1.3}Mn_{0.4}Nb_{0.3}O_2$ (Mn-DRS) material was used for this study in order to compare with another Mn-based Li-excess anionic redox material, $Li[Li_{0.144}Ni_{0.136}Co_{0.136}Mn_{0.544}]O_2$ (LR-NMC), which has been more widely studied. Micron-sized samples were used to reduce possible surface contamination, for instance, during the transfer to the glovebox, as it is more severe for higher-surface-area nanoparticles as discussed in the earlier section. The three different electrolyte systems studied are: 1) Baseline electrolyte: 1 M lithium hexafluorophosphate ($LiPF_6$) in a 3:7 volume mixture of ethylene carbonate (EC) and dimethyl carbonate (DMC); 2) LiDFOB eletrolyte: 1 M $LiPF_6$ in a 3:7 volume mixture of EC and DMC with 2 wt.% lithium difluoro(oxalate)borate (LiDFOB) as an additive; and 3) FEC electrolyte: 1 M $LiPF_6$ in a 1:4 volume mixture of fluoroethylene carbonate (FEC) and DMC.

Figure 5.18 presents the cycling stability of LR-NMC and Mn-DRS cells made with three different electrolytes, along with Nyquist plots of the impedance spectra at four different states: as assembled (bare), after 6 hours resting time (rest), after the first charge and after the first discharge. In half cells, the cause of capacity decay is

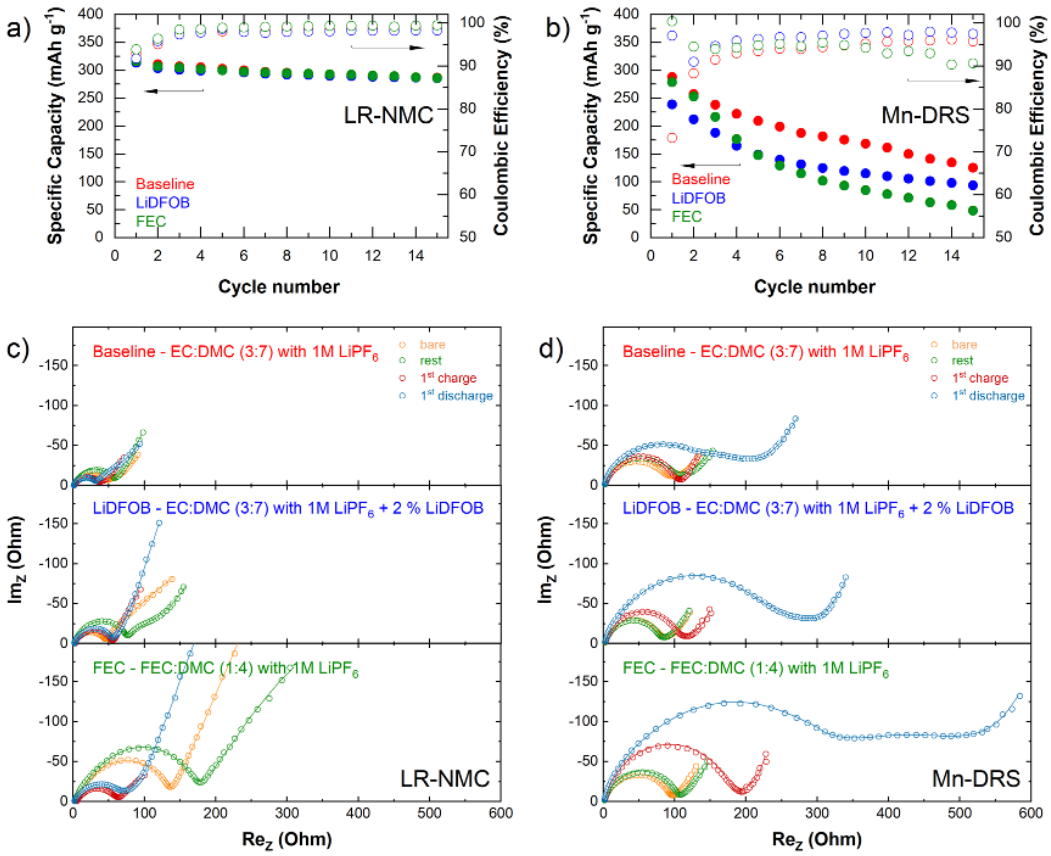

Figure 5.18: Cycling stability and Nyquist plots of a, c) $Li[Li_{0.144}Ni_{0.136}Co_{0.136}Mn_{0.544}]O_2$ and b, d) $Li_{1.3}Mn_{0.4}Nb_{0.3}O_2$ in the voltage range of 1.5 - 4.8 V vs. Li/Li^+ at room temperature with 3 different electrolytes. For each sample, the EIS spectra were acquired at 4 different steps: as assembled (bare), after a 6-hour resting time (rest), after the 1st charge, and after the 1st discharge. Equivalent circuits and fitting parameters are detailed in Figure 5.4 and Table 5.4.

attributed to both kinetic (impedance) and non-kinetic (electronic contact loss and cathode material degradation) factors. Therefore, the evolution of the cell impedance is not directly correlated with the capacity decay of the material - for example, LiDFOB and FEC electrolyte system in LR-NMC develop slightly larger impedance than the baseline but all present similar capacity decay. Nevertheless, electrochemical impedance spectroscopy provides important insights on where the resistance is mainly coming from. As shown, in terms of electrochemistry, the choice of electrolytes significantly impacts the cycling

stability of Mn-DRS contrary to what is observed for LR-NMC. Indeed, for Mn-DRS, the first discharge capacity for LiDFOB only reaches 240 $mA\,h\,g^{-1}$, whereas the baseline and FEC electrolytes are higher, around 288 $mA\,h\,g^{-1}$and 278 $mA\,h\,g^{-1}$, respectively. FEC electrolyte cell, nevertheless, exhibits a faster capacity decay than the two other cells, its discharge capacity being only 85 $mA\,h\,g^{-1}$ after only 10 cycles, compared to 168 $mA\,h\,g^{-1}$for the baseline and 115 $mA\,h\,g^{-1}$ for LiDFOB electrolyte. Even after the first few formation cycles, the coulombic efficiencies of all these cells are between 90 and 97% implying that severe side reactions continue to occur during cycling.

As detailed in the literature,[177] the high frequencies semicircle in EIS spectra can correspond to the resistance of the CEI layer,[178,179] and the contact resistance between the cathode composite and the current collector.[180] The intermediate frequencies semicircle is attributed to the charge transfer resistance between electrode and electrolyte[178,179] and the low frequencies tail, fitted by a Warburg element, corresponds to lithium ion diffusion in the electrode.[181–183] In the case of LR-NMC, consistent with the stable electrochemical performances, the impedance values remained in the same range for all the electrolytes. The charge transfer resistance contributions are reduced in charged and discharged state compared to the rest state, indicating that the resistance gets reduced after a stable CEI is formed. For Mn-DRS, the impedance of all three cells only slightly increases after a 6 hours resting time, which proves that the extent of the chemical reactions between the electrolytes and the cathode is limited. After the first charge, the impedance of the baseline cell stays stable, whereas it slightly increases for LiDFOB and is doubled for FEC electrolyte. Then, at the discharged state for all three cells, the charge transfer resistance increases drastically. Contrary to the baseline and LiDFOB electrolytes, where the initial impedance increases by two to three times, the FEC electrolyte cell shows an impedance more than 5 times higher than in the pristine state, suggesting the formation of an even thicker CEI layer.

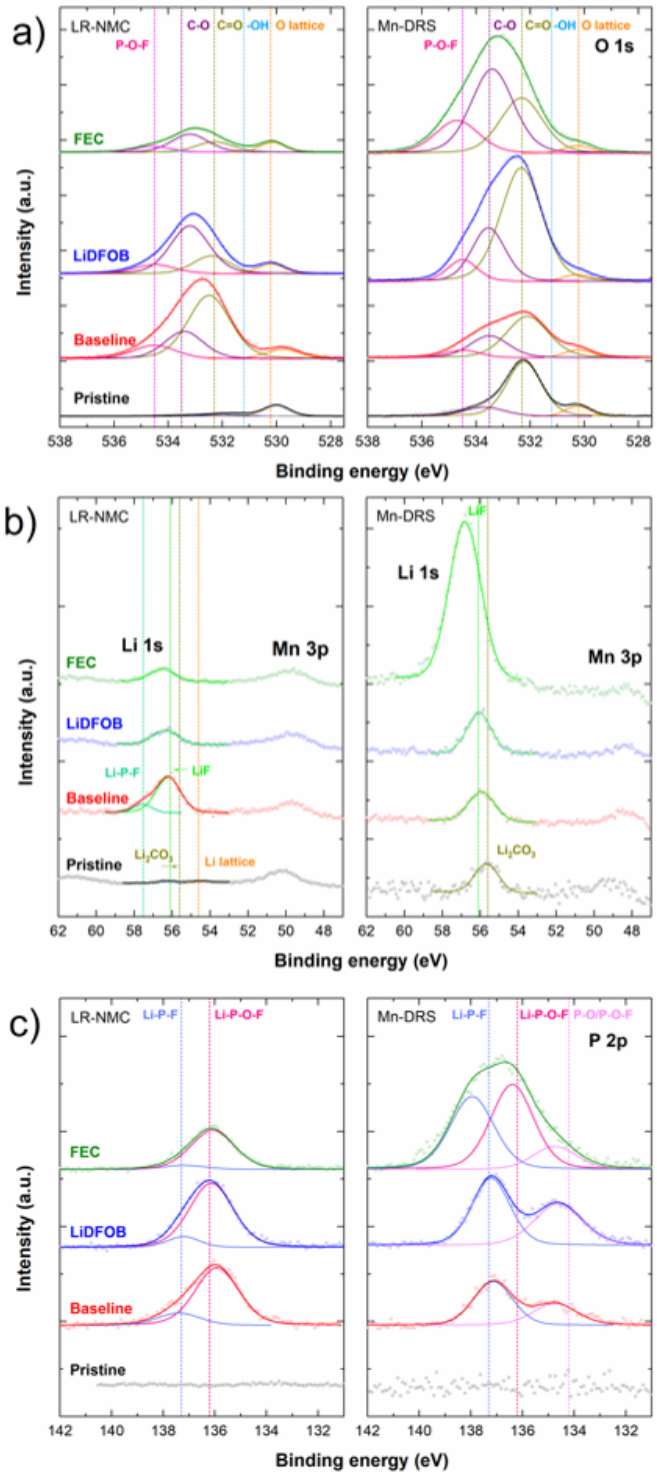

Figure 5.19: XPS spectra of the a) O 1s, b) Li 1s – Mn 3p, and c) P 2p region of $Li_{1.3}Mn_{0.4}Nb_{0.3}O_2$ and $Li[Li_{0.144}Ni_{0.136}Co_{0.136}Mn_{0.544}]O_2$ in the pristine state and after first discharge for the 3 electrolytes tested.

This passivation film usually protects the surface of the electrode particles by avoiding direct contact with the electrolyte during the highly oxidizing charging environment, however an excessive amount of CEI layer can drastically increase the cell impedance and affect the cycling efficiency and capacity retention. These results show that in contrast to other conventional cathode materials, Mn-DRS does not form a stable CEI layer with the electrolyte studied here.

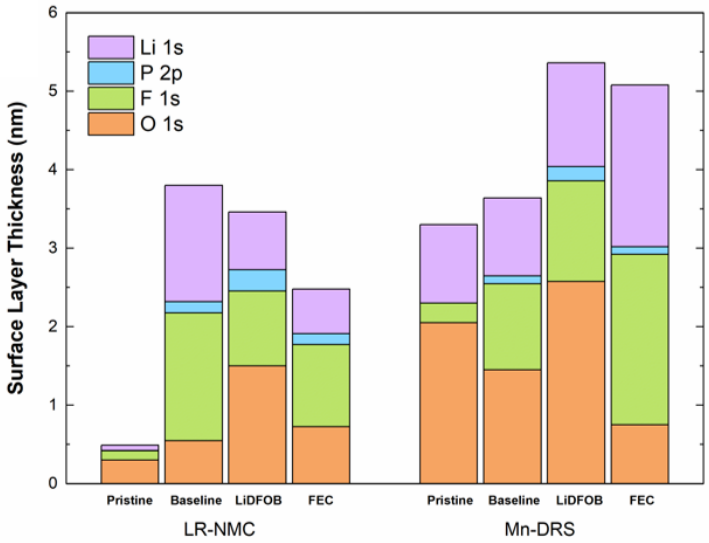

Figure 5.20: Surface layer thickness of $Li_{1.3}Mn_{0.4}Nb_{0.3}O_2$ and $Li[Li_{0.144}Ni_{0.136}Co_{0.136}Mn_{0.544}]O_2$ calculated from the XPS spectra with elemental contribution.

Along with the EIS study, XPS was carried out to understand the changes in chemical composition of the CEI layer with the choice of cathode materials and electrolytes. Figure 5.19a, b and c compares the O 1s, Li 1s – Mn 3p, and P 2p core regions of the pristine and cycled LR NMC and Mn-DRS electrodes, tested with three different electrolytes. Peak fits of each spectra are presented to indicate the dependence of specific CEI species on the electrolyte used, with approximate peak assignments detailed in Table 5.1. These assignments are based on a range of previous CEI studies on oxide cathodes.[184–186] The C-C carbon black peak at 284.8 eV was used to calibrate the LR-

NMC samples, while the Nb 3d peak associated with the Nb^{5+}environment was used for $Li_{1.3}Mn_{0.4}Nb_{0.3}O_2$. This second calibration method was selected due to differential charging effects that resulted in large relative binding energy shifts between $Li_{1.3}Mn_{0.4}Nb_{0.3}O_2$ and other cathode components (PVDF binder and carbon black). This effect can occur when measuring samples composed of mixed conducting and insulating materials,[187,188] and is more prevalent for the electronically insulating $Li_{1.3}Mn_{0.4}Nb_{0.3}O_2$ compound. For PVDF and carbon black, this effect results in over a 0.5 eV variation in their peak positions relative to the $Li_{1.3}Mn_{0.4}Nb_{0.3}O_2$ Nb 3d lattice peak (Figure 5.3). As detailed later, this effect can also cause shifts in the relative positions of insulating CEI species, including LiF.

Focusing first on the pristine compounds, there is a significant Li_2CO_3 layer on the surface of the Mn-DRS even before cycling, based on the strong peaks at 532.3 eV in the O 1s region and at 55.6 eV in the Li 1s region. As discussed in an earlier section, Li_2CO_3 surface impurity can come from residual precursors, or reactions between CO_2 in the atmosphere and the active cathode powder,[173] but the latter is more likely in Mn-DRS case, since the high-temperature heat-treatment (950 °C for 24 h) was conducted in Ar atmosphere during the synthesis. Despite the care taken to minimize atmospheric exposure during the experiments, high chemical sensitivity with ambient air for Mn-DRS leads to a surface layer more than 6 times as thick (3.3 nm) compared to the LR-NMC counterpart (0.49 nm). For both materials, this initial surface Li_2CO_3 layer breaks down at high state of charge (Figure 5.21), consistent with previously reported work.[171] Reductions of surface layer during charge are observed across all three electrolytes in Mn-DRS cathode as summarized in Figure 5.21a.

In the discharged state, new peaks arise as a thicker cathode-electrolyte-interphase develops for both cathode materials. In the O 1s core region, the single peak found at 530.2 eV is indexed to the lattice oxygen (TM-O). Higher energy peaks at $531 - 536$ eV are commonly attributed to the surface CEI species,[184–186] therefore, their relative intensities

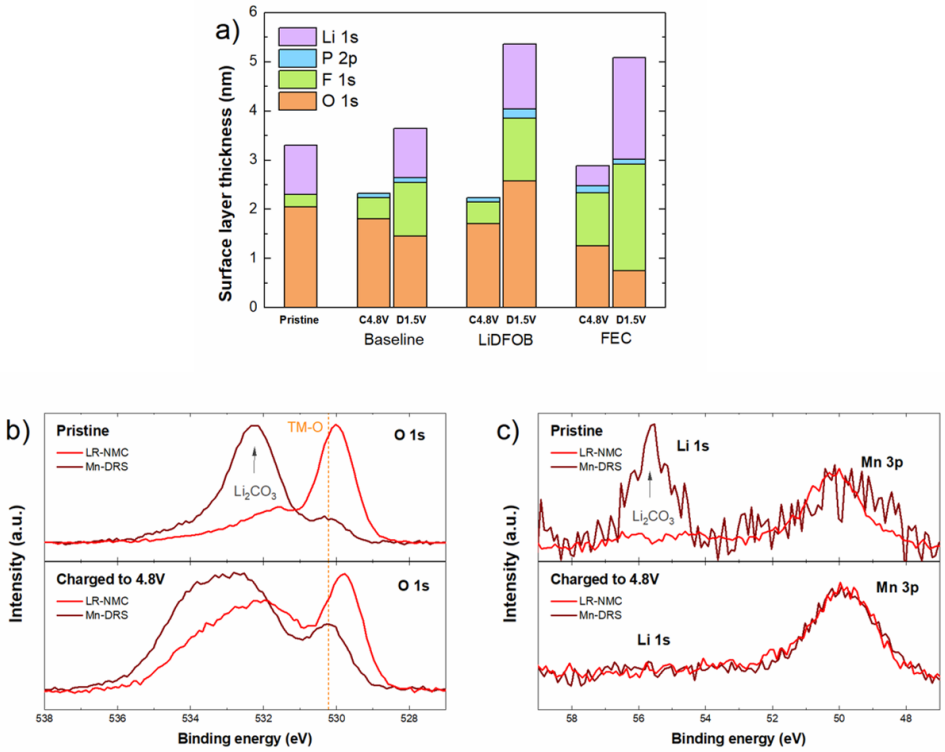

Figure 5.21: a) Surface layer thickness of Mn-DRS electrode in pristine, 4.8 V charged (C4.8 V), and 1.5 V discharged (D1.5 V) state with three electrolytes. Baseline represents EC:DMC (3:7) with 1M $LiPF_6$, LiDFOB represents EC:DMC (3:7) with 1M $LiPF_6$ + 2% LiDFOB, and FEC represents FEC:DMC (1:4) with 1M $LiPF_6$ (FEC) electrolyte systems. Comparison of XPS spectra of the b) O 1s region and c) Li 1s and Mn 3p region of morphology-controlled $Li_{1.3}Mn_{0.4}Nb_{0.3}O_2$ and Li-rich NMC in the pristine state and after the first charge with EC:DMC (3:7) with 1M $LiPF_6$.

against the lattice oxygen are a good indicator to estimate CEI thickness. In Figure 5.20, the elemental composition of the CEI (Li, P, F, and O) for each sample was normalized to the estimated CEI thickness. Although Mn-DRS initially starts with a thicker surface layer, a similar CEI thickness is found in LR-NMC by the end of the first cycle when using the baseline electrolyte. However, when LiDFOB additive or FEC:DMC co-solvent electrolytes are used, the two material systems show diverging trends in both CEI thickness and composition. In the case of LR-NMC, the overall intensities for CEI components get reduced compared to the baseline electrolyte, while the peak locations in O 1s, P 2p, and Li 1s remain mostly consistent. This indicates that the overall CEI thickness was reduced for

LiDFOB and FEC electrolytes without significant changes in their chemical composition.

On the other hand, for Mn-DRS material, CEI thickness increases from 3.64 nm for baseline to 5.36 nm for LiDFOB and 5.08 nm for FEC electrolytes. In both electrolytes, the O 1s signal is dominated by a broad peak at a higher binding energy than lattice TM-O (≈ 530.2 eV), which comprised of several oxygen-containing groups, such as C-O (≈ 533.5 eV), C=O (≈ 532.3 eV), O-H (≈ 531.2 eV), and P-O-F (≈ 534.4 eV) species. As the cycled electrodes were washed with DMC before XPS measurement, we assume that no Li-salt remained on the electrode. As a result, the relative amounts of detected Li, P, and F components can be correlated to the CEI species developed through the Li salt ($LiPF_6$) degradation in the electrolyte that leads to the formation of LiF and $Li_xPF_yO_z$ and other species.[184–186] As summarized in the elemental composition in Figure 5.20, Mn-DRS had consistently larger contributions of Li and F species for all 3 electrolytes than the LR-NMC cathode. The difference between these two systems becomes increasingly wider from baseline, LiDFOB, to FEC electrolyte, as both LiDFOB and FEC electrolytes show more salt decomposition in Mn-DRS, while it was found to be suppressed in LR-NMC.[159,189]

Particularly, in the FEC electrolyte with Mn-DRS, sharp peaks at ≈ 56.8 eV in the Li 1s region (Figure 5.19b) and at ≈ 686.6 eV in the F 1s region (Figure 5.22b) were detected compared to baseline or LiDFOB electrolytes. These peaks were attributed to LiF in spite of its ≈ 0.7 eV higher binding energy shift relative to the reference material in both the Li and F 1s spectra. This shift may be a result of the more insulating nature of LiF and the large quantity of these species found for the FEC electrolyte with Mn-DRS. Additionally, high intensity peaks associated with Li-P-F and Li-P-O-F species in the P 2p region were detected, which also arise from Li-salt decomposition. The pronounced increase in highly ionically resistive LiF at the CEI for the FEC electrolyte Mn-DRS electrode is consistent with the growth in impedance.[3] Although the LiDFOB electrolyte exhibited the thickest CEI of all six cycled electrodes based on our thickness estimation method, this is

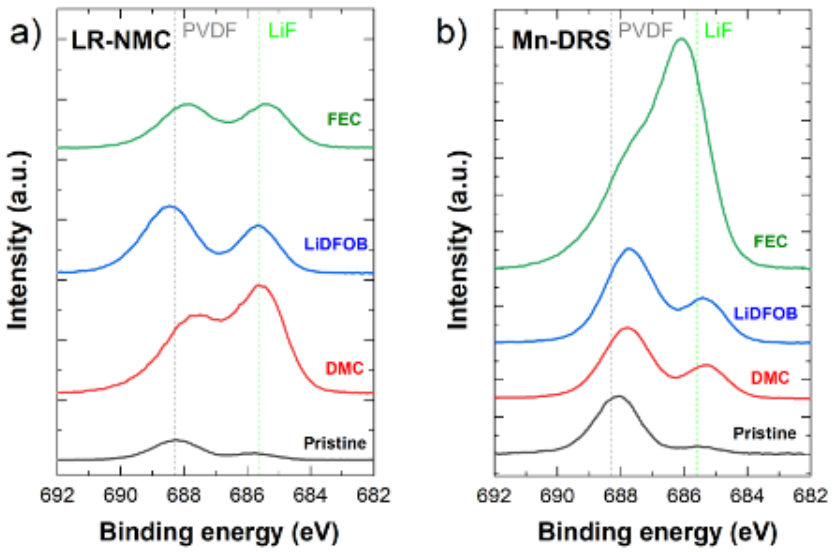

Figure 5.22: F 1s XPS spectra of a) $Li[Li_{0.144}Ni_{0.136}Co_{0.136}Mn_{0.544}]O_2$ and b) $Li_{1.3}Mn_{0.4}Nb_{0.3}O_2$ in the pristine state and after first discharge for the 3 electrolyte tested: EC:DMC (3:7) with 1M $LiPF_6$, EC:DMC (3:7) with 1M $LiPF_6$ + 2% LiDFOB, and FEC:DMC (1:4) with 1M $LiPF_6$.

likely a result of the high content of C=O and C-O species detected in the O 1s region. Indeed, less salt decomposition components were observed with the LiDFOB electrolyte, suggesting that solvent molecules are mainly involved in the CEI formation process. These results show that the choice of the electrolyte is crucial to enable long cycling stability of cation-disordered rock salt materials. Even compared with the similar Mn-based Li-excess anionic redox cathode material, DRS material forms distinct interphase species with the 3 electrolytes used for this study.

5.4 Conclusion

A systematic study of the solid-state synthesis of cation disordered rock salt materials was carried out, in which the influence of important synthesis parameters, such as precursor mixing, synthesis temperature, and precursor choice, on the final product was investigated. Three different morphology-controlled DRS materials, Li_3NbO_4, $Li_{1.3}Fe_{0.4}Nb_{0.3}O_2$, and

$Li_{1.3}Mn_{0.4}Nb_{0.3}O_2$, were synthesized at low temperature using nano-sized precursors. This method allowed to obtain particle sizes comprised between 150 nm and 1 µm, contrasting with the several micrometers-sized particles obtained with a standard high-temperature solid-state synthesis. Whereas the initial discharge capacity of the substituted samples reaches reported values in the literature and the capacity retention is improved, this class of material still suffers from poor cyclability. In order to investigate this issue, two possible limitations of this system were evaluated: surface contamination from air exposure and electrolyte stability. It appears that both $Li_{1.3}Fe_{0.4}Nb_{0.3}O_2$ and $Li_{1.3}Mn_{0.4}Nb_{0.3}O_2$ are highly sensitive to air exposure, as evidenced by TGA, XRD and XPS results. A heat-treatment at 500 °C allows the removal of most surface species, reducing the polarization of the cell and inducing the partial recovery of the lost capacity. Nevertheless, inert atmosphere storage after synthesis is still highly recommended for cation-disordered rock salt materials. For the electrolyte compatibility study, LiDFOB additives or FEC:DMC co-solvent electrolyte, although suitable for other oxygen redox material such as Li-excess NMC, was shown to lead to a thick CEI when used with Mn-substituted DRS cathode. This process occurs starting from the first discharge and results in a rapid increase of the cell impedance, hindering the cycling stability of the cathode. Therefore, evaluating the electrochemical compatibility of the electrolyte with the DRS cathode is critical for this new class of materials to enhance their electrochemical performances.

Chapter 5, in full, is currently under review as: H. Chung; Z. Lebens-Higgins; B. Sayahpour; C. Meija; A. Grenier; G.E. Kamm; Y. Li; R. Huang; L.F.J. Piper; K.W. Chapman; J. Doux; Y.S. Meng, "Experimental Considerations to Study Li-Excess Disordered Rock Salt Cathode Materials." The author was the primary investigator and author of this paper. All the experiment parts were performed by the author except electrochemical testing, XPS, and EIS.

Chapter 6

Summary and Future Works

With half a century of concerted efforts, it is widely acknowledged that the electrochemical performance of a cathode material is dictated not only by its crystal structure and composition but also its morphology and the interface it forms with other battery components. In-depth knowledge of the synthesis mechanism allows us to identify what are the most critical synthesis parameters that will influence the material electrochemistry, giving us the insight to design a better battery material. The focus of my study was to enhance the understanding of cathode nanoparticle synthesis. After a versatile synthesis platform that can control the morphology was developed, efforts were focused on understanding how each synthesis step affects the material's physical and chemical properties using advanced characterization tools.

In Chapter 3, a polyol method has been developed to synthesize high-performance, nano-size dispersed cathode materials including layered $LiNi_{0.4}Mn_{0.4}Co_{0.2}O_2$ (NMC), spinel $LiNi_{0.5}Mn_{1.5}O_4$ (LNMO), and olivine $LiCoPO_4$ (LCP), for Li-ion batteries. Polyol synthesis is a promising synthetic method that offers many advantages such as low cost, ease of use, and proven scalability for industrial applications, but the scope was so far mainly limited to simple metals or metal oxide compounds. This study showed that, when properly

designed, polyol synthesis can be applied to prepare a variety of cathode nanoparticles with controlled size distribution and superior surface structural stability.

Then, a comprehensive picture of how the polyol reaction progresses during each step of the synthesis was constructed using a combination of *in situ* and *ex situ* characterization, including STEM/EELS, soft XAS, and synchrotron XRD and PDF analysis. The results show that, for layered NMC, the reducing environment of the polyol medium yields the precipitate of core/shell structures with Ni-Co alloy nanocrystals surrounded by a Mn- and Li-embedded organic matrix. Then, the direct structural and chemical transformation was observed during the heat treatment that follows until the final cathode product with homogenous elemental distribution was confirmed.

As a follow up study, Chapter 4 explored in greater detail the origin of the enhanced electrochemical performance of polyol-synthesized cathode materials. Using atomic resolution images obtained from scanning transmission electron microscopy, highly coherent twin boundaries were identified in high concentrations for synthesized layered NMC. Detailed analysis revealed that a single atomic layer of rock salt-like phase forms at the twin boundary, which typically propagate radially across the particle in parallel direction to (104) plane. Such defects caused by twin boundaries are electrochemically inactive and possibly act as a framework during the charge and discharge process when layered oxide materials typically go through volume changes. Our hypothesis was supported by operando XRD results that show that polyol synthesized nanoparticles enriched with twin boundaries go through less internal shear stress during cycling compared to the reference NMC material. Repeated anisotropy changes in the reference material leads to pulverization after long-term cycling, which can be translated to severe capacity degradation.

Moving on to Chapter 5, I went beyond the traditional transition metal redox chemistry and investigated high capacity anionic redox materials. Cation-disordered rock salt (DRS) materials have recently received significant attention due to their additional

capacity, originating from anionic electrochemical activity, along with their low cost. However, their full assessment is still limited, as there are few studies reporting guidelines for their synthesis, their storage, and their electrochemical stability with the electrolyte. This work identified key synthesis parameters that influence both the crystal phase and the morphology of the DRS material. This knowledge helped enable low-temperature morphology-controlled synthesis of DRS using nano-sized precursors. Then, I have identified two additional important experimental considerations that are closely impacted by the particle morphology: the material storage condition and the choice of electrolyte during electrochemical testing. The results show that DRS material is extremely air-sensitive, so only inert air storage can preserve its original surface properties and electrochemical performances. As for the electrolyte, even when compared with similar Mn-based Li-excess layered cathode materials, DRS significantly accelerates salt decomposition in the electrolyte, leading to a thick layer of cathode-electrolyte-interface. The importance of electrolyte screening is emphasized before the full potential for DRS material can be realized.

Given the above-mentioned work, future work should be concentrated in finding the right application of the gained knowledge regarding the nanoparticle synthesis. Although the nanoparticle morphology generally improves the kinetics of the material by reducing the Li diffusion length, the dispersive nature may have lower tap density compared to the material that exists as micro-sized aggregates. Moreover, the increased surface sensitivity of nanoparticles due to large surface-to-volume ratio may lead to a larger extent of electrolyte decomposition or ambient air-induced contamination, depending on the material chemistry. This is also why it is extremely challenging to find a synthesis method that will yield completely dispersive cathode nanoparticles and, at the same time, give a comparable performance to that of conventional cathodes, which exist as micro-sized aggregates. However, as the synthesized cathode nanoparticles shown in this work show competitive

and even enhanced performance, the following applications can benefit from the inherent properties coming from large surface areas.

First of all, the synthesized well-crystallized cathode materials with dispersion of nanoparticles can be applied to enhance the performance of all-solid-state batteries (ASSBs). In energy storage technology, enhanced safety features are becoming increasingly important with the growing market in wearable electronics and electric vehicles. At the same time, higher energy and lower cost requirements of applications push the industry to higher Ni content cathode materials which are known to have lower thermal stability.[190] By removing flammable liquid electrolyte, ASSBs have improved safety features with the same cathode material and initiated a new paradigm shift in Li-ion batteries. However, one of the major challenges is to provide an intimate solid-to-solid contact between the electrodes and the electrolyte so that Li-ions can still intercalate during charge and discharge processes. With large surface areas to be contacted, cathode nanoparticles synthesized in this work can be utilized to help enable ASSB technology.

Secondly, detailed insights gained from the polyol synthesis method can be applied in the design of surface coating process. Previous studies demonstrated that a properly designed polyol synthesis process can uniformly coat both organic and inorganic materials.[44,54,191,192] Although these studies mainly used a wet method, where the core material was suspended in the polyol solution with dissolved precursor for the coating material, I would also like to propose a dry method that utilizes polyol-synthesized precursors. In this way, large amounts of coating precursors can be synthesized with one batch of the polyol process and reduce the overall amount of solvent required. Reduction of solvent amount is especially critical for industrial scale production, because large amount of solvent disposal is extremely costly and raises environmental concerns. While the large area dispersion of coating precursors is typically considered as challenging for dry coating process, polyol synthesis can yield extremely well-dispersed precipitate of 1-2 nm in size with attached

organics (if desired) that can help attaching to the core material. This provides the possibility of substituting the current expensive coating process, for instance in a concentration gradient of NMC cathode[193] or lithium niobate coating commonly applied for $LiCoO_2$ in ASSBs.[194]

Lastly, insights gained from this work can be applied in the strategy for the incorporating dopants. Several computational studies predict that significant enhancement of electrochemistry can be achieved when small amounts of a dopant are incorporated into the cathode material bulk structure.[20] However, doping studies are extremely challenging experimentally, because many of the precursors that can be used as dopants are metal oxides with extremely high melting points (above 1000 °C), well beyond the thermal stability temperature of cathode materials. Trying to mix separate elements is challenging at lower temperatures and often yields impurities with elemental segregation. However, as demonstrated in Chapter 5, the usage of nano-sized precursors can dramatically reduce the synthesis temperature, promote a fast and homogeneous reaction, and mitigate the elemental segregation of the final product. Thus, the results suggest that nano sized precursors made via the polyol process may enable doping materials and dramatically improve their electrochemical properties as computations have predicted.

Bibliography

[1] M. Li, J. Lu, Z. Chen and K. Amine, *Advanced Materials*, 2018, **30**, 1–24.

[2] B. Xu, D. Qian, Z. Wang and Y. S. Meng, *Materials Science and Engineering R: Reports*, 2012, **73**, 51–65.

[3] M. Gauthier, T. J. Carney, A. Grimaud, L. Giordano, N. Pour, H.-h. Chang, D. P. Fenning, S. F. Lux, O. Paschos, C. Bauer, F. Maglia, S. Lupart, P. Lamp and Y. Shao-horn, *The journal of physical chemistry letters*, 2015, **6**, 4653–4672.

[4] Q. Li, J. Chen, L. Fan, X. Kong and Y. Lu, *Green Energy and Environment*, 2016, **1**, 18–42.

[5] C. R. Birkl, M. R. Roberts, E. McTurk, P. G. Bruce and D. A. Howey, *Journal of Power Sources*, 2017, **341**, 373–386.

[6] R. Hausbrand, G. Cherkashinin, H. Ehrenberg, M. Gröting, K. Albe, C. Hess and W. Jaegermann, *Materials Science and Engineering B*, 2015, **192**, 3–25.

[7] C. Julien, A. Mauger, K. Zaghib and H. Groult, *Inorganics*, 2014, **2**, 132–154.

[8] M. S. Whittingham, *Science*, 1976, **192**, 1126–1127.

[9] M. S. Whittingham, *Journal of The Electrochemical Society*, 1976, **123**, 315.

[10] A. Manthiram, *Nature Communications*, 2020, **11**, 1–9.

[11] T. Kim, W. Song, D. Y. Son, L. K. Ono and Y. Qi, *Journal of Materials Chemistry A*, 2019, **7**, 2942–2964.

[12] F. Lin, I. M. Markus, D. Nordlund, T. C. Weng, M. D. Asta, H. L. Xin and M. M. Doeff, *Nature communications*, 2014, **5**, 3529.

[13] A. Manthiram, K. Chemelewski and E. S. Lee, *Energy and Environmental Science*, 2014, **7**, 1339–1350.

[14] X. L. Xu, S. X. Deng, H. Wang, J. B. Liu and H. Yan, *Nano-Micro Letters*, 2017, **9**, 1–19.

[15] S. Upreti, N. A. Chernova, J. Xiao, J. K. Miller, O. V. Yakubovich, J. Cabana, C. P. Grey, V. L. Chevrier, G. Ceder, J. L. Musfeldt and M. S. Whittingham, *Chemistry of Materials*, 2012, **24**, 166–173.

[16] W. J. Zhang, *Journal of Power Sources*, 2011, **196**, 2962–2970.

[17] J. Yu and H. Zhou, *The Journal of Physical Chemistry Letters*, 2013, **4**, 1268–1280.

[18] H. Pan, S. Zhang, J. Chen, M. Gao, Y. Liu, T. Zhu and Y. Jiang, *Molecular Systems Design and Engineering*, 2018, **3**, 748–803.

[19] G. Assat, D. Foix, C. Delacourt, A. Iadecola, R. Dedryvère and J. M. Tarascon, *Nature Communications*, 2017, **8**, year.

[20] T. A. Wynn, C. Fang, M. Zhang, H. Liu, D. M. Davies, X. Wang, D. Lau, J. Z. Lee, B. Y. Huang, K. Z. Fung, C. T. Ni and Y. S. Meng, *Journal of Materials Chemistry A*, 2018, **6**, 24651–24659.

[21] S. Guo, H. Yu, P. Liu, X. Liu, D. Li, M. Chen, M. Ishida and H. Zhou, *Journal of Materials Chemistry A*, 2014, **2**, 4422–4428.

[22] H. Guo, Z. Wei, K. Jia, B. Qiu, C. Yin, F. Meng, Q. Zhang, L. Gu, S. Han, Y. Liu, H. Zhao, W. Jiang, H. Cui, Y. Xia and Z. Liu, *Energy Storage Materials*, 2019, **16**, 220–227.

[23] N. Yabuuchi, M. Takeuchi, M. Nakayama, H. Shiiba, M. Ogawa, K. Nakayama, T. Ohta, D. Endo, T. Ozaki, T. Inamasu, K. Sato and S. Komaba, *Proceedings of the National Academy of Sciences*, 2015, **112**, 7650–7655.

[24] R. J. Clément, Z. Lun and G. Ceder, *Energy & Environmental Science*, 2020, **13**, 345–373.

[25] E. S. Ameh, *International Journal of Advanced Manufacturing Technology*, 2019, **105**, 3289–3302.

[26] K. Stahl, 2008.

[27] X. Wang, S. Tan, X. Q. Yang and E. Hu, *Chinese Physics B*, 2020, **29**, 028802.

[28] M. Sardela, *Practical materials characterization*, 2014, pp. 1–237.

[29] K. W. Chapman, *MRS Bulletin*, 2016, **41**, 231–238.

[30] B. J. Inkson, *Materials Characterization Using Nondestructive Evaluation (NDE) Methods*, Elsevier Ltd, 2016, pp. 17–43.

[31] C. Liu, Z. G. Neale and G. Cao, *Materials Today*, 2016, **19**, 109–123.

[32] S. J. Cho, M. J. Uddin and P. Alaboina, *Review of Nanotechnology for Cathode Materials in Batteries*, Elsevier Inc., 2017, pp. 83–129.

[33] M. Armand and J.-M. Tarascon, *Nature*, 2008, **451**, 652–657.

[34] B. Dunn, H. Kamath and J.-m. Tarascon, *Science*, 2011, **334**, 928–935.

[35] R. J. Brodd, M. M. Doeff and J. Goodenough, *Batteries for Sustainability: Selected Entries from the Encyclopedia of Sustainability Science and Technology*, 2013, pp. 1–504.

[36] H. Deshazer, F. L. Mantia, C. Wessells, R. Huggins and Y. Cui, *Journal of The Electrochemical Society*, 2011, **158**, 1079–1082.

[37] Z. Zhang, S. Zhu, J. Huang and C. Yan, *Ionics*, 2016, **22**, 621–627.

[38] M. Zhang, H. Liu, Z. Liu, C. Fang and Y. S. Meng, *ACS Applied Materials & Interfaces*, 2018, 3369–3376.

[39] R. Zhao, Z. Yang, J. Liang, D. Lu, C. Liang, X. Guan, A. Gao and H. Chen, *Journal of Alloys and Compounds*, 2016, 318–325.

[40] Y. Shi, M. Zhang, C. Fang and Y. S. Meng, *Journal of Power Sources*, 2018, **394**, 114–121.

[41] J. Zheng, M. Gu, A. Genc, J. Xiao, P. Xu, X. Chen, Z. Zhu, W. Zhao, L. Pullan, C. Wang and J. G. Zhang, *Nano Letters*, 2014, **14**, 2628–2635.

[42] X. Cao, Y. Zhao, L. Zhu, L. Xie, X. Cao, S. Xiong and C. Wang, *International Journal of Electrochemical Science*, 2016, **11**, 5267–5278.

[43] F. Fievet, J. P. Lagier, B. Blin, B. Beaudoin and M. Figlarz, *Solid State Ionics*, 1989, **32-33**, 198–205.

[44] F. Fievet, S. Ammar-Merah, R. Brayner, F. Chau, M. Giraud, F. Mammeri, J. Peron, J. Y. Piquemal, L. Sicard and G. Viau, *Chemical Society Reviews*, 2018, **47**, 5187–5233.

[45] A. R. Tao, S. Habas and P. Yang, *Small*, 2008, **4**, 310–325.

[46] P. J. Chupas, K. W. Chapman, C. Kurtz, J. C. Hanson, P. L. Lee and C. P. Grey, *Journal of Applied Crystallography*, 2008, **41**, 822–824.

[47] B. H. Toby and R. B. Von Dreele, *Journal of Applied Crystallography*, 2013, **46**, 544–549.

[48] P. Juhás, T. Davis, C. L. Farrow and S. J. L. Billinge, *Journal of Applied Crystallography*, 2013, **46**, 560–566.

[49] C. L. Farrow, P. Juhas, J. W. Liu, D. Bryndin, E. S. Božin, J. Bloch, T. Proffen and S. J. L. Billinge, *Journal of physics. Condensed matter : an Institute of Physics journal*, 2007, **19**, 335219.

[50] T. Roisnel and J. Rodriguez-Carvajal, *EPDIC 7: Proceedings of the Seventh European Powder Diffraction Conference, Materials Science Forum*, 2001, 118–123.

[51] J. Rodríguez-Carvajal, *Physica B: Physics of Condensed Matter*, 1993, **192**, 55–69.

[52] R. Qiao, Q. Li, Z. Zhuo, S. Sallis, O. Fuchs, M. Blum, L. Weinhardt, C. Heske, J. Pepper, M. Jones, A. Brown, A. Spucces, K. Chow, B. Smith, P.-A. Glans, Y. Chen, S. Yan, F. Pan, L. F. J. Piper, J. Denlinger, J. Guo, Z. Hussain, Y.-D. Chuang and W. Yang, *Review of Scientific Instruments*, 2017, **88**, 033106.

[53] Q. Li, R. Qiao, L. A. Wray, J. Chen, Z. Zhuo, Y. Chen, S. Yan, F. Pan, Z. Hussain and W. Yang, *Journal of Physics D: Applied Physics*, 2016, **49**, 413003.

[54] H. Dong, Y. C. Chen and C. Feldmann, *Green Chemistry*, 2015, **17**, 4107–4132.

[55] K. Imamoto and M. Arai, *Materials and Structures*, 2008, **41**, 323–333.

[56] D. G. Capco and Y. Chen, *Nanomaterial impacts on Cell Biology and Medicine*, 2014.

[57] D. Zhang and R. Luo, *Construction and Building Materials*, 2018, **175**, 653–663.

[58] N. Tran, L. Croguennec, C. Jordy, P. Biensan and C. Delmas, *Solid State Ionics*, 2005, **176**, 1539–1547.

[59] J. C. Arrebola, A. Caballero, M. Cruz, L. Hernán, J. Morales and E. R. Castellón, *Advanced Functional Materials*, 2006, **16**, 1904–1912.

[60] H. Liu, X. Zhang, X. He, A. Senyshyn, A. Wilken, D. Zhou, O. Fromm, P. Niehoff, B. Yan, J. Li, M. Muehlbauer, J. Wang, G. Schumacher, E. Paillard, M. Winter and J. Li, *Journal of The Electrochemical Society*, 2018, **165**, A1886–A1896.

[61] L. Wang, H. Li and X. Huang, *Progress in Natural Science: Materials International*, 2012, **22**, 207–212.

[62] J. Song, D. W. Shin, Y. Lu, C. D. Amos, A. Manthiram and J. B. Goodenough, *Chemistry of Materials*, 2012, **24**, 3101–3109.

[63] J. Yang, X. Han, X. Zhang, F. Cheng and J. Chen, *Nano Research*, 2013, **6**, 679–687.

[64] A. Nytén and J. O. Thomas, *Solid State Ionics*, 2006, **177**, 1327–1330.

[65] N. N. Bramnik, K. G. Bramnik, C. Baehtz and H. Ehrenberg, *Journal of Power Sources*, 2005, **145**, 74–81.

[66] J. Ludwig and T. Nilges, *Journal of Power Sources*, 2018, **382**, 101–115.

[67] J. Mayer, L. A. Giannuzzi, T. Kamino and J. Michael, *MRS Bulletin*, 2007, **32**, 400–407.

[68] S. Wolff-Goodrich, F. Lin, I. M. Markus, D. Nordlund, H. L. Xin, M. Asta and M. M. Doeff, *Physical Chemistry Chemical Physics*, 2015, **17**, 21778–21781.

[69] J. Zheng, P. Yan, J. Zhang, M. H. Engelhard, Z. Zhu, B. J. Polzin, S. Trask, J. Xiao, C. Wang and J. Zhang, *Nano Research*, 2017, **10**, 4221–4231.

[70] M. Lin, L. Ben, Y. Sun, H. Wang, Z. Yang, L. Gu, X. Yu, X. Q. Yang, H. Zhao, R. Yu, M. Armand and X. Huang, *Chemistry of Materials*, 2015, **27**, 292–303.

[71] L. Ben, H. Yu, B. Chen, Y. Chen, Y. Gong, X. Yang, L. Gu and X. Huang, *ACS Applied Materials and Interfaces*, 2017, **9**, 35463–35475.

[72] R. Huang and Y. Ikuhara, *Current Opinion in Solid State and Materials Science*, 2012, **16**, 31–38.

[73] M. Gu, I. Belharouak, A. Genc, Z. Wang, D. Wang, K. Amine, F. Gao, G. Zhou, S. Thevuthasan, D. R. Baer, J. G. Zhang, N. D. Browning, J. Liu and C. Wang, *Nano Letters*, 2012, **12**, 5186–5191.

[74] R. A. Armstrong, M. Holzapfel, P. Novak, C. S. Johnson, S.-H. Kang, M. M. Thackeray and P. G. Bruce, *Journal of the American Chemical Society*, 2006, **128**, 8694–8698.

[75] W. H. Ryu, S. J. Lim, W. K. Kim and H. Kwon, *Journal of Power Sources*, 2014, **257**, 186–191.

[76] J. Xiao, X. Chen, P. V. Sushko, M. L. Sushko, L. Kovarik, J. Feng, Z. Deng, J. Zheng, G. L. Graff, Z. Nie, D. Choi, J. Liu, J. G. Zhang and M. S. Whittingham, *Advanced Materials*, 2012, **24**, 2109–2116.

[77] Q. Wu, X. Zhang, S. Sun, N. Wan, D. Pan, Y. Bai, H. Zhu, Y. S. Hu and S. Dai, *Nanoscale*, 2015, **7**, 15609–15617.

[78] N. N. Bramnik, K. Nikolowski, G. Baehtz, K. G. Bramnik and H. Ehrenberg, *Chemistry of Materials*, 2007, **19**, 908–915.

[79] K. J. Kreder, G. Assat and A. Manthiram, *Chemistry of Materials*, 2015, **27**, 5543–5549.

[80] C. Julien, A. Mauger, K. Zaghib and H. Groult, *Materials (Basel)*, 2016, **9**, 595.

[81] D.-H. Kim and J. Kim, *Electrochemical and Solid-State Letters*, 2006, **9**, 439–442.

[82] Z. Chen, D. Chao, J. Liu, M. Copley, J. Lin, Z. Shen, G. T. Kim and S. Passerini, *Journal of Materials Chemistry A*, 2017, **5**, 15669–15675.

[83] H. Yu, Y. Qian, M. Otani, D. Tang, S. Guo, Y. Zhu and H. Zhou, *Energy and Environmental Science*, 2014, **7**, 1068.

[84] C. Ban, Z. Li, Z. Wu, M. J. Kirkham, L. Chen, Y. S. Jung, E. A. Payzant, Y. Yan, M. S. Whittingham and A. C. Dillon, *Advanced Energy Materials*, 2011, **1**, 58–62.

[85] Z. Chen, G. T. Kim, D. Chao, N. Loeffler, M. Copley, J. Lin, Z. Shen and S. Passerini, *Journal of Power Sources*, 2017, **372**, 180–187.

[86] W. S. Yoon, M. Balasubramanian, K. Y. Chung, X. Q. Yang, J. McBreen, C. P. Grey and D. A. Fischer, *Journal of the American Chemical Society*, 2005, **127**, 17479–17487.

[87] I. A. Shkrob, J. A. Gilbert, P. J. Phillips, R. Klie, R. T. Haasch, J. Bareño and D. P. Abraham, *Journal of The Electrochemical Society*, 2017, **164**, A1489–A1498.

[88] X. Jiang, Y. Sha, R. Cai and Z. Shao, *Journal of Materials Chemistry A*, 2015, **3**, 10536–10544.

[89] S. Helveg, C. Lopez-Cartes, J. Sehested, P. L. Hansen, B. S. Clausen, J. R. Rostrup-nielsen, F. Abild-pedersen and J. Norskov, *Nature*, 2004, **427**, 426–429.

[90] K. R. Yoon, J. W. Ko, D.-Y. Youn, C. B. Park and I.-D. Kim, *Green Chemistry*, 2016, 944–950.

[91] M. K. Singh, A. Agarwal, R. Gopal, R. K. Swarnkar and R. K. Kotnala, *Journal of Materials Chemistry*, 2011, **21**, 11074–11079.

[92] J. Zhu, S. Wei, Y. Li, S. Pallavkar, H. Lin, N. Haldolaarachchige, Z. Luo, D. P. Young and Z. Guo, *Journal of Materials Chemistry*, 2011, **21**, 16239–16246.

[93] Q. Yao, X. Chen and Z.-H. Lu, *Energy and Environment Focus*, 2014, **3**, 236–245.

[94] H. Shang, K. Pan, L. Zhang, B. Zhang and X. Xiang, *Nanomaterials*, 2016, **6**, 103.

[95] E. A. Owen and D. M. Jones, *Proceedings of the Physical Society, London*, 1954, **67**, 456–466.

[96] W. Li, O. J. Borkiewicz, M. Saubanère, M. L. Doublet, D. Flahaut, P. J. Chupas, K. W. Chapman and D. Dambournet, *Journal of Physical Chemistry C*, 2018, **122**, 23861–23866.

[97] C. Petit, Z. L. Wang and M. P. Pileni, *Journal of Physical Chemistry B*, 2005, **109**, 15309–15316.

[98] J. Rouquette, J. Haines, G. Fraysse, A. Al-Zein, V. Bornarnd, M. Pintard, P. Papet, S. Hull and F. A. Gorelli, *Inorganic Chemistry*, 2008, **47**, 9898–9904.

[99] I. K. Suh, H. Ohta and Y. Waseda, *Journal of Materials Science*, 1988, **23**, 757–760.

[100] J. Bandyopadhyay and K. P. Gupta, *Cryogenics*, 1977, **17**, 345–347.

[101] A. Taylor and R. W. Floyd, *Acta Crystallographica*, 1950, **3**, 285–289.

[102] A. Morozkin, *Intermetallics*, 2012, **25**, 136–138.

[103] E. A. Owen and D. M. Jones, *Proceedings of the Physical Society, London*, 1954, **67**, 456–466.

[104] L. J. Hofer and W. C. Peebles, *Journal of the American Chemical Society*, 1947, **69**, 893–899.

[105] E. F. Bertaut, D. Tran Qui, P. Burlet, P. Burlet, M. Thomas, J. M. Moreau and IUCr, *Acta Crystallographica*, 1974, **B30**, 2234–2236.

[106] C. Luna, M. d. P. Morales, C. J. Serna and M. Vázquez, *Nanotechnology*, 2003, **14**, 268–272.

[107] R. Sanz, C. Luna, M. Hernández-Vélez, M. Vázquez, D. López and C. Mijangos, *Nanotechnology*, 2005, **16**, 278–281.

[108] T. J. Regan, H. Ohldag, C. Stamm, F. Nolting, J. Lüning, J. Stöhr and R. L. White, *Physical Review B*, 2001, **64**, 214422.

[109] L. Hu, H. Zhong, X. Zheng, Y. Huang, P. Zhang and Q. Chen, *Scientific Reports*, 2012, **2**, 986.

[110] M. Augustin, D. Fenske, I. Bardenhagen, A. Westphal, M. Knipper, T. Plaggenborg, J. Kolny-Olesiak and J. Parisi, *Beilstein Journal of Nanotechnology*, 2015, **6**, 47–59.

[111] D. Zhang, C. Jin, Z. Y. Li, Z. Zhang and J. Li, *Science Bulletin*, 2017, **62**, 775–778.

[112] D. H. Ha, L. M. Moreau, S. Honrao, R. G. Hennig and R. D. Robinson, *Journal of Physical Chemistry C*, 2013, **117**, 14303–14312.

[113] A. Grenier, H. Liu, Z. W. Lebens-Higgins, L. F. J. Piper, O. J. Borkiewicz, K. M. Wiaderek, P. J. Chupas and K. W. Chapman, *Chemistry of Materials*, 2017, **29**, 7345–7352.

[114] R. Wang, X. Yu, J. Bai, H. Li, X. Huang, L. Chen and X. Yang, *Journal of Power Sources*, 2012, **218**, 113–118.

[115] E. A. Gulbransen and K. F. Andrew, *Journal of The Electrochemical Society*, 1951, **98**, 241–251.

[116] J. G. Railsback, A. C. Johnston-Peck, J. Wang and J. B. Tracy, *ACS Nano*, 2010, **4**, 1913–1920.

[117] J. Zhu and G. Chen, *Journal of Materials Chemistry A*, 2019, **7**, 5463–5474.

[118] Y. Liu, X. J. Lin, Y. G. Sun, Y. S. Xu, B. B. Chang, C. T. Liu, A. M. Cao and L. J. Wan, *Precise Surface Engineering of Cathode Materials for Improved Stability of Lithium-Ion Batteries*, 2019.

[119] Y. Zhang, L. Tao, C. Xie, D. Wang, Y. Zou, R. Chen, Y. Wang, C. Jia and S. Wang, *Advanced Materials*, 2020, **32**, 1905923.

[120] Q. D. Truong, M. K. Devaraju, Y. Sasaki, H. Hyodo, T. Tomai and I. Honma, *Chemistry of Materials*, 2014, **26**, 2770–2773.

[121] B. Qiu, M. Zhang, L. Wu, J. Wang, Y. Xia, D. Qian, H. Liu, S. Hy, Y. Chen, K. An, Y. Zhu, Z. Liu and Y. S. Meng, *Nature Communications*, 2016, **7**, 12108.

[122] L. Hong, K. Yang and M. Tang, *npj Computational Materials*, 2019, **5**, 118.

[123] K. Yang and M. Tang, *Journal of Materials Chemistry A*, 2020, **8**, 3060–3070.

[124] A. P. Rooney, Z. Li, W. Zhao, A. Gholinia, A. Kozikov, G. Auton, F. Ding, R. V. Gorbachev, R. J. Young and S. J. Haigh, *Nature Communications*, 2018, **9**, 3597.

[125] H. Chung, A. Grenier, R. Huang, X. Wang, Z. Lebens-Higgins, J. M. Doux, S. Sallis, C. Song, P. Ercius, K. Chapman, L. F. Piper, H. M. Cho, M. Zhang and Y. S. Meng, *Nano Research*, 2019, **12**, 2238–2249.

[126] N. V. Faenza, L. Bruce, Z. W. Lebens-Higgins, I. Plitz, N. Pereira, L. F. Piper and G. G. Amatucci, *Journal of the Electrochemical Society*, 2017, **164**, A3727–A3741.

[127] H. Liu, P. K. Allan, O. J. Borkiewicz, C. Kurtz, C. P. Grey, K. W. Chapman and P. J. Chupas, *Journal of Applied Crystallography*, 2016, **49**, 1665–1673.

[128] H. Liu, Z. Li, A. Grenier, G. E. Kamm, L. Yin, G. S. Mattei, M. R. Cosby, P. G. Khalifah, P. J. Chupas and K. W. Chapman, *Journal of Applied Crystallography*, 2020, **53**, 133–139.

[129] P. W. Stephens, *Journal of Applied Crystallography*, 1999, **32**, 281–289.

[130] J. P. Perdew and W. Yue, *Physical Review B*, 1986, **33**, 8800–8802.

[131] G. Kresse and D. Joubert, *Physical Review B - Condensed Matter and Materials Physics*, 1999, **59**, 1758–1775.

[132] G. Kresse and J. Hafner, *Physical Review B*, 1994, **49**, 14251–14269.

[133] G. Kresse and J. Furthmüller, *Computational Materials Science*, 1996, **6**, 15–50.

[134] S. Dudarev, G. Botton, S. Y. Savrasov, C. Humphreys and A. Sutton, *Physical Review B - Condensed Matter and Materials Physics*, 1998, **57**, 1505–1509.

[135] R. Tran, Z. Xu, B. Radhakrishnan, D. Winston, W. Sun, K. A. Persson and S. P. Ong, *Scientific Data*, 2016, **3**, 160080.

[136] H. Moriwake, A. Kuwabara, C. A. Fisher, R. Huang, T. Hitosugi, Y. H. Ikuhara, H. Oki and Y. Ikuhara, *Advanced Materials*, 2013, **25**, 618–622.

[137] P. Niehoff and M. Winter, *Langmuir*, 2013, **29**, 15813–15821.

[138] D. Kramer and G. Ceder, *Chemistry of Materials*, 2009, **21**, 3799–3809.

[139] G. Wulff, *Zeitschrift für Kristallographie - Crystalline Materials*, 1901, **34**, 449–530.

[140] L. D. Marks, *Philosophical Magazine A*, 1984, **49**, 81–93.

[141] A. Howie and L. D. Marks, *Philosophical Magazine A*, 1984, **49**, 95–109.

[142] W. Li, H. Y. Asl, Q. Xie and A. Manthiram, *Journal of the American Chemical Society*, 2019, **141**, 5097–5101.

[143] J. H. Kim, S. J. Kim, T. Yuk, J. Kim, C. S. Yoon and Y. K. Sun, *ACS Energy Letters*, 2018, **3**, 3002–3007.

[144] S. Hy, H. Liu, M. Zhang, D. Qian, B. J. Hwang and Y. S. Meng, *Energy and Environmental Science*, 2016, **9**, 1931–1954.

[145] P. K. Nayak, E. M. Erickson, F. Schipper, T. R. Penki, N. Munichandraiah, P. Adelhelm, H. Sclar, F. Amalraj, B. Markovsky and D. Aurbach, *Advanced Energy Materials*, 2017, **8**, 1702397.

[146] J. Lee, A. Urban, X. Li, D. Su, G. Hautier and G. Ceder, *Science*, 2014, **343**, 519–522.

[147] D. A. Kitchaev, Z. Lun, W. D. Richards, H. Ji, R. J. Clément, M. Balasubramanian, D. H. Kwon, K. Dai, J. K. Papp, T. Lei, B. D. McCloskey, W. Yang, J. Lee and G. Ceder, *Energy and Environmental Science*, 2018, **11**, 2159–2171.

[148] N. Yabuuchi, *Chemistry Letters*, 2016, **46**, 412–422.

[149] A. Urban, J. Lee and G. Ceder, *Advanced Energy Materials*, 2014, **4**, 1400478.

[150] J. Lee, J. K. Papp, R. J. Clément, S. Sallis, D. H. Kwon, T. Shi, W. Yang, B. D. McCloskey and G. Ceder, *Nature Communications*, 2017, **8**, 1–10.

[151] N. Yabuuchi, M. Takeuchi, S. Komaba, S. Ichikawa, T. Ozaki and T. Inamasu, *Chemical Communications*, 2016, **52**, 2051–2054.

[152] R. Wang, X. Li, L. Liu, J. Lee, D.-h. Seo, S.-h. Bo, A. Urban and G. Ceder, *Electrochemistry Communications*, 2015, **60**, 70–73.

[153] X. Fan, Q. Qin, D. Liu, A. Dou, M. Su, Y. Liu and J. Pan, *Journal of Alloys and Compounds*, 2019, **797**, 961–969.

[154] R. Chen, S. Ren, M. Knapp, D. Wang, R. Witter, M. Fichtner and H. Hahn, *Advanced Energy Materials*, 2015, **5**, 1401814.

[155] M. Freire, N. V. Kosova, C. Jordy, D. Chateigner, O. I. Lebedev, A. Maignan and V. Pralong, *Nature Materials*, 2015, **15**, 173–177.

[156] J. Lee, D. A. Kitchaev, D.-H. Kwon, C.-W. Lee, J. K. Papp, Y.-S. Liu, Z. Lun, R. J. Clément, T. Shi, B. D. McCloskey, J. Guo, M. Balasubramanian and G. Ceder, *Nature*, 2018, **556**, 185–190.

[157] E. N. Lysenko, A. P. Surzhikov, E. V. Nikolaev and V. A. Vlasov, *Journal of Thermal Analysis and Calorimetry*, 2018, **134**, 81–87.

[158] H. Zhao, X. Yu, J. Li, B. Li, H. Shao, L. Li and Y. Deng, *Journal of Materials Chemistry A*, 2019, **7**, 8700–8722.

[159] J. Cha, J.-g. Han, J. Hwang, J. Cho and N.-s. Choi, *Journal of Power Sources*, 2017, **357**, 97–106.

[160] N. Schulz, R. Hausbrand, C. Wittich, L. Dimesso and W. Jaegermann, *Journal of The Electrochemical Society*, 2018, **165**, A833–A846.

[161] Q. Li, Y. Wang, X. Wang, X. Sun, J. N. Zhang, X. Yu and H. Li, *ACS Applied Materials and Interfaces*, 2020, **12**, 2319–2326.

[162] D. R. Baer and M. H. Engelhard, *Journal of Electron Spectroscopy and Related Phenomena*, 2010, **178-179**, 415–432.

[163] Q. Jacquet, A. Perez, D. Batuk, G. Van Tendeloo, G. Rousse and J. M. Tarascon, *Chemistry of Materials*, 2017, **29**, 5331–5343.

[164] N. Yabuuchi, M. Nakayama, M. Takeuchi, S. Komaba, Y. Hashimoto, T. Mukai, H. Shiiba, K. Sato, Y. Kobayashi, A. Nakao, M. Yonemura, K. Yamanaka, K. Mitsuhara and T. Ohta, *Nature Communications*, 2016, **7**, 1–10.

[165] M. A. Jones, P. J. Reeves, I. D. Seymour, M. Cliffe, S. E. Dutton and C. P. Grey, *Chemical Communications*, 2019, **55**, 9027–9030.

[166] D. R. Modeshia, R. Walton, M. Mitchel and S. Ashbrook, *Dalton Transactions*, 2010, **39**, 5949–5964.

[167] M. Luo, S. Zheng, J. Wu, K. Zhou, W. Zuo, M. Feng, H. He, R. Liu, J. Zhu, G. Zhao, S. Chen, W. Yang, Z. Peng, Q. Wu and Y. Yang, *Journal of Materials Chemistry A*, 2020, **8**, 5115–5127.

[168] E. McCalla, M. T. Sougrati, G. Rousse, E. J. Berg, A. Abakumov, N. Recham, K. Ramesha, M. Sathiya, R. Dominko, G. Van Tendeloo, P. Novák and J. M. Tarascon, *Journal of the American Chemical Society*, 2015, **137**, 4804–4814.

[169] D. Chen, W. H. Kan and G. Chen, *Advanced Energy Materials*, 2019, **9**, 1901255.

[170] C. Siu, I. D. Seymour, S. Britto, H. Zhang, J. Rana, J. Feng, F. O. Omenya, H. Zhou, N. A. Chernova, G. Zhou, C. P. Grey, L. F. Piper and M. S. Whittingham, *Chemical Communications*, 2018, **54**, 7802–7805.

[171] S. E. Renfrew and B. D. McCloskey, *Journal of the American Chemical Society*, 2017, **139**, 17853–17860.

[172] Y. You, H. Celio, J. Li, A. Dolocan and A. Manthiram, *Angewandte Chemie*, 2018, **57**, 6480–6485.

[173] O. Haik, N. Leifer, Z. Samuk-Fromovich, E. Zinigrad, B. Markovsky, L. Larush, Y. Goffer, G. Goobes and D. Aurbach, *Journal of The Electrochemical Society*, 2010, **157**, A1099–A1107.

[174] J. Sicklinger, M. Metzger, H. Beyer, D. Pritzl and H. A. Gasteiger, *Journal of The Electrochemical Society*, 2019, **166**, A2322–A2335.

[175] M. P. Seah, *Surface and Interface Analysis*, 1980, **2**, 222–239.

[176] I. Takahashi, H. Kiuchi, A. Ohma, T. Fukunaga and E. Matsubara, *Journal of Physical Chemistry C*, 2020, **124**, 9243–9248.

[177] T. Ohashi, K.-i. Okazaki, T. Fukunaga, Z. Ogumi and T. Abe, *ChemElectroChem*, 2020, **7**, 1644–1651.

[178] S. S. Zhang, K. Xu and T. R. Jow, *Electrochemical and Solid-State Letters*, 2002, **5**, 92–94.

[179] D. Aurbach, M. D. Levi, E. Levi, H. Teller, B. Markovsky and G. Salitra, *Journal of The Electrochemical Society*, 1998, **145**, 3024–3034.

[180] M. Gaberscek, J. Moskon, B. Erjavec, R. Dominko and J. Jamnik, *Electrochemical and Solid-State Letters*, 2008, **11**, 170–174.

[181] X. Jiang, B. Wu, X. Yang, K. Xiong, Q. Liu, Y. Zhang, H. Shu, P. Gao, S. Xu and X. Wang, *Electrochimica Acta*, 2019, **325**, 134951.

[182] C. Julien, A. Mauger, K. Zaghib and H. Groult, *Inorganics*, 2014, **2**, 132–154.

[183] S. Tan, Z. Zhang, Y. Li, Y. Li, J. Zheng, Z. Zhou and Y. Yang, *Journal of The Electrochemical Society*, 2013, **160**, A285–A292.

[184] Y.-c. Lu, A. N. Mansour, N. Yabuuchi and Y. Shao-horn, *Chemistry of Materials*, 2009, **21**, 4408–4424.

[185] L. Baggetto, N. J. Dudney and G. M. Veith, *Electrochimica Acta*, 2013, **90**, 135–147.

[186] Z. W. Lebens-Higgins, N. V. Faenza, M. D. Radin, H. Liu, S. Sallis, J. Rana, J. Vinckeviciute, P. J. Reeves, M. J. Zuba, F. Badway, N. Pereira, K. W. Chapman, T. L. Lee, T. Wu, C. P. Grey, B. C. Melot, A. Van Der Ven, G. G. Amatucci, W. Yang and L. F. Piper, *Materials Horizons*, 2019, **6**, 2112–2123.

[187] L. Dahéron, R. Dedryvère, H. Martinez, M. Ménétrier, C. Denage, C. Delmas and D. Gonbeau, *Chemistry of Materials*, 2008, **20**, 583–590.

[188] L. W. Wangoh, Y. Huang, R. L. Jezorek, A. B. Kehoe, G. W. Watson, F. Omenya, N. F. Quackenbush, N. A. Chernova, M. S. Whittingham and L. F. Piper, *ACS Applied Materials and Interfaces*, 2016, **8**, 11532–11538.

[189] Y. Qian, P. Niehoff, M. Börner, M. Grützke, X. Mönnighoff, P. Behrends, S. Nowak, M. Winter and F. M. Schappacher, *Journal of Power Sources*, 2016, **329**, 31–40.

[190] S.-m. Bak, E. Hu, Y. Zhou, X. Yu, S. D. Senanayake, S.-j. Cho, K.-b. Kim, K. Y. Chung, X.-q. Yang and K.-w. Nam, *Applied Materials and Interfaces*, 2014, **6**, 22594–22601.

[191] B. J. Paul, J. Gim, S. Baek, J. Kang, J. Song, S. Kim and J. Kim, *Journal of Nanoscience and Nanotechnology*, 2015, **15**, 6168–6171.

[192] T. Kato, N. Itakura and K. Sugawara, *Journal of Chemical Engineering of Japan*, 2019, **52**, 882–888.

[193] Y. K. Sun, D. H. Kim, C. S. Yoon, S. T. Myung, J. Prakash and K. Amine, *Advanced Functional Materials*, 2010, **20**, 485–491.

[194] A. Banerjee, H. Tang, X. Wang, J. H. Cheng, H. Nguyen, M. Zhang, D. H. Tan, T. A. Wynn, E. A. Wu, J. M. Doux, T. Wu, L. Ma, G. E. Sterbinsky, M. S. D'Souza, S. P. Ong and Y. S. Meng, *ACS Applied Materials and Interfaces*, 2019, **11**, 43138–43145.